

Transversal momentum of the electroweak
gauge boson and forward jets
in high energy factorisation
at the LHC

Dissertation
zur Erlangung des Doktorgrades
des Department Physik
der Universität Hamburg

vorgelegt von

Michal Deák

aus Rimavská Sobota, Slowakei

Hamburg

2009

Gutachter des Dissertation:	Dr. Hannes Jung Prof. Dr. Joachim Bartels
Gutachter der Disputation:	Dr. Hannes Jung Dr. Markus Diehl
Datum der Disputation:	28. 1. 2010
Vorsitzender des Prüfungsausschusses:	Dr. Georg Steinbrueck
Vorsitzender des Promotionsausschusses:	Prof. Dr. Joachim Bartels
Dekan der Fakultät Mathematik, Informatik und Naturwissenschaften:	Prof. Dr. Heinrich Graener

Abstract

Fixed order perturbation theory is not able to describe the transversal momentum spectrum of a electro-weak gauge boson. It is needed to resum whole classes of enhanced logarithmic terms. Depending on the phase space region different classes of logarithmic terms can be important. There are different approaches to sum such logarithmic terms including evolution equations of parton density functions. The evolution equation DGLAP which is valid for integrated parton density functions can be used to effectively produce unintegrated parton density functions using parton shower algorithm, but this approach involves kinematical approximations. With opening of phase space region $\Lambda_{QCD}^2 \ll \mu^2 \ll s$ at the LHC approaches based on the BFKL and the CCFM equations are becoming more relevant. The BFKL and the CCFM equations define genuine unintegrated parton density functions which can be convoluted with matrix elements with off-shell initial state gluons. The off-shell matrix element for $Z/W + Q\bar{Q}$ production was calculated the Monte Carlo CASCADE based on the CCFM evolution equation was used to study the phenomenology of this process concentrated on observables connected with the electro-weak gauge boson for the LHC kinematics. The widening of the peak of the transversal momentum spectrum of the electroweak boson is observed and discussed. The forward jet production using unintegrated parton density functions and off-shell matrix elements at the LHC was studied as a probe for small- x dynamics. Differences in azimuthal decorrelation and harder forward jet transversal momentum spectrum are discussed.

Zusammenfassung

Störungstheorie in bestimmter Ordnung der starken Kopplung ist nicht in der Lage, die Transversaleimpulsverteilung von elektro-schwachen Eichbosonen zu beschreiben. Es ist notwendig, ganze Klassen von führenden logarithmischen Beiträgen aufzusummieren. Abhängig vom Phasenraum koennen verschiedene Klassen von logarithmischen Beiträgen wichtig sein. Es gibt verschiedene Ansätze, diese logarithmischen Beiträge zu summieren, wie z.B. in den Evolutionsgleichungen der Parton Dichte Funktionen. Die Entwicklungsgleichung DGLAP, welche für die integrierte Parton Dichte Funktion gültig ist, kann benutzt werden, um effektiv unintegrierte Parton Dichte Funktionen mit Hilfe des Parton-Shower Algorithmus zu erzeugen, allerdings beinhaltet dieser Ansatz kinematische Approximativen. Mit der Erweiterung der Phasenraums am LHC $\Lambda_{QCD}^2 \ll \mu^2 \ll s$ werden Ansätze basierend auf den BFKL und CCFM Gleichungen zunehmend relevant. Die aus den BFKL und CCFM Gleichungen definieren unintegrierten Parton Dichte Funktionen können mit den Matrixelementen mit "Off-shell" Gluonen verknüpft werden. Die off-shell Matrixelement $Z/W + Q\bar{Q}$ Produktion wurden berechnet und werden nun im Monte-Carlo Cascade auf der Grundlage der CCFM Gleichung benutzt um die Phänomenologie dieses Prozesses bei LHC Kinematik zu studieren. Die Verbreiterung des transversalen Impulsspektrum der elektroschwachen Bosonen wird eingehend diskutiert. Die Forward-Jet-Produktion mit unintegrierten Parton Dichte Funktionen und off-shell Matrixelemente am LHC wurde als Sonde für die Dynamik bei kleinen x . Unterschiede in der azimuthalen Korrelation und dem härteren Transversalimpulsspektrum werden diskutiert.

Contents

1	Introduction	1
2	Overview of QCD at colliders	3
2.1	From e^+e^- to e^-p to pp collider	3
2.1.1	e^+e^- colliders	3
2.1.2	$e^\pm p$ colliders	5
2.1.3	pp colliders	13
3	Evolution equations	15
3.1	The DGLAP evolution equation and its Monte Carlo implementation . . .	15
3.1.1	The implementation of the DGLAP equation for initial state parton shower	19
3.2	k_\perp -factorisation	23
3.2.1	Motivation for use of k_\perp -dependent PDFs	23
3.3	The BFKL evolution equation	25
3.4	The CCFM evolution equation	32
3.4.1	Coherence effect of the QCD radiation	32
3.4.2	Virtual corrections in the CCFM equation.	36
3.5	uPDF evolution equations summary	37
4	Monte Carlo generators PYTHIA, HERWIG and CASCADE	38
4.1	PYTHIA	38
4.2	CASCADE	39
4.3	HERWIG and HERWIG++	40
5	The transverse momentum of the Z-boson	42
5.1	Analytical approaches	42
5.2	Semi-analytical approaches	44
6	Drell-Yan production in heavy quark-antiquark annihilation	47
6.1	Z and W production associated with heavy quark-antiquark pair in k_\perp -factorisation.	48
6.1.1	Discussion of the kinematics	50
6.1.2	Discussion of the gauge invariance	51

6.1.3	Discussion of some aspects of the results	54
6.2	Z and W production associated with heavy quark-antiquark pair in HERWIG++	57
6.2.1	Introduction	57
6.2.2	Transverse momentum of b-quark jets in Fortran HERWIG and in HERWIG++	59
6.2.3	Initial state splitting functions in quasi-collinear limit	59
6.2.4	Evolution of massive b-quarks in HERWIG++	61
7	Forward jets at the LHC in high energy factorisation	65
7.1	Forward jets in asymmetric kinematical situation	66
7.2	Kinematics and dynamics	67
7.2.1	Calculation of matrix element	68
7.3	Implementation into Monte Carlo program	70
7.4	Results	70
7.4.1	Transversal momentum and energy flows in forward rapidity region	71
8	Summary and Conclusions	75
9	Appendix	0
A	Discussion of the method of orthogonal amplitudes	1
B	Z and W^\pm production associated with quark-antiquark pair in k_T -factorization at the LHC	1
B.1	Introduction	4
B.2	Kinematics of Z/W production and calculation of the hard matrix element	5
B.3	Numerical studies	12
B.4	Summary and Conclusions	25
C	Forward Jet Production at the Large Hadron Collider	1
C.1	Introduction	4
C.2	High-energy factorized cross subsections	5
C.3	Matrix elements for fully exclusive events	7
C.4	Numerical results	8
C.5	Conclusions	10

List of Figures

2.1.1 Processes contributing to $e^+e^- \rightarrow X$, a) annihilation, b) photon exchange.	4
2.1.2 Higher order QCD corrections to total e^+e^- cross section. Left diagram contributes also to 3-jet cross section.	4
2.1.3 Quark production threshold effects in e^+e^- scattering [1].	6
2.1.4 Notation used in text for the ep scattering process.	7
2.1.5 Diagram of photon scattering on one of the partons.	10
2.1.6 The Bjorken scaling observed for values of $x \sim 0.2$ [2].	11
2.1.7 Diagrams which cause violation of Bjorken scaling.	12
2.1.8 Diagrammatic representation of the formula (2.1.28).	13
2.1.9 Schematic diagram of hadron-hadron scattering. In X_1 and X_2 are included remnants of protons and produced soft particles.	14
3.1.1 On the momenta variables of splitting.	18
3.1.2 Schematic picture of the DGLAP equation.	19
3.1.3 Schematic picture describing the modified splitting function.	20
3.3.1 Multi-regge kinematics.	25
3.3.2 Leading contribution to process $qq \rightarrow qq$	26
3.3.3 Next to leading contribution to process $qq \rightarrow qq$	26
3.3.4 Emergence of Lipatov effective vertex.	27
3.3.5 A gluon emission ladder with virtual corrections.	28
3.3.6 BFKL equation for $q^2 = 0$ momentum exchange.	29
3.4.1 Soft gluon emission for $\theta > \theta'$	32
3.4.2 On derivation of the formula (3.4.18).	35
4.1.1 Schematic picture of MPI with two hard scattering subprocesses.	38
6.1.1 Diagrams for W and Z production.	49
6.1.2 Diagrams for W and Z production.	49
6.1.3 Probability distribution of x_g in $Z/W + Q\bar{Q}$ in Monte Carlo generator CASCADE.	50
6.1.4 Probability distribution of \mathbf{k}_g in $Z/W + Q\bar{Q}$ in Monte Carlo generator CASCADE.	51
6.1.5 Replacing protons by quarks.	53

6.1.6	Transverse momentum distributions of the produced Z gauge bosons. Calculation with massive b -quarks. Both calculations are in LO of perturbation series.	55
6.1.7	Comparison of cross sections differential in transverse momentum of the produced Z gauge boson. Calculation with massless b -quarks. The applied cuts are described in the text.	56
6.1.8	Comparison of cross sections differential in transverse momentum of the produced Z gauge boson (linear scale). Calculation with massless b -quarks. The applied cuts are described in the text.	56
6.2.1	Rapidity-transversal momentum correlation plot.	60
6.2.2	Schematic diagram of the calculation of the splitting function.	60
6.2.3	Schematic diagram of $b\bar{b}$ annihilation into Z boson with \bar{b} originating from $g \rightarrow b\bar{b}$ splitting.	62
6.2.4	Transversal momentum spectrum of the Z boson for different evolution scales.	62
6.2.5	Transversal momentum spectrum of the b/\bar{b} quark for different evolution scales.	63
6.2.6	Invariant mass of the $b\bar{b}$ pair from HERWIG++ and MCFM	64
7.2.1	Set of diagrams of $qg^* \rightarrow qg$ with initial state gluon off-shell and initial state quark on-shell.	69
7.4.1	Transversal momentum of jets in for pseudo-rapidity of jets $3 < \eta_j < 5$	72
7.4.2	Multiplicity of jets in a single event for pseudo-rapidity of jets $3 < \eta_j < 5$	73
7.4.3	Azimuthal correlation of jets in for pseudo-rapidity of the forward jet $3 < \eta_j < 5$	73
7.4.4	Average azimuthal correlation as a function of the rapidity distance of the jet pair.	74
B.1	Labeling and flow of momenta of the process $pp \rightarrow q(W/Z)\bar{q}X$	6
B.2	Full set of diagrams contributing to W/Z production via off-shell gluon-gluon fusion.	8
B.3	Diagrams contributing to the Lipatov vertex.	8
B.4	Transverse momentum distributions of the produced Z gauge bosons. Calculation with massive b -quarks. Both calculations are in LO of perturbation series.	14
B.5	Rapidity distribution of the produced Z gauge bosons. Calculation with massive b -quarks. Both calculations are in LO of perturbation series.	14
B.6	Distributions of the rapidity distance between quark and antiquark. Calculation with massive b -quarks. Both calculations are in LO of perturbation series.	15
B.7	Distributions of the rapidity distance between quark and antiquark. Calculation with massive b -quarks. A cut on $p_{Z\perp} > 50$ GeV has been applied.	16

B.8	Distributions of the distance in azimuthal angle of Z and highest p_{\perp} quark or antiquark. Calculation with massive b -quarks. Both calculations are in LO of perturbation series.	16
B.9	Comparison of cross sections differential in transverse momentum of the produced Z gauge boson. Calculation with massless b -quarks. The applied cuts are described in the text.	18
B.10	Comparison of cross sections differential in transverse momentum of the produced Z gauge boson (linear scale). Calculation with massless b -quarks. The applied cuts are described in the text.	18
B.11	Comparison of cross sections differential in rapidity of the produced Z gauge boson (logarithmic scale). Calculation with massless b -quarks. The applied cuts are described in the text.	19
B.12	Comparison of cross sections differential in the p_{\perp} of the system $Zb\bar{b}$. Calculation with massless b -quarks. The applied cuts are described in the text.	20
B.13	Comparison of cross sections differential in distance in azimuthal angle of Z and higher p_{\perp} b/\bar{b} . Calculation with massless b -quarks. The applied cuts are described in the text.	21
B.14	Comparison of cross sections differential in distance in azimuthal angle of Z and higher p_{\perp} b/\bar{b} . Calculation with massless b -quarks. An additional cut on $p_{Z\perp} > 50$ GeV has been applied.	21
B.15	Transverse momentum distributions of produced Z gauge boson calculated in CASCADE using massive quarks. Cases with different uPDFs compared.	23
B.16	Comparison of cross sections differential in distance in azimuthal angle of Z and higher p_{\perp} b/\bar{b} , using massive quarks. Cases with different uPDFs compared.	23
B.17	Transverse momentum distributions of produced Z gauge boson calculated in CASCADE using massive quarks. Cases with different renormalization scales μ_R compared.	24
B.18	Transverse momentum distributions of produced Z gauge boson calculated in CASCADE using massive quarks. Cases with different renormalization scales μ_R compared.	24
C.1	Jet production in the forward rapidity region in hadron-hadron collisions.	4
C.2	(Left) High- p_T events in the forward and central detectors; (right) azimuthal plane segmentation.	5
C.3	(a) Factorized structure of the cross subsection; (b) a graph contributing to the qg channel matrix element.	6
C.4	The k_T/Q_T dependence of the factorizing qg hard cross subsection at high energy: (left) C_F^2 term; (right) $C_F C_A$ term ($\xi_1 \xi_2 S/Q_T^2 = 10^2$, $\alpha_s = 0.2$).	9
C.5	The energy dependence of the qg hard cross subsection ($k_T/Q_T = 1$).	10
C.6	The k_T/Q_T dependence of the factorizing gg matrix elements: (a) $gg \rightarrow gg$; (b) $gg \rightarrow q\bar{q}$ C_F term; (c) $gg \rightarrow q\bar{q}$ C_A term ($\xi_1 \xi_2 S/Q_T^2 = 10^2$, $\alpha_s = 0.2$).	11

List of Tables

B.1	Total cross sections for different final states, calculated in k_T -factorization using CASCADE.	15
B.2	Total cross sections of the process $pp \rightarrow Zb\bar{b} + X$ for different sets of unintegrated parton distribution functions.	22
B.3	Total cross sections for different renormalization scale μ	22

Chapter 1

Introduction

The large progress made in experimental and theoretical physics in the first half of the 20th century for which grounds were based already in the end of the 19th century by the discovery of the electron by Joseph Thomson in 1897, continuing with the discovery of the proton by Ernest Rutherford by his famous experiment in 1919, the discovery of the Schrödinger equation by Erwin Schrödinger in 1926 and the Heisenberg relations in 1925 by Werner Heisenberg, the discovery of the Dirac equation in 1928 by Paul Dirac, opened way to formulation of the quantum field theory and to perturbative approach in a diagrammatic form used today.

Quantum field theory was with huge success applied to electromagnetic phenomena. Indeed the most precise agreement of a theory prediction and experiment is the anomalous magnetic moment of the electron minus 2 agreeing on 8 digits is a unprecedented success of the quantum electro-dynamics (QED). QED being a abelian gauge theory with gauge group $U(1)$ is the simplest discovered quantum field theory realised in the nature.

An important step in our understanding of particle physics was the discovery that the proper field theory describing so called strong interactions is a non-abelian gauge theory with gauge group $SU(3)$. Quantum chromo-dynamics (QCD) together with experimental discoveries of quarks explained all the features of particle mass spectra observed and still successfully predicts and explains experimental particle data. Understanding of the nature of strong interaction was a big step in understanding the structure and origin of all the particles which build most of the visible matter in the Universe – hadrons.

Another force which had to be explained was a force causing the particles as leptons decay on much larger time scales as hadrons. The force was named weak force and it was found by Sheldon Glashow, Abdus Salam and Steven Weinberg that the correct quantum field theory describing it is $SU(2)$ gauge theory. Part of the discovery was a finding that the electromagnetic and the weak interaction can be unified under one quantum field theory. All the interactions mentioned can be included into one quantum field theory called the Standard Model of particle physics (shortly called the Standard Model or the SM) with gauge theory with $SU(3) \times SU(2) \times U(1)$ symmetry.

One of the still remaining problems of the SM is the question of mass and fermion families. The SM as a theory would work without having the masses of particles included,

but experimental evidence shows that even elementary particles without known internal structure have finite masses. The simplest and quite natural way how to include masses of particles is to spontaneously break the $SU(2) \times U(1)$ symmetry by a scalar field with a negative vacuum expectation value. The breaking results into emergence of Goldstone bosons of which all except one disappear. The remaining scalar field is called the Higgs field and through interactions with weak interaction bosons, leptons and quarks creates mass terms for these particles.

The interaction we did not mention and which plays a significant role for the existence of the Universe, but is by present knowledge negligible for the internal structure of matter is the gravitational force. All the known forces except of gravitational force are studied by particle physics. Since the strong interaction and weak interaction manifest themselves in collisions of particles at high energies it is the high energy particle physics which can study detailed properties of the matter in the Universe and gives answers to questions related to the origin of the world around us.

In the next chapter, 2, an overview of QCD physics on particle colliders will be done. Then in the chapter 3 evolution equations of parton density functions, their implementation in Monte Carlo programs and k_{\perp} -factorisation will be introduced. An overview on resummation methods for electro-weak gauge boson is done in 5. The chapters 6 and 7 together with Appendix 9 part B and C represent my work during my PhD. studies. In the chapter 6 the calculation of $Z/W/\gamma + Q\bar{Q} + X$ in proton-proton collisions is discussed. This chapter is an extension of 9 part B where a more detailed phenomenological study was done. In the chapter 7 the calculation of a forward jet production in high energy factorisation is discussed and some phenomenological results are presented. The part C of Appendix 9 discusses the method of orthogonal amplitudes used for calculation of the matrix element $g^* + g^* \rightarrow Z/W/\gamma + Q\bar{Q}$. The thesis is concluded and summarised in the chapter 8.

Chapter 2

Overview of QCD at colliders

In high energy experiments two different kinds of interactions, electroweak and strong, play a significant role. In this chapter we will go through different particle collider types and will discuss the significance of particular interaction types. We will exclude a discussion of physics beyond the SM since the topic is too wide and not relevant for our discussions.

2.1 From e^+e^- to e^-p to pp collider

2.1.1 e^+e^- colliders

The simplest type of a particle collider is a collider which collides electrons and positrons. The reason is that electrons and positrons are to our present knowledge elementary particles without internal structure. In a case when the colliding electron and positron annihilate into a gauge boson the collision process can be therefore treated completely perturbatively at high energies, figure 2.1.1 a). Another type of interaction of an electron and a positron can involve the exchange of almost real photons which can contribute with a non-perturbative component, figure 2.1.1 b). Initial state radiation in the process $e^+e^- \rightarrow X$ can be described in leading order (LO) and next to leading order (NLO) purely by electroweak interactions, QCD plays a significant role for corrections of the final state.

The cross section for the e^+e^- annihilation in LO can be written with the hard process matrix element $\mathcal{M}_{e^+e^- \rightarrow \gamma^*/Z \rightarrow X}$ in simple form

$$\sigma_{e^+e^-} = \int_{\Omega_f} \frac{1}{2s} |\mathcal{M}_{e^+e^- \rightarrow \gamma^*/Z \rightarrow X}|^2 d\Omega_f \quad (2.1.1)$$

or rewritten as a cross section differential in the mass of the s -channel virtual electroweak gauge boson

$$\frac{d\sigma_{e^+e^-}}{dM_Z^2} = \int_{\Omega_f} \frac{1}{2s} |\mathcal{M}_{e^+e^- \rightarrow \gamma^*/Z \rightarrow X}|^2 \delta(s - M_Z^2) d\Omega_f, \quad (2.1.2)$$

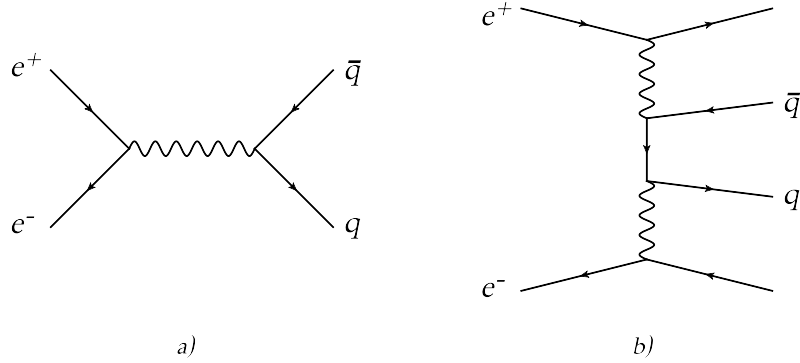


Figure 2.1.1: Processes contributing to $e^+e^- \rightarrow X$, a) annihilation, b) photon exchange.

where Ω_f is the final state particle phase space and s is the e^+e^- collision energy squared. The factor $1/(2s)$ is the flux factor for the e^+e^- collision in the case when the electron and positron collide head-on. The more general formula for the flux factor reads [1]

$$\frac{1}{2E_{e^+}2E_{e^-}|v_{e^+} - v_{e^-}|}, \quad (2.1.3)$$

where E_{e^+} and E_{e^-} are the energies and v_{e^+} and v_{e^-} are velocities of the electron and positron respectively.

Everything described up to now in this subsection can be calculated entirely in framework of QED. QCD becomes important, when the higher order corrections to the total cross section of e^+e^- scattering are calculated, or when n -jet with $n > 2$ observables are calculated. Typical higher order diagrams are in the figure 2.1.2. There are also electroweak corrections which are however important only at higher the next to leading order, because the electroweak coupling constant is approximately 10 times smaller the α_S . Since $\alpha \sim 0.01$ and $\alpha_S \sim 0.1$, the LO - the tree level order cross section is proportional to α^2 , the next to NLO contributions are proportional to $\alpha^2\alpha_S$ and next to NLO corrections are proportional to $\alpha^2\alpha_S^2$ and to $\alpha^3\alpha_S$.

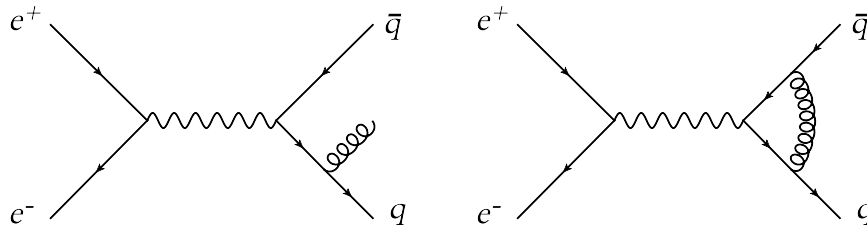


Figure 2.1.2: Higher order QCD corrections to total e^+e^- cross section. Left diagram contributes also to 3-jet cross section.

QCD corrections have been calculated to high orders in fixed order perturbation theory approach, but also certain classes of logarithmic terms to all orders have been summed,

summarised in [3]. By looking at diagrams in 2.1.2 we can see that in leading and next to leading order of the perturbation theory the QCD corrections factorise from the $e^+\gamma^*e^-$ vertex. One can consider two processes: annihilation of e^+e^- pair into an off-shell photon and off-shell photon decay into QCD particles.

What is important from the point of view of QCD is that in the e^+e^- scattering cross section data, with increasing centre of mass energy \sqrt{s} of the collision, a step structure in the cross section was observed. The steps can be associated with mass thresholds for quark-antiquark production. One can see these threshold effects in plots of ratio $R = (\sigma_{e^+e^- \rightarrow \text{hadrons}}/\sigma_{e^+e^- \rightarrow \mu^+\mu^-})$, figure 2.1.3. The cross section corresponded to the one predicted by QED, but was roughly bigger by a factor of 3. The factor 3 was identified as the contribution of all 3 colours of the quarks. Each step in the in R as a function of \sqrt{s} corresponds to increase by a contribution from a production channel of a new quark species.

Electron-positron colliders represent a very clean environment to study perturbative QCD since it contributes at LO and NLO only in the final state and the non-perturbative component can be reduced to hadronisation of final state partons. Examples of e^+e^- colliders are SLC at SLAC in California (USA), LEP at CERN, PETRA at DESY in Hamburg, Germany.

2.1.2 $e^\pm p$ colliders

The situation at a collider which collides electrons and protons is more complicated. The proton is a hadron composed of quarks and gluons which are confined inside of it by the strong force. The proton will be always a source of a non-perturbative component because perturbative techniques cannot be applied to its structure, because the typical scale at which are the gluon and quark field interacting in proton is below its mass $m_p \sim 1 \text{ GeV}$. The coupling constant $\alpha_S(\mu)$ is not a reliable expansion parameter for $\mu < 1 \text{ GeV}$.

Let us consider now electron-proton scattering via a photon exchange as depicted in figure 2.1.4. We will first discuss the kinematics of this process. The momenta of the scattered electron before and after interaction can be, in a frame in which the initial state electron moves along the z -axis, written in this form

$$\begin{aligned} k &= (E, E, 0, 0), \\ k' &= (E', E' \cos \theta, E' \sin \theta, 0) \end{aligned} \tag{2.1.4}$$

where E and E' are the energy of the scattered electron before and after the collision respectively. The angle θ is the angle between the momentum of the electron after the scattering and the z -axis (the direction of the incoming electron). In figure 2.1.4 $q = k - k'$ is the 4-momentum of the off-shell photon with off-shellness $q^2 < 0$. The virtuality of the photon can be used as a hard scale and it is therefore useful to define quantity

$$Q^2 = -q^2 = -(k - k')^2 = 2k.k' = 2EE'(1 - \cos \theta) \tag{2.1.5}$$

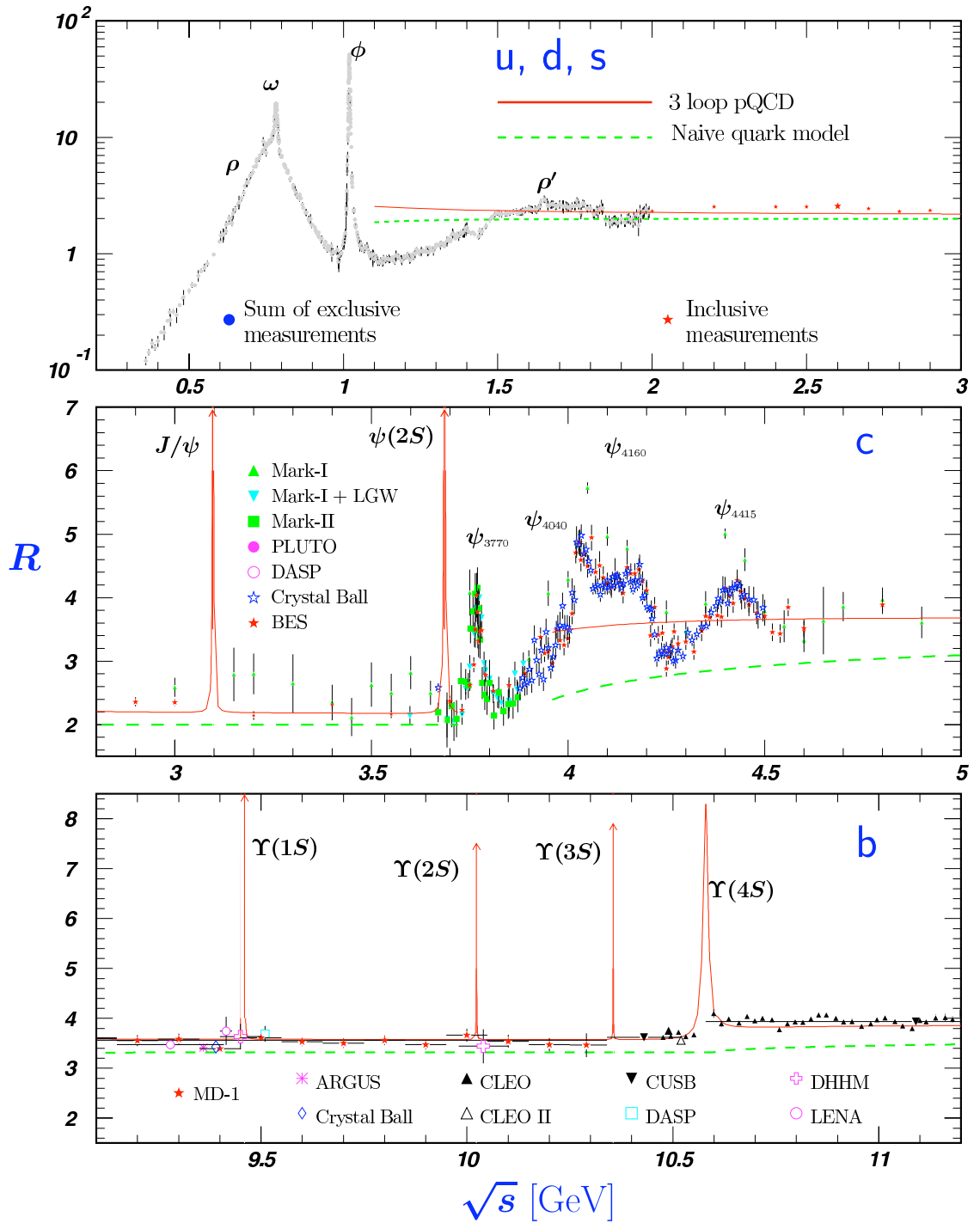


Figure 2.1.3: Quark production threshold effects in e^+e^- scattering [1].

For convenience one defines variables

$$\begin{aligned} s &= W^2 = (p + k)^2 = 2p \cdot k, \\ x &= \frac{Q^2}{2M\nu} = \frac{Q^2}{2M(E - E')}, \\ y &= \frac{p \cdot q}{p \cdot k} = \frac{E - E'}{E}. \end{aligned} \quad (2.1.6)$$

In a scattering of two particles are exactly 2 kinematical variables free and all other variables can be calculated from them. The usual choice is Q^2 and x , but also combinations E' and θ , Q^2 and ν and x and y are used. The variable y is called inelasticity because in the laboratory frame it corresponds to the relative energy of the electron transmitted into proton. The variable $s = W^2$ describes the invariant energy of the electron-proton collision.

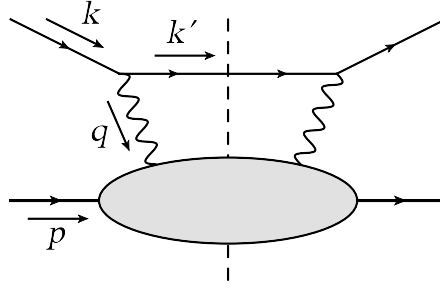


Figure 2.1.4: Notation used in text for the ep scattering process.

The cross section for this process can be written in a factorised form and can be considered as a off-mass shell photon-proton scattering times a factor describing the photon emission from electron times a photon flux factor. To write an expression for the cross section of photon-proton scattering we will consider coupling of a photon to a proton flux by

$$J_p^\mu(\xi) A_\mu(\xi) \quad (2.1.7)$$

where $J_p^\mu(\xi)$ is the proton flux and $A_\mu(\xi)$ the photon flux in the 4-point ξ .

Taking advantage from this structure we can now write the current matrix element of the transition of the proton state P with momentum p into a state X with momentum p_X

$$\langle X(p_X) | J_p^\mu(\xi) | P(p) \rangle = \langle X(p_X) | J_p^\mu(0) | P(p) \rangle e^{-i(p-p_X) \cdot \xi} \quad (2.1.8)$$

The hadron tensor which carries the information about the cross section from the hadron side can be written using (2.1.8)

$$\begin{aligned} W^{\mu\nu} &= \frac{1}{2} \sum_{pol.} \sum_{X, p_X} \langle P(p) | J_p^\mu(0) | X(p_X) \rangle \langle X(p_X) | J_p^\nu(0) | P(p) \rangle (2\pi)^3 \\ &\quad \times \delta^{(4)}(p_X - p - q), \end{aligned} \quad (2.1.9)$$

By applying the factor $1/2$ and summing over polarisations we average over the proton polarisation states. We consider a massive proton with mass M .

Using an identity for the delta function we can rewrite (2.1.9) into

$$W^{\mu\nu} = \frac{1}{2} \sum_{pol.} \sum_{X, p_X} \int \frac{d^4\zeta}{(2\pi)^4} \langle P(p) | J_p^\mu(0) | X(p_X) \rangle \langle X(p_X) | J_p^\nu(0) | P(p) \rangle (2\pi)^3 \times e^{-i(p_X-p)\cdot\zeta} e^{iq\cdot\zeta} \quad (2.1.10)$$

We can then rewrite last equation using the identity in (2.1.8) to

$$W^{\mu\nu} = \frac{1}{2} \sum_{pol.} \sum_{X, p_X} \int \frac{d^4\zeta}{(2\pi)^4} \langle P(p) | J_p^\mu(\zeta) | X(p_X) \rangle \langle X(p_X) | J_p^\nu(0) | P(p) \rangle (2\pi)^3 e^{iq\cdot\zeta} \quad (2.1.11)$$

We can now use the completeness relation

$$\sum_{X, p_X} |X(p_X)\rangle \langle X(p_X)| = 1 \quad (2.1.12)$$

which simplifies (2.1.11) to

$$W^{\mu\nu} = \frac{1}{2} \sum_{pol.} \int \frac{d^4\zeta}{(2\pi)^4} \langle P(p) | J_p^\mu(\zeta) J_p^\nu(0) | P(p) \rangle (2\pi)^3 e^{iq\cdot\zeta}. \quad (2.1.13)$$

We can write the most general expression for a tensor depending on 4-momenta p and q because the right-hand side of (2.1.13) depends only on these momenta. The most general tensor can be written has this form [4]

$$W^{\mu\nu} = -W_1 g^{\mu\nu} + W_2 \frac{p^\mu p^\nu}{M^2} + W_3 \epsilon^{\mu\nu\kappa\lambda} \frac{p^\kappa q^\lambda}{M^2} + W_4 \frac{q^\mu q^\nu}{M^2} + W_5 \frac{p^\mu q^\nu + p^\nu q^\mu}{M^2} \quad (2.1.14)$$

Scalar functions W_1 , W_2 , W_3 , W_4 and W_5 depend only on Lorentz invariants $p\cdot q$ and q^2 . The factor $1/M^2$ is used to keep all the W -functions of the same dimension.

The equation (2.1.14) does include terms with the Levi-Civita tensor $\epsilon^{\alpha\beta\gamma\delta}$, but because the whole process of photon-proton scattering conserves parity and terms proportional to Levi-Civita tensor would violate parity. The function $W_3 = 0$. If we would on the other hand consider also W and Z boson exchange the function $W_3 \neq 0$, because of parity violation in such processes.

The current $J_p^\mu(x)$ is being conserved which results into an identity for the tensor $W^{\mu\nu}$

$$q^\mu W^{\mu\nu} = 0 \quad (2.1.15)$$

which can be used to derive relations between functions W_1 , W_2 , W_4 and W_5 and to reduce the number of independent functions describing $W^{\mu\nu}$. The relations one obtains are

$$\begin{aligned} W_5 &= -\frac{p\cdot q}{q^2} W_2, \\ W_4 &= -\frac{p\cdot q}{q^2} W_5 + \frac{M^2}{q^2} W_1. \end{aligned} \quad (2.1.16)$$

The structure of $W^{\mu\nu}$ reduces to

$$W^{\mu\nu} = W_1 \left(-g^{\mu\nu} + \frac{q^\mu q^\nu}{q^2} \right) + W_2 \frac{1}{M^2} \left(p^\mu - \frac{p \cdot q}{q^2} q^\mu \right) \left(p^\nu - \frac{p \cdot q}{q^2} q^\nu \right) \quad (2.1.17)$$

The cross section can be written as a contraction of the lepton tensor and hadron tensor in this way

$$\frac{d\sigma_{ep \rightarrow X}}{d\Omega dE'} = \frac{\alpha^2}{Q^4} \frac{E'}{E} L^{\mu\nu} W_{\mu\nu}, \quad (2.1.18)$$

The tensor $L^{\mu\nu}$ also satisfies the condition $q^\mu L^{\mu\nu} = 0$ and that is why in (2.1.17) we do not have to consider terms proportional to q^μ and q^ν . The application of this leaves us with an expression for the relevant part of $W^{\mu\nu}$

$$W^{\mu\nu} = -W_1 g^{\mu\nu} + \frac{1}{M^2} W_2 p^\mu p^\nu. \quad (2.1.19)$$

What remains is to calculate the $L^{\mu\nu}$, which is:

$$L^{\mu\nu} = \frac{1}{2} \sum_{\lambda\lambda'} \bar{u}_{\lambda'}(k') \gamma^\mu u_\lambda(k) \bar{u}_\lambda(k) \gamma^\nu u_{\lambda'}(k') = 2(k'^\mu k^\nu + k'^\nu k^\mu - k \cdot k' g^{\mu\nu}) \quad (2.1.20)$$

The right-hand side of the equation (2.1.18) then gives

$$\frac{d\sigma_{ep \rightarrow X}}{d\Omega dE'} = \frac{\alpha^2}{4E^2 \sin^4 \frac{\theta}{2}} \left(2W_1 \sin^2 \frac{\theta}{2} + W_2 \cos^2 \frac{\theta}{2} \right). \quad (2.1.21)$$

It is convenient to define functions

$$\begin{aligned} F_1 &= MW_1, \\ F_2 &= \nu W_2. \end{aligned} \quad (2.1.22)$$

It is possible to fit the functions F_1 and F_2 by comparing the data with the formula for the cross section. For this it is enough to measure the energy and the angle θ of the scattered electron. After obtaining the functions F_1 and F_2 from experiment in 1960's at SLAC linear accelerator it came out that functions F_1 and F_2 are not functions of 2 variables θ and E' , but only one of them. This behaviour is called *Bjorken scaling*, figure 2.1.6. The solution to this mysterious behaviour came from Richard Feynman who suggested existence of almost free constituents of the proton. How the existence of free proton constituents can explain the Bjorken scaling we should first compare the expressions for the cross section of deep inelastic electron-proton scattering with cross section of elastic scattering of electron and point-like proton. The cross section for the latter one reads

$$\frac{d\sigma_{ep \rightarrow ep}}{d\Omega dE'} = \frac{\alpha^2}{4E^2 \sin^4 \frac{\theta}{2}} \left(\frac{Q^2}{2M^2} \sin^2 \frac{\theta}{2} + \cos^2 \frac{\theta}{2} \right) \delta \left(\nu - \frac{Q^2}{2M} \right). \quad (2.1.23)$$

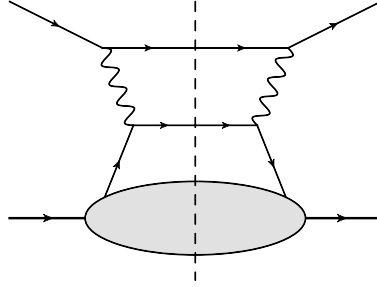


Figure 2.1.5: Diagram of photon scattering on one of the partons.

One can find the functions W_1^{point} and W_2^{point} , by comparing the equations (2.1.21) and (2.1.23). The resulting functions are

$$2W_1^{point} = \frac{Q^2}{2M^2} \delta\left(\nu - \frac{Q^2}{2M}\right), W_2^{point} = \delta\left(\nu - \frac{Q^2}{2M}\right). \quad (2.1.24)$$

The model based on the assumption of free proton constituents is called *parton model* and the constituents of proton are called *partons*. The model works in the infinite proton momentum frame. Each of the partons belong to some parton species i and can carry a momentum fraction $0 < \kappa < 1$ of the proton momentum. When a photon interacts with the proton it hits one of the partons. The probability for a parton of species i carrying a proton momentum fraction κ to be struck by the photon is $f_i(\kappa)$ - *parton density*. The functions $f_i(\kappa)$ satisfy normalisation condition

$$\sum_i \int_0^1 d\kappa \kappa f_i(\kappa) = 1. \quad (2.1.25)$$

Partons were later identified as quarks and gluons of QCD. Assuming the knowledge of functions $f_i(\kappa)$, the parton model gives us a possibility to calculate the functions W_1 and W_2 . We will calculate W_2 by convoluting the expression for W_2^{point} with the sum of parton densities weighted by charges of the partons squared

$$\begin{aligned} F_2(x) = \nu W_2(x) &= \sum_i \int_0^1 d\kappa e_i^2 f_i(\kappa) \delta\left(\nu - \frac{Q^2}{2M\kappa}\right) \nu \\ &= \sum_i \int_0^1 d\kappa e_i^2 f_i(\kappa) \delta\left(1 - \frac{Q^2}{2M\kappa\nu}\right) = \sum_i \int_0^1 d\kappa e_i^2 f_i(\kappa) \delta\left(1 - \frac{x}{\kappa}\right) \\ &= \sum_i \int_0^1 d\kappa e_i^2 f_i(\kappa) \frac{\kappa^2}{x} \delta(\kappa - x) = \sum_i e_i^2 x f_i(x). \end{aligned} \quad (2.1.26)$$

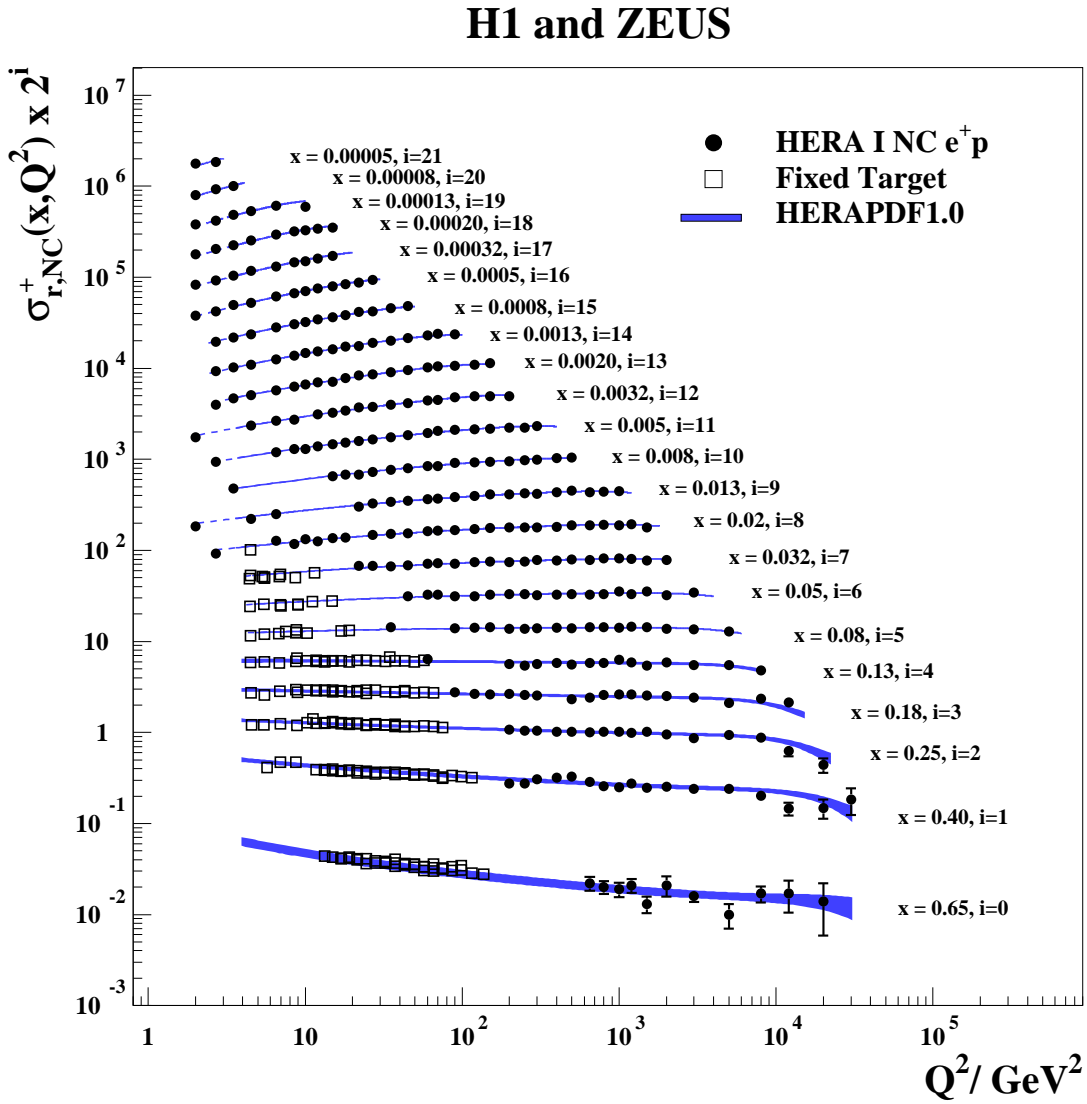


Figure 2.1.6: The Bjorken scaling observed for values of $x \sim 0.2$ [2].

By doing the same exercise we would obtain expression $F_1(x) = MW_1(x) = \frac{1}{2} \sum_i e_i^2 f_i(x)$.

We see that

$$F_2(x) = 2xF_1(x), \quad (2.1.27)$$

which is called Callan-Gross relation and has a specific form because of the spin $\frac{1}{2}$ of the partons. If partons would have spin different than $\frac{1}{2}$ the equation (2.1.27) would have a different form. The Callan-Gross relation is valid for a certain kinematic range of experimental data.

To the end of this chapter we have to comment on Bjorken scaling. Bjorken scaling is not exact and is violated for small- x and also for $x > 0.3$ (figure 2.1.6) so the functions $F_1(x)$ and $F_2(x)$ will be also functions of Q^2 : $F_1(x, Q^2)$, $F_2(x, Q^2)$. This behaviour was experimentally discovered at EMC at CERN, SLC at SLAC and at TeVatron and was also found in HERA data at DESY. From the theoretical point of view the violation of the Bjorken scaling is caused by higher order QCD corrections to the photon-parton/quark scattering in figure 2.1.7.

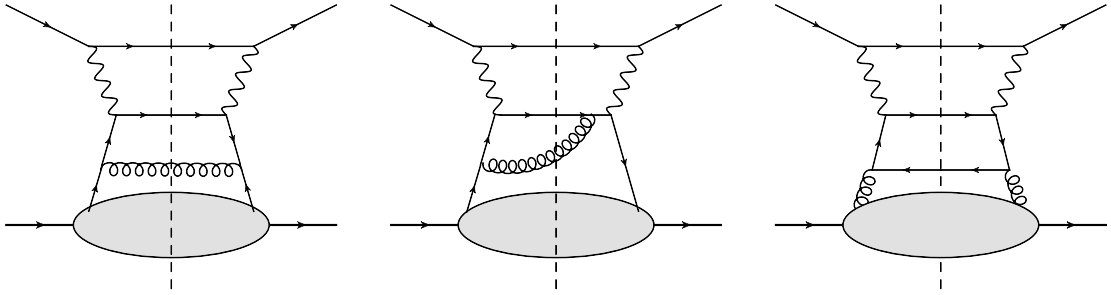


Figure 2.1.7: Diagrams which cause violation of Bjorken scaling.

The final result of this chapter is that the cross section for a process $\gamma^*p \rightarrow O_H + X$, O_H being a final state of a hard subprocess $\gamma^*i \rightarrow O_H$ and i being a parton species, can be written as convolution of the cross section for the subprocess $\gamma^*p \rightarrow O_H$ and a PDF (figure 2.1.8)

$$d\sigma_{\gamma^*p \rightarrow X+O_H} = \sum_i \int_0^1 d\xi d\hat{\sigma}_{i\gamma^* \rightarrow O_H}(\xi, Q^2) f_i(\xi, Q^2), \quad (2.1.28)$$

where the sum runs through all possible parton species. The cross section for $ep \rightarrow O_H + X$ can be expressed using (2.1.28)

$$d\sigma_{ep \rightarrow X+O_H} = \frac{\alpha}{2\pi Q^2} \frac{1 + (1-y)^2}{y} d\sigma_{\gamma^*p \rightarrow X+O_H}. \quad (2.1.29)$$

We did not comment on the Q^2 - the scale dependence of the PDFs. We will discuss it in the section 3.1.

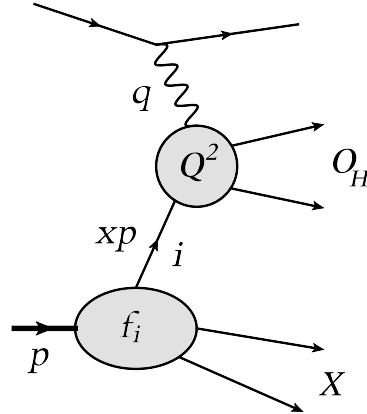


Figure 2.1.8: Diagrammatic representation of the formula (2.1.28).

2.1.3 pp colliders

The last type of a collider which will be presented here is the $p/\bar{p}p$ or hadron collider. In hadron colliders both colliding particles introduce a non-perturbative factor. To be able at all to use perturbation theory for such scattering process one needs to ensure the presence of a hard scale. A way how to do it is to require a hard jet or any hard subprocess to happen during the hadron-hadron collision. One can then push the concept from the section 2.1.2 further and calculate the cross section of the process $p/\bar{p} + p \rightarrow X + O_H$, where O_H is set of particles originating from the hard subprocess, by assuming a collision of any combination of two partons, one originating from one of the protons and other from the other one, which can result in the final state $X + O_H$. The formula for the differential cross section then will be

$$d\sigma_{pp \rightarrow X + O_H} = \sum_{i,j} \int_0^1 dx_1 \int_0^1 dx_2 d\hat{\sigma}_{ij \rightarrow O_H}(x_1, x_2, \mu^2) f_i(x_1, \mu^2) f_j(x_2, \mu^2). \quad (2.1.30)$$

where $d\hat{\sigma}_{ij \rightarrow O_H}(x_1, x_2, \mu^2)$ is the partonic cross section which describes the production of O_H in the collision of partons i and j . Partons i and j carry momentum fractions of their mother protons x_1 and x_2 respectively. The summation over i and j goes through all combinations for which the production of $X + O_H$ is possible. The partonic cross section can be differential in some of the kinematic variables of O_H in such a way that the presence of the hard scale μ^2 is ensured. For example if $O_H = \{Z\}$ then we can integrate over all the phase space of the gauge boson Z , because its mass m_Z ensures presence of a hard scale $\mu^2 = m_Z^2$.

From the experimental point of view hadron colliders present a very complicated setup to study the hard subprocess. Experimentalists have to deal with the fact that the collision of the partons in the hard subprocess does not happen in the center of mass frame. In fact in each hadron-hadron collision is the center of mass frame of the colliding partons different.

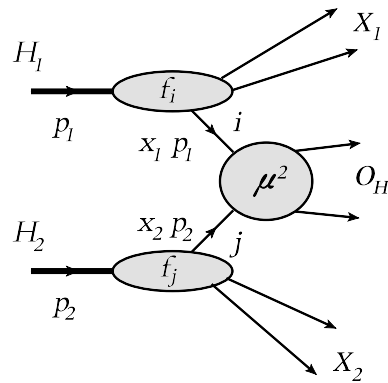


Figure 2.1.9: Schematic diagram of hadron-hadron scattering. In X_1 and X_2 are included remnants of protons and produced soft particles.

It is therefore very important to measure the parton density functions at electron-proton colliders, where the situation is much simpler. The advantage of hadron-hadron colliders is much higher luminosity and less energy losses through synchrotron radiation which allows for higher beam energies. The fact that the partonic collision energy is different in every collision can be viewed as an advantage for discovery searches because a large energy range is probed. One has more trouble with all what one can "see", but one can "see" more.

The formula (2.1.30) suggests that the calculation of the cross section factorises into a convolution of two non-perturbative factors associated with the initial state hadrons and a perturbative factor associated with the hard subprocess. This scheme is called *factorisation*. The factorisation in hadron-hadron collisions is used extensively to calculate cross sections with different hard subprocesses. We will show few applications of (2.1.30) in later sections of the thesis. However factorisation was proven only for a limited number of them like for example Drell-Yan production of an electroweak gauge boson [5]. The reason why the factorisation can for some processes fail is that we are dealing with scattering of hadronic objects which can interact with QCD particles such as gluons and quarks. If quarks or gluons appear in the final state they can interact with one of the protons. Such interaction in principle unsuppressed can lead to a violation of factorisation. A detailed analysis of such effects has been done in [6].

Chapter 3

Evolution equations

In the previous section 2 we have come to conclusion that Bjorken scaling in deep inelastic scattering is broken and PDFs depend not only on x , which is proton momentum fraction carried by the hard subprocess initiating parton, but also on the hard scale Q^2 . Bjorken scaling is broken by contribution from graphs with additional parton radiation (see figure 2.1.7). Since every extra radiation of a parton gives rise to a large logarithmic correction it is needed to resum all the dominant contributions from all possible graphs. This is done by the evolution equation for PDFs called the DGLAP [7] equation. The DGLAP equation is an integro-differential equation for the Q^2 dependence of the PDFs. In the next section we will describe the DGLAP equation and its application to parton shower programs.

Monte Carlo programs like PYTHIA [8], HERWIG [9], SHERPA [10] and many others use solutions of DGLAP equation to generate exclusive final states by assuming a probabilistic interpretation of the Altarelli-Parisi kernel. In the approach called *parton shower* single parton emissions are generated satisfying momentum conservation and with finite transversal momentum of the emitted parton. Note that the splitting kernel of the DGLAP equation is derived in limit in which the transversal momentum of the emitted partons is very small. Numerical methods which use parton shower solutions of the DGLAP equation go beyond this limit. We will discuss these methods in more detail.

3.1 The DGLAP evolution equation and its Monte Carlo implementation

In this section we will discuss how one obtains transversal momenta of the initial state partons of the hard subprocess in the framework of the evolution equation DGLAP, although the DGLAP equation is based on collinear factorisation and holds for integrated PDFs.

To show how can be the DGLAP equation interpreted probabilistically we will derive it entirely as an equation for a probability distribution of finding a parton inside a proton with a proton momentum fraction x and at a scale squared q^2 .

The collinear factorisation is based on the observation that by having a general parton-

scattering process with n external legs and by making an i -th leg with four-momentum p_i collinear to a j -th one with four-momentum p_j the amplitude squared of such process factorises into amplitude squared of parton-scattering process with $(n - 1)$ external legs with partons i and j replaced by parton k with four-momentum $p_k = p_i + p_j$, the propagator of the parton k , a factor of α_S and a function of the momentum fraction $z - P_{k \rightarrow ij}(z)$ called Altarelli-Parisi splitting function. One can express it a form of

$$\lim_{\theta_{ij} \rightarrow 0} |\mathcal{M}^n|^2 = \frac{\alpha_S}{\pi p_k^2} P_{k \rightarrow ij}(z) |\mathcal{M}^{(n-1)}|^2 \quad (3.1.1)$$

The momentum fraction z defines how much of the momentum p_k is carried away by the parton j .

The function

$$\frac{\alpha_S}{\pi p_k^2} P_{k \rightarrow ij}(z) dz dp_k^2 \quad (3.1.2)$$

depends on flavour of the partons i and j and can be interpreted as a probability of the parton of flavour k to split into partons i and j in which j is carrying fraction z of the momentum p_k away. One can push the probability interpretation further and find an expression for the probability of no-emission of a parton in an scale interval (q_0, q) with any fraction of momenta p_k emission of a parton after an interval in which no splitting happened. However, one has to keep in mind that a probabilistic interpretation is valid only at leading logarithmic accuracy. To go beyond leading order, the renormalisation group equation formalism is more useful, although there has been some progress in constructing a parton shower algorithm at NLO accuracy [11].

One can calculate the expression for the probability of no-emission in the scale interval (q_0, q) by cutting it into small infinitesimal pieces and expressing the probability of no emission of a parton in a infinitesimal interval as

$$\mathcal{P}_l = 1 - \frac{\alpha_S dq^2}{\pi q^2} dz P_{k \rightarrow ij}(z) \quad (3.1.3)$$

when one then multiplies each probability 3.1.3 in each interval, one obtains

$$\Delta_{k \rightarrow ij}(q_0, q) = \prod_{l=0}^{\infty} \mathcal{P}_l|_{(q_l, q_l + dq_l)} = \exp \left(- \int_{q_0^2}^{q^2} \frac{dq'^2}{q'^2} \frac{\alpha_S}{\pi} \int_{\frac{Q_0^2}{q'^2}}^{1 - \frac{Q_0^2}{q'^2}} dz P_{k \rightarrow ij}(z) \right) \quad (3.1.4)$$

called also Sudakov form factor¹. We have to point out that we have introduced an infrared cut-off for the upper and lower limits of integration over z . One can obtain this form of the cut-offs by considering a lowest possible mass Q_0 of any particle in the process. We will derive it later, but first we will discuss the assumptions behind the derivation of splitting functions. The splitting functions are derived with an assumption that virtuality

¹The name Sudakov form factor originates from work of author of [12] on QED radiation.

of the parton k with p_k^2 is much bigger than the virtuality parton j with $p_j - p_k^2 \gg p_j^2$. The parton i is assumed to be on-shell with virtuality equal to zero. In fact in the calculation of the splitting function $P_{k \rightarrow ij}(z)$ also the virtuality of parton j is taken to be infinitesimally small – $p_j^2 \sim 0$. The plus and minus components in the lightcone decomposition of the particle momenta in the splitting process are related by these equations

$$\begin{aligned} p_k^- &= \frac{p_k^2}{2p_k^+}, \\ p_j^- &= \frac{p_j^2 + \mathbf{p}^2}{2zp_k^+}, \\ p_i^- &= \frac{p_i^2 + \mathbf{p}^2}{2(1-z)p_k^+} \end{aligned} \tag{3.1.5}$$

where \mathbf{p} is the transverse momentum of one of the daughters of parton k . The minus components are related by four-momentum conservation equation

$$p_k^- = p_j^- + p_i^-, \tag{3.1.6}$$

After applying (3.1.5) to (3.1.6) we get an equation for the virtualities of the partons i, j and k, z and \mathbf{p}^2

$$z(1-z)p_k^2 - (1-z)p_j^2 - zp_i^2 = \mathbf{p}^2. \tag{3.1.7}$$

The condition for \mathbf{p}^2 to be positive will give us kinematic limit for z depending on the virtualities of the partons. We expect p_i to be on-shell with a small mass Q_0 , p_j to be off-shell with small virtuality and p_k off-shell with positive virtuality. From this assumptions and by replacing p_k^2 with q^2 we get

$$z < 1 - \frac{Q_0^2}{q^2}. \tag{3.1.8}$$

If we would let parton i play the role of the fragmenting parton we would get an inequality restricting the lower limit of the integral in (3.1.4)

$$z > \frac{Q_0^2}{q^2}. \tag{3.1.9}$$

The partons i and j carry small virtuality and are able to radiate other partons and by doing it repeatedly they reduce their virtuality. We say that the partons evolve from higher to lower virtuality. When the parton radiates a certain number of partons its virtuality – the scale variable reaches a value close to Λ_{QCD} . Since the coupling constant $\alpha_S = \alpha_S(q^2)$ is a function of the scale its value increases with number of radiated partons and reaches value for which the perturbation theory is not applicable. The parton hadronizes and can be described only by a non-perturbative object – the *fragmentation function* of a hadron H and parton $j - d_{Hj}(x, q^2)$ which describes what fraction of momenta of the parton is

carried away by the hadron. The equation which describes the evolution process is called evolution equation and has this form

$$d_{Hk}(x, q^2) = d_{Hk}(x, q_0^2) + \sum_j^{n_{pf}} \int_{q_0^2}^{q^2} \frac{dq'^2}{q'^2} \frac{\alpha_S}{\pi} \int_x^{1-\frac{Q_0^2}{q'^2}} dz \int_0^1 dx' P_{j \rightarrow ik}(x/x') d_{Hj}(x', q'^2) \Delta(q_0, q') \delta(zx' - x), \quad (3.1.10)$$

where $\Delta(q_0, q')$ is defined by

$$\Delta(q_0, q') = \prod_{k,j}^{n_{pf}} \Delta_{k \rightarrow ij}(q_0, q'), \quad (3.1.11)$$

number of parton flavours is labeled n_{pf} .

We have to point out that equation (3.1.12) is derived by assuming *forward evolution* starting from a lower scale where we know an initial condition for the fragmentation function $d_{Hk}(x, q_0^2)$. The splitting functions in such case differ from those introduced in previous paragraph, because we assume that parton j splits into partons i and k which carry fraction fractions of parton j momentum $1 - z$ and z respectively. The strong ordering of the virtualities is the same as by assuming evolution from higher scales to lower scales.

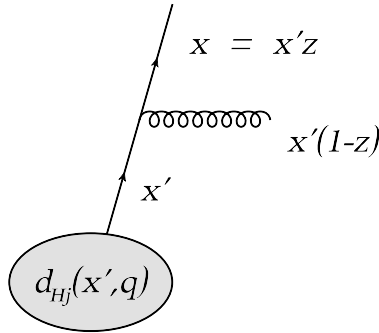


Figure 3.1.1: On the momenta variables of splitting.

The figure 3.1.1 explains the variables over which one integrates in the equation (3.1.10). Obviously one has to integrate over all possible fragmented parton momentum fractions x' and all possible fractions of momenta carried away by the emitted parton z .

After performing the integral over x' we get the well known form of the DGLAP equation

$$d_{Hk}(x, q^2) = d_{Hk}(x, q_0^2) + \sum_j^{n_{pf}} \int_{q_0}^q \frac{dq'^2}{q'^2} \frac{\alpha_S}{\pi} \int_x^{1-\frac{Q_0^2}{q'^2}} \frac{dz}{z} P_{k \rightarrow ij}(z) d_{Hj}(x/z, q'^2) \Delta_i(q_0, q'). \quad (3.1.12)$$

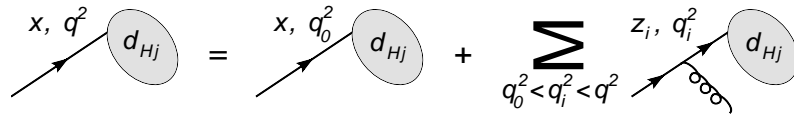


Figure 3.1.2: Schematic picture of the DGLAP equation.

This equation describes the radiation from the final state particles and describes the evolution of the fragmentation function $d_{Hi}(x, q^2)$. The same equation can be obtained by writing the renormalisation group equation for $d_{Hi}(x, q^2)$ since it is a description of the renormalisation scale dependence of the fragmentation function.

One can write a similar equation for the the initial state radiation which describes the evolution of the *parton density functions* (PDFs). PDFs at leading order can be interpreted as probabilities of finding a parton of certain flavour in the colliding hadron. The DGLAP equation for PDFs $f_i(x, q^2)$ reads

$$f_j(x, q^2) = f_j(x, q_0^2) + \sum_k^{n_{pf}} \int_{q_0}^q \frac{dq'^2}{q'^2} \frac{\alpha_S}{\pi} \int_x^{1-\frac{q_0^2}{q'^2}} \frac{dz}{z} P_{k \rightarrow ij}(z) f_k(x/z, q'^2) \Delta_i(q_0, q'). \quad (3.1.13)$$

The interpretation of the equation (3.1.13) is similar to the interpretation of the equation (3.1.12).

The DGLAP equation can be solved on a grid in x, Q^2 space [13] or by an other method in which the integral of the right-hand side is evaluated using numerical integration. It can be also analytically solved using Mellin transform of the equation derivated in q^2 [14] where the right-hand side integral results into a simple product of Mellin transforms of functions in the integrand. Equations (3.1.12) and (3.1.13) can be implemented into Monte Carlo showering program. We will describe the implementation in next chapter.

3.1.1 The implementation of the DGLAP equation for initial state parton shower

There are two possibilities how to proceed by generating the emissions according to the DGLAP equation using a Monte Carlo method.

The idea of the so called *forward evolution* is to generate the emissions using probability

$$\Delta_i(q_0, q) \frac{\alpha_S}{\pi} \frac{dz}{z} \frac{dq^2}{q^2} P_{k \rightarrow ij}(x/z). \quad (3.1.14)$$

going from a low scale q_0 to a higher scale q . The advantage of *forward evolution* algorithm for the initial state parton shower is that one starts at a nonperturbative value of the scale and by generating parton emissions one increases the value of the scale to the scale of the hard subprocess. Such a evolution seems to be more natural and on first

sight more straightforward than the backward evolution, but has a big drawback by being very ineffective. We will shortly sketch the reason for the ineffectiveness. Let us start the evolution algorithm by choosing the proton momentum fraction of the struck parton x at the scale q_{min} . We can now directly use the veto algorithm to produce emissions distributed according to the emission probability obtained from DGLAP equation. After reaching the hard subprocess scale one is left with a point of phase space of the hard partonic subprocess. The problem is that it is not clear if the hard subprocess can happen in the reached phase space point. The *forward evolution* algorithm does not take into account kinematical constraints on the hard subprocess. In practice it often happens that the point in which the evolution stopped is kinematically not allowed for the hard subprocess and whole event has to be discarded.

The idea of the *backward evolution*, which was for the first time constructed in [15], is to first generate the four-momenta of the particles involved in the hard subprocess and then use the probability

$$\tilde{P}_{k \rightarrow ij}(x, z, q, q') = \frac{dq^2}{q^2} \frac{\alpha_S}{2\pi} dz P_{k \rightarrow ij}(x/z) \frac{f_k(x/z, q')}{f_j(x, q)} \Delta'(q, q', x, z). \quad (3.1.15)$$

to generate every single parton radiation in the chain. Notice that in the formula used in the (3.1.15) is not used simple PDF of the starting parton, but a ratio of PDFs of before and after parton radiation. This arrangement leads to a so called modified Sudakov form factor $\Delta'(q, q', x, z)$ and reproduces the correct PDF after a *backward evolution*. To see this one has to realise that by knowing the PDF in the point (x, q) corresponding to j -th emission of the parton the next $(j + 1)$ -th emission is at scale value $q + dq$ with fraction of the mother parton momentum z .

It is useful to point out that this probability distribution describes a *backward evolution* – by adding a parton emission one goes down to a lower value of the evolution scale $q' < q$. The modified splitting function $\tilde{P}_{k \rightarrow ij}(x, z, q, q')$ is schematically described in Figure 3.1.1.

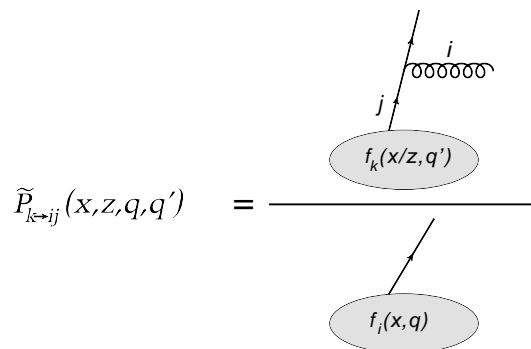


Figure 3.1.3: Schematic picture describing the modified splitting function.

The advantage of the *backward evolution* algorithm is that it generates the endpoints of parton shower chains already distributed according to the partonic cross section and then

generates the parton shower in such way that the starting point is distributed according to the corresponding PDF.

If we know the function (3.1.15) we can use standard methods to generate random values of q^2 and z according to this distribution. In general is the function $\Delta(q_0, q, x, z)$ too complicated to be expressed in analytical form. Fortunately there is a way to generate the desired distribution without tabulating the Sudakov form factor. To generate random numbers according to the distribution (3.1.15) we can use the fact that the Sudakov form factor is just a exponent of an integral of the distribution [16]. To obtain the exponentiated distribution we have to apply so called *veto algorithm* [8].

After generating all n emissions according to *backward evolution* algorithm, described in previous paragraphs, and reaching the cut-off scale q_{min} one is left with set of pairs of values $\{(z_1, q_1), (z_2, q_2), \dots, (z_n, q_n)\}$. We assume that for every $i \in 1, \dots, n$ $q_i = q_i(z_i, |\mathbf{p}_i|)$, where \mathbf{p}_i is the transverse two-momentum of the i -th emitted parton.

This set of values contains almost the whole information about the momenta of the emitted partons. Using the information from the pair (z_i, q_i) and the on-shell condition for the emitted parton one can reconstruct the whole 4-momentum p_i . The 4-momentum of the emitted parton can be written as follows

$$p_i = (1 - z_i)p_k + y_i n_i + p_{i\perp} \quad (3.1.16)$$

where $p_{i\perp}$ is the transversal four-momentum of the emitted parton, n_i is an auxiliary ligh-like four-momentum satisfying condition $n_i \cdot p_k > 0$ for every k , y_i is momentum fraction in the direction of n . This kind of decomposition is called Sudakov decomposition. On-shell condition $p_i^2 = 0$ using equation (3.1.16) reads (for a massless parton)

$$y_i = \frac{\mathbf{p}_i^2 / (1 - z_i) - (1 - z_i) p_k^2}{2 p_k \cdot n_i}. \quad (3.1.17)$$

To calculate the momenta in the chain one needs the complete information about the vector of the transversal momentum. This can be done by generating a set of polar angles $\{\phi_1, \phi_2, \dots, \phi_n\}$. We can neglect correlations between the polar angles ϕ_i and generate them randomly independent on each other. The transverse momentum of an i -th parton can be then calculated form q_i , z_i and azimuthal angle ϕ_i

$$\mathbf{p}_i = (|\mathbf{p}_i|(q_i, z_i) \cos \phi_i, |\mathbf{p}_i|(q_i, z_i) \sin \phi_i). \quad (3.1.18)$$

We can also calculate the momentum of the recoiled parton ij simply from momentum conservation

$$p_j = p_k - p_i. \quad (3.1.19)$$

In this setup the parton taking part in the hard scattering subprocess will be off-shell by order of $\sim q_0$.

It can be easily shown by trying to solve the DGLAP equation iteratively that it sums terms proportional to $[\alpha_S \ln(q^2/q_0^2)]^n$ for every n . In the next chapters we will show how to go beyond this logarithmic approximation by including terms proportional to $[\alpha_S \ln(1/x)]^n$.

However, the parton shower algorithm goes beyond the standard collinear approximation, since it generates finite transversal momentum of the exclusive final state and resums part of the subleading corrections. The scale dependence of the PDFs is reproduced according to the correct DGLAP equation.

3.2 k_{\perp} -factorisation

3.2.1 Motivation for use of k_{\perp} -dependent PDFs

In the section 2 we have discussed some of the collider types and phenomenological approaches to describe them. In a case when at least one of the colliding particles is a hadron we have found that the cross section will be a convolution of a non-perturbative factor for each of the hadrons colliding and a perturbative factor which describes the subprocess at a hard scale μ^2 . The non-perturbative factors are called parton density functions (PDFs). PDFs have a perturbative component because they can be evolved from a low scale, which has to be determined non-perturbatively, to higher scale by perturbative calculation. The PDF of a certain parton species i is a function of the proton momentum fraction x carried by the parton and the scale at which is the hard partonic process happening.

There are some kinematics approximations in the pictured scheme. Let us take as the hard subprocess in a proton-proton collision to be bottom-antibottom quark pair production: $pp \rightarrow X + b\bar{b}$. The hard scale in this process is formally ensured by the mass of the bottom quark, but there are more adequate choices for the hard scale μ^2 since also the invariant mass of the $b\bar{b}$ -pair or the transverse momentum of one the b -quarks can be much larger than their mass. Now let us investigate the transverse momentum \mathbf{p}_b , of the b -quark or \bar{b} -quark. We find a distribution with a turn-over around the b -quark mass. The cross section is finite because the collinear singularities are regulated by the bottom quark mass m_b . The cross section falls like $1/\mathbf{p}_b^2$ for high transverse momenta \mathbf{p}_b^2 . For now we are not interested in the low \mathbf{p}_b behaviour where the cross section is finite, but in the high \mathbf{p}_b behaviour. The cross section of the \mathbf{p}_b distribution is governed dominantly by the partonic cross section for the $b\bar{b}$ -production. For large \mathbf{p}_b we can neglect the mass of the b -quark

$$\frac{d\sigma}{d\Omega}(gg \rightarrow b\bar{b})\Big|_{1/\mathbf{p}_b^2 \rightarrow 0} \approx \frac{\alpha_S^2}{32\hat{s}}(\hat{t}^2 + \hat{u}^2) \left(\frac{1}{\hat{t}\hat{u}} - \frac{9}{4\hat{s}^2} \right). \quad (3.2.1)$$

After introducing the variable $\beta = \mathbf{p}_b^2/\hat{s}$ and $z = \hat{t}/\hat{s}$. It can be shown that $0 < \beta < 1/4$ and $0 < z < 1$. Then by using kinematic constraints on β and z (4-momentum conservation and on-shell conditions) one finds that for fixed β there are two solutions for z : read $z_{1,2} = 1/2 \pm 1/2\sqrt{1-4\beta}$. Using these relations one can rewrite (3.2.1) into

$$\frac{d\sigma}{d\Omega}(gg \rightarrow b\bar{b})\Big|_{1/\mathbf{p}_b^2 \rightarrow 0} \approx \frac{\alpha_S^2}{64} \frac{(1-2\beta)(4-9\beta)}{\mathbf{p}_b^2} \sim \frac{1}{\mathbf{p}_b^2}. \quad (3.2.2)$$

Other channels with quarks in the initial state are suppressed by electroweak coupling or small PDFs compared to the gluon PDF. This is definitely true for the LHC energies where gluon channel dominates for most of the processes. However, let us concentrate now on the transverse momentum of the $b\bar{b}$ pair $\mathbf{p}_{b\bar{b}}$, the magnitude of the total transverse momentum of the pair. If one takes the leading order approximation for the hard subprocess matrix element and naively applies the formula (2.1.30) one obtains that the transverse momentum $\mathbf{p}_{b\bar{b}} = 0$. The interpretation of this result is that leading order approximation - α_S^2 - for the hard matrix element is not the leading order approximation for the observable $\mathbf{p}_{b\bar{b}}$. The

leading order approximation for an observable is the first approximation in the series which gives a non-zero value for the observable. The perturbation series for the observable $\mathbf{p}_{b\bar{b}}$ starts at α_S^3 order. Diagrams with real emission corrections generate transverse momentum of the $b\bar{b}$ pair so the total transverse momentum of the $b\bar{b}i$, where i is an extra parton emission, is again 0. The problem is solved and if one wants to approximate the observable $\mathbf{p}_{b\bar{b}}$ better, all one needs is to invest enough effort to go to higher and higher orders of the perturbation theory. However if one looks at $\mathbf{p}_{b\bar{b}i}$ one sees that it diverges at $\mathbf{p}_{b\bar{b}i} = \mathbf{0}$, because of the collinear divergence connected to the fact that i is massless, and thus is unphysical. The singularity is compensated by the virtual correction, but does not change the fast growing behaviour of the cross section with $\mathbf{p}_{b\bar{b}i} \rightarrow \mathbf{0}$. The leading order for $\mathbf{p}_{b\bar{b}i}$ is definitely not enough.

The sketched problems rise the question if the picture is consistent and if one cannot do better. To answer these questions we have to go back to formulation of the parton model and look in detail what is happening in the derivation of the factorisation formula like (2.1.30).

What was actually done in the derivation of the formula (2.1.30) was that the correlation between the transversal momentum of the transverse momentum dependence in the PDFs and transverse momentum of colliding partons in the initial state of the hard matrix element was neglected, because it is expected to be small comparing to the hard scale. Then the transverse momentum in the hard matrix element can be integrated out independently on the PDFs and the transverse momentum dependence in the PDFs can be integrated out independently on the hard matrix element. The result is that the matrix element and the PDFs do not depend on the transverse momenta of the initial state partons. These partons are on-mass shell so the gauge invariance of the hard matrix element is easily guaranteed. Obviously, by applying such approximations we are losing information about the transverse momentum structure of partonic content of proton and we are losing connection to the kinematics of the hard particles. How adequate is it to acquire for the lost information by fixed order perturbation theory is a complicated question.

In this chapter we will present approaches which go beyond the fixed order approximation for the transverse momentum of the hard subprocess final state. One of the approaches, called k_\perp -factorisation, addresses also the transverse momentum dependence of the hard matrix element. We will discuss this approach in more detail for different processes. The problem is closely related to evolution equations for PDFs and to their parton shower interpretation, so, the next sections of the thesis will be dedicated to their discussion with focus on the treatment of the kinematics of the hard subprocess. For this purpose we will study the transverse momentum of the Z boson.

3.3 The BFKL evolution equation

The BFKL equation found by [17] deals with a situation in which the total collision energy squared s is much larger than the exchanged momentum squared $|t|$: $s \gg |t|$. In such a situation logarithmic terms of the form $[\alpha_S \log(1/x)]^n$ are large because the momentum fraction x is small – $x \sim \sqrt{|t|/s} \ll 1$ [18]. These logarithmic terms, not taken into account by the DGLAP equation, are resummed by the BFKL equation. Despite the fact that the BFKL equation is suitable only for inclusive calculations, it will be useful to describe the ideas which are behind it. It will allow us to discuss the CCFM equation, which represents an interpolation between the DGLAP and the BFKL equations, in the next chapter.

The derivation of the BFKL equation (we will summarise the argumentation in [19]) follows from observation that the leading small- x logarithmic contribution can be summed by assuming *multi-regge kinematics* [17]. In the multi-regge kinematic regime for three subsequent emissions of partons, $i-1$, i and $i+1$ as depicted in the figure 3.3.1, invariant masses $s_{i-1,i}$ of emitted partons $i-1$ and i , and $s_{i,i+1}$ of emitted partons i and $i+1$ are both much smaller than the invariant mass $s_{i-1,i+1}$ of the pair $i-1$ and $i+1$ – $s_{i-1,i} \sim s_{i,i+1} \ll s_{i-1,i+1}$. This automatically implies ordering of the Sudakov components of momenta of the emitted partons. If the momenta of the emitted parton k is

$$q_k = \alpha_k p_A + \beta_k p_B + q_{k\perp}, \quad (3.3.1)$$

where p_A and p_B are light-like initial state particle momenta, then

$$1 \gg \alpha_i \gg \alpha_{i+1}, \quad \beta_i \ll \beta_{i+1} \ll 1. \quad (3.3.2)$$

On the other hand the transversal momenta of the emitted partons can be of the same order $\mathbf{q}_i \sim \mathbf{q}_{i+1}$. We can see, that in contrary to the situation in the kinematic regime under which the DGLAP equation was derived, the transverse momenta in *multi-regge regime* are not ordered.

Since the Sudakov variables are directly related to the rapidity of the partons, the emitted partons are strongly ordered in rapidity.

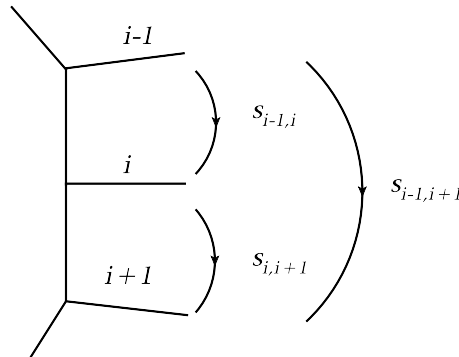


Figure 3.3.1: Multi-regge kinematics.

It is easy to see that the *multi-regge* regime satisfies the condition $s \gg |t|$ for the four-momenta p_A and p_B . Because of the strong ordering, in the case when the emitted parton couples to another external parton (next in order), one can approximate the coupling by eikonal coupling

$$-ig_S\lambda^a \bar{u}_{\xi'}(q_i - q_{i+1})\gamma^\mu u_\xi(q_i) = -ig_S\lambda^a 2q_i^\mu \delta_{\xi'\xi} + \mathcal{O}\left(\frac{\mathbf{q}_{i+1}^2}{s}\right). \quad (3.3.3)$$

To see how *multi-regge kinematics* applies in praxis we can examine it at the lowest order of the perturbation series. The lowest order α_S contribution to the amplitude of quark-quark scattering is obtained by calculating the tree Feynman diagram in figure 3.3.2 in which the eikonal coupling is denoted by empty circles. We can use the eikonal approximation because momentum exchange $t = k^2$ is much smaller than the collision energy squared. We can go to higher orders by adding real and virtual corrections, see figure 3.3.3.

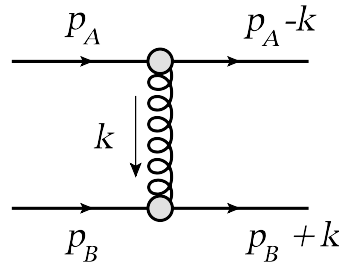


Figure 3.3.2: Leading contribution to process $qq \rightarrow qq$.

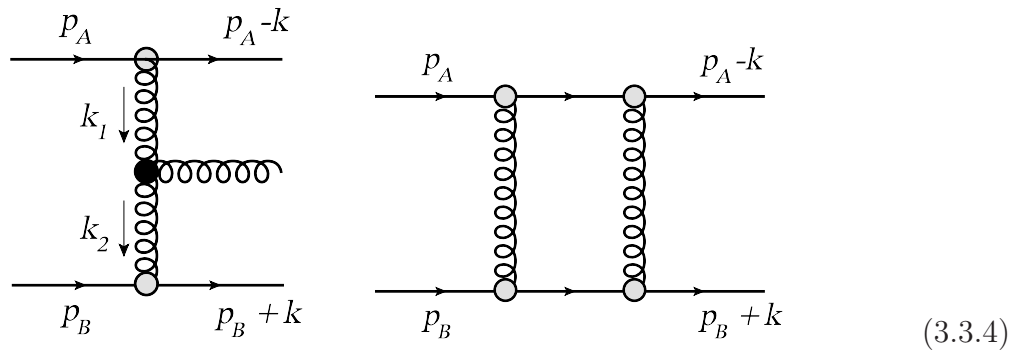


Figure 3.3.3: Next to leading contribution to process $qq \rightarrow qq$.

The polarisations of the initial state and final state are labeled ξ and ξ' respectively. In front of the quark spinors $u_\xi(p_A)$ and $\bar{u}_{\xi'}$ there is a factor consisting of the strong coupling

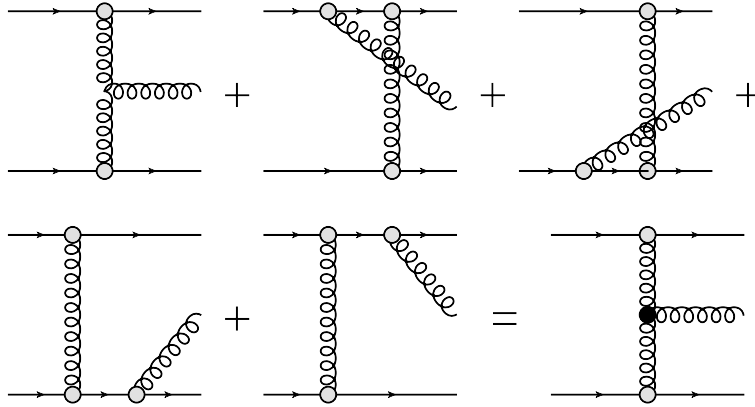


Figure 3.3.4: Emergence of Lipatov effective vertex.

constant g_S and colour factor λ_a . The vertex in this approximation preserves spin of the quark. It can be shown that the expression for this *eikonal vertex* does not depend on the spin of the initial/final state particle which. This is consistent with our assumptions from the beginning of the chapter.

If we take the leading term of (3.3.3) for upper and lower quark-gluon vertex, we can write the expression for the leading order amplitude of the process $qq \rightarrow qq$ in *multi-regge kinematics* (in Feynman gauge)

$$\mathcal{A}_{2 \rightarrow 2}^0 = i4\pi\alpha_S\lambda^a \otimes \lambda^a \frac{s}{\mathbf{k}^2} \delta_{\xi'\xi}\delta_{\zeta'\zeta} \quad (3.3.5)$$

where λ^b , ζ' and ζ are the colour factor for the lower quark-gluon vertex and labels of the polarisation of the lower quark respectively.

To calculate the next order of the perturbation series we have to calculate the amplitudes corresponding to diagrams in figure 3.3.3.

The contribution from the diagrams 3.3.4 can be summed into an three-gluon effective vertex

$$\Gamma_{\sigma\tau}^\nu(k_1, k_2) = \frac{2p_{A\tau}p_{B\sigma}}{s} \left(-\frac{2\mathbf{k}_1^2}{\beta_S} p_A^\nu + \frac{2\mathbf{k}_2^2}{\alpha_S} p_B^\nu - (k_{1\perp} + k_{2\perp})^\nu \right) \quad (3.3.6)$$

This expression has to be contracted with effective eikonal vertices of gluon-quark coupling.

One can show that summing virtual corrections to the propagator (all relevant virtual corrections in the leading order) results into dressing the bare gluon propagator by a Regge factor [19, 20]

$$-i\frac{g^{\mu\nu}}{k^2} \rightarrow -i\frac{g^{\mu\nu}}{k^2} \left(\frac{s}{|t|} \right)^{\epsilon_R(-\mathbf{k}^2)} \rightarrow -i\frac{g^{\mu\nu}}{k_{i+1}^2} \left(\frac{\alpha_i}{\alpha_{i+1}} \right)^{\epsilon_R(-\mathbf{k}_{i+1}^2)} \quad (3.3.7)$$

where

$$\epsilon_R(-\mathbf{k}^2) = \frac{N_C\alpha_S}{4\pi^2} \int d^2\kappa \frac{\mathbf{k}^2}{\kappa^2(\mathbf{k}-\kappa)^2}. \quad (3.3.8)$$

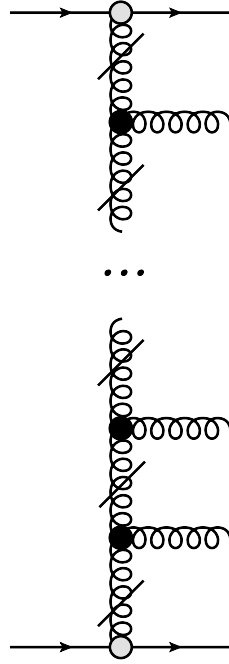


Figure 3.3.5: A gluon emission ladder with virtual corrections.

The modification of the gluon propagator described in relation (3.3.7) is called *reggeisation* of the gluon. *Reggeisation* of the gluon has to be proven for consistency since it is not clear if the reggeisation factor includes all the virtual corrections when considering a whole chain of gluon emissions.

By generalising the above calculations for n real emissions corrections and all the corresponding virtual corrections one finds that the amplitude exponentiates and factorises. The expression for amplitude $\mathcal{A}_{2 \rightarrow (n+2)}^{(8)\sigma_1 \dots \sigma_n}$ has this form

$$\begin{aligned} \mathcal{A}_{2 \rightarrow (n+2)}^{(8)\sigma_1 \dots \sigma_n} &= i2sg^{n+2} \delta_{\lambda'_A \lambda_A} \delta_{\lambda'_B \lambda_B} G_n^{(8)} \frac{i}{\mathbf{k}_1^2} \left(\frac{1}{\alpha_1} \right)^{\epsilon_R(-\mathbf{k}_1^2)} \\ &\times \prod_{i=1}^n \frac{2p_A^{\mu_i} p_B^{\nu_i}}{s} \Gamma_{\mu_i \nu_{i+1}}^{\sigma_i}(k_i, k_{i+1}) \frac{i}{\mathbf{k}_{i+1}^2} \left(\frac{\alpha_i}{\alpha_{i+1}} \right)^{\epsilon_R(-\mathbf{k}_{i+1}^2)} \end{aligned} \quad (3.3.9)$$

Using the expression (3.3.9) we can calculate the imaginary part of the octet exchange amplitude using the dispersion relation. It is possible then to write the equation for the octet exchange amplitude and prove the consistency of *reggeisation* of gluon. However to derive the BFKL equation one has to calculate the amplitude for colour singlet exchange scattering. The colour singlet amplitude will not include the tree level diagram (3.3.5) contribution and virtual contributions will carry different colour factors. The steps which lead to the derivation of the BFKL equation are similar to those which were described above for an octet exchange case. The BFKL equation can be most conveniently written

for a Mellin transform of the colour singlet exchange amplitude $\mathcal{A}^{(1)}(s, t)$

$$\int_1^\infty d\left(\frac{s}{\mathbf{k}^2}\right) \left(\frac{s}{\mathbf{k}^2}\right)^{-\omega-1} \frac{\mathcal{A}^{(1)}(s, t)}{s} = 4i\alpha_S^2 \delta_{\lambda'_A \lambda_A} \delta_{\lambda'_B \lambda_B} G_0^{(1)} \quad (3.3.10)$$

$$\times \int \frac{d^2 \mathbf{k}_1 d^2 \mathbf{k}_2}{\mathbf{k}_2^2 (\mathbf{k}_1 - \mathbf{q})^2} f(\omega, \mathbf{k}_1, \mathbf{k}_2, \mathbf{q})$$

where \mathbf{q} is the transversal component of the momentum exchanged between scattered particles A and B .

The equation for the quantity $f(\omega, \mathbf{k}_1, \mathbf{k}_2, \mathbf{q})$ then reads

$$(\omega - \epsilon_R(-\mathbf{k}_1^2) - \epsilon_R(-(\mathbf{k}_1 - \mathbf{q})^2)) f(\omega, \mathbf{k}_1, \mathbf{k}_2, \mathbf{q}) = \delta^2(\mathbf{k}_1 - \mathbf{k}_2) - \frac{N_C \alpha_S}{2\pi^2} \int d^2 \mathbf{k}' \left[\frac{\mathbf{q}^2}{(\mathbf{k}' - \mathbf{q})^2 \mathbf{k}_1^2} - \frac{1}{(\mathbf{k}' - \mathbf{k}_1)^2} \left(1 + \frac{(\mathbf{k}_1 - \mathbf{q})^2 \mathbf{k}'^2}{(\mathbf{k}' - \mathbf{q})^2 \mathbf{k}_1^2} \right) \right] f(\omega, \mathbf{k}', \mathbf{k}_2, \mathbf{q}). \quad (3.3.11)$$

The equation (3.3.11) has an important property that it is infrared finite. We are interested in the case when $\mathbf{q} = \mathbf{0}$ and in such a case the equation simplifies to

$$(\omega - 2\epsilon_R(-\mathbf{k}_1^2)) f(\omega, \mathbf{k}_1, \mathbf{k}_2, \mathbf{0}) = \delta^2(\mathbf{k}_1 - \mathbf{k}_2) + \frac{N_C \alpha_S}{\pi^2} \int d^2 \mathbf{k}' \frac{f(\omega, \mathbf{k}', \mathbf{k}_2, \mathbf{0})}{(\mathbf{k}' - \mathbf{k}_1)^2} \quad (3.3.12)$$

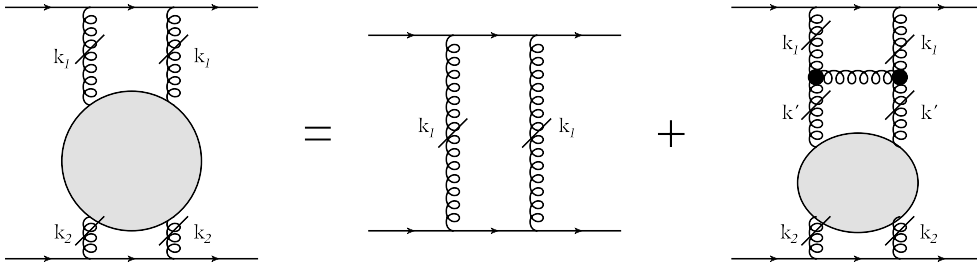


Figure 3.3.6: BFKL equation for $q^2 = 0$ momentum exchange.

We will use this form of the BFKL (3.3.12) equation to rewrite it in a way more similar to the DGLAP, identifying a splitting function, a form factor and a gluon density. For this purpose we will define a Regge form factor by equation [19, 21]

$$\ln \Delta_R(z, \mathbf{k}^2) = -\frac{N_C \alpha_S}{\pi} \int_z^1 \frac{dz'}{z'} \int \frac{d^2 \mathbf{q}'}{\pi \mathbf{q}'^2} \theta(|\mathbf{q}'| - \mu) \theta(|\mathbf{k}| - |\mathbf{q}'|) = 2 \ln(1/z) \epsilon_R(-\mathbf{k}^2). \quad (3.3.13)$$

The regge form factor includes all the contributions from the virtual corrections. Note that we have inserted a collinear cut-off μ for the integration over \mathbf{q}' , although, as we mentioned before, the BFKL equation is infrared finite. The dependence on μ cancels

between the virtual and real corrections for inclusive quantities, but does not cancel for exclusive quantities and is important for the formulation of a Monte Carlo algorithm based on the BFKL equation [22, 23].

The equation (3.3.12) simplifies if we use the fact that

$$\frac{1}{\omega - 2\epsilon_R(-\mathbf{k}^2)} = \int_0^1 \frac{dz}{z} z^\omega \Delta_R(z, \mathbf{k}^2). \quad (3.3.14)$$

Using equation (3.3.14) the equation (3.3.12) turns into

$$\begin{aligned} f(\omega, \mathbf{k}_1, \mathbf{k}_2, \mathbf{0}) &= \delta^2(\mathbf{k}_1 - \mathbf{k}_2) \int_0^1 \frac{dz}{z} z^\omega \Delta_R(z, \mathbf{k}^2) \\ &+ \frac{N_C \alpha_S}{\pi^2} \int \frac{d^2 \mathbf{k}'}{(\mathbf{k}' - \mathbf{k}_1)^2} \int_0^1 \frac{dz}{z} z^\omega \Delta_R(z, \mathbf{k}^2) f(\omega, \mathbf{k}', \mathbf{k}_2, \mathbf{0}) \theta(|\mathbf{q}'| - \mu) \end{aligned} \quad (3.3.15)$$

If we define $\mathbf{q}' = \mathbf{k}' - \mathbf{k}$, $\mathbf{k}_1 = \mathbf{k}$ we get

$$\begin{aligned} f(\omega, \mathbf{k}, \mathbf{k}_2, \mathbf{0}) &= \delta^2(\mathbf{k} - \mathbf{k}_2) \int_0^1 \frac{dz}{z} z^\omega \Delta_R(z, \mathbf{k}^2) \\ &+ \frac{N_C \alpha_S}{\pi^2} \int \frac{d^2 \mathbf{q}'}{\mathbf{q}'^2} \int_0^1 \frac{dz}{z} z^\omega \Delta_R(z, \mathbf{k}^2) f(\omega, \mathbf{k} + \mathbf{q}', \mathbf{k}_2, \mathbf{0}) \theta(|\mathbf{q}'| - \mu). \end{aligned} \quad (3.3.16)$$

The next step which we can do is to perform an inverse Mellin transform

$$\tilde{f}(x, \mathbf{k}, \mathbf{k}_2) = \frac{1}{2\pi i} \int_{-i\infty}^{i\infty} d\omega x^{-\omega} f(\omega, \mathbf{k}, \mathbf{k}_2, \mathbf{0}). \quad (3.3.17)$$

We get

$$\begin{aligned} \tilde{f}(x, \mathbf{k}, \mathbf{k}_2) &= \frac{1}{2\pi i} \delta^2(\mathbf{k} - \mathbf{k}_2) \int_0^1 \frac{dz}{z} \int_{-i\infty}^{i\infty} d\omega \left(\frac{x}{z}\right)^{-\omega} \Delta_R(z, \mathbf{k}^2) \\ &+ \frac{N_C \alpha_S}{\pi^2} \int \frac{d^2 \mathbf{q}'}{\mathbf{q}'^2} \int_0^1 \frac{dz}{z} \Delta_R(z, \mathbf{k}^2) \tilde{f}(x/z, \mathbf{k} + \mathbf{q}', \mathbf{k}_2) \theta(|\mathbf{q}'| - \mu) \end{aligned} \quad (3.3.18)$$

and in the last step we can evaluate the integral in the first term on the right-hand side of the equation (3.3.18). We obtain

$$\begin{aligned} \tilde{f}(x, \mathbf{k}, \mathbf{k}_2) &= x \delta^2(\mathbf{k} - \mathbf{k}_2) \Delta_R(x, \mathbf{k}^2) \\ &+ \frac{N_C \alpha_S}{\pi^2} \int \frac{d^2 \mathbf{q}'}{\mathbf{q}'^2} \int_0^1 \frac{dz}{z} \Delta_R(z, \mathbf{k}^2) \tilde{f}(x/z, \mathbf{k} + \mathbf{q}', \mathbf{k}_2) \theta(|\mathbf{q}'| - \mu) \end{aligned} \quad (3.3.19)$$

When we compare expressions for the Regge form factor in the equation (3.3.13) and Sudakov form factor in the equation (3.1.4) we can identify $1/z$ singular piece of the gluon splitting function in the Regge form factor. However by comparing equations (3.3.19) and (3.1.13) we find this splitting function missing in equation (3.3.19). In addition we have an extra factor of x in the first term on the right-hand side and also a form factor. To remove this factor and obtain the splitting function we have to redefine the quantity \tilde{f} from $\tilde{f}(x, \mathbf{k}, \mathbf{k}_2) \rightarrow x\tilde{f}(x, \mathbf{k}, \mathbf{k}_2)$. Using this change we obtain

$$\begin{aligned} \tilde{f}(x, \mathbf{k}, \mathbf{k}_2) &= \delta^2(\mathbf{k} - \mathbf{k}_2)\Delta_R(x, \mathbf{k}^2) \\ &+ \frac{N_C\alpha_S}{\pi^2} \int \frac{d^2\mathbf{q}'}{\mathbf{q}'^2} \int_0^1 \frac{dz}{z} \frac{\Delta_R(z, \mathbf{k}^2)}{z} \tilde{f}(x/z, \mathbf{k} + \mathbf{q}', \mathbf{k}_2) \theta(|\mathbf{q}'| - \mu) \end{aligned} \quad (3.3.20)$$

We can now identify the factor $1/z$ as the small z singular piece of the gluon-gluon splitting function. In the last step we will convolute the function $\tilde{f}(x, \mathbf{k}, \mathbf{k}_2)$ with an impact factor $\Phi_h(\mathbf{k}_2)$ to obtain a function $f_g(x, \mathbf{k})$ [24] which we will interpret as an *unintegrated parton density function*. The impact factor contains information about the non-perturbative structure of the colliding particle (usually a hadron h) from which the gluon undergoing a hard collision originates. We have also to realise that the integration in z must be restricted in the range from x to 1 because if z should be interpreted as the momentum fraction the ratio x/z should not be larger than 1. The final form of the BFKL equation reads

$$\begin{aligned} f_g(x, \mathbf{k}) &= \frac{\Phi_h(\mathbf{k})}{\mathbf{k}^2} \Delta_R(x, \mathbf{k}^2) \\ &+ \frac{N_C\alpha_S}{\pi^2} \int \frac{d^2\mathbf{q}'}{\mathbf{q}'^2} \int_x^1 \frac{dz}{z} \frac{\Delta_R(z, \mathbf{k}^2)}{z} f_g(x/z, \mathbf{k} + \mathbf{q}') \theta(|\mathbf{q}'| - \mu). \end{aligned} \quad (3.3.21)$$

Such a form of an integral equation, if momentum conservation taken in addition into account, allows for a probability interpretation and possibility to generate parton branchings and solve the equation in a Monte Carlo program which would allow not only for a study of the total cross section of particle scattering, but also for studies of more exclusive states. We will not study such a problem, but go a bit more further, include also the $1/(1-z)$ part of the splitting function and QCD coherence effects which are important if one wants to study exclusive final states.

3.4 The CCFM evolution equation

One of the effects neglected in the derivation of the BFKL equation is the coherence effect of QCD radiation. Coherence effect is sub-leading in the kinematical regime in which the BFKL equation is valid, but it plays a crucial role when one tries to extend the kinematical range of the BFKL equation and include contributions beyond leading logarithmic approximation. Coherence is also important for calculation of exclusive final states since it allows to correctly separate collinear logarithmic contributions from soft logarithmic contributions.

Coherence can be included into the shower by angular ordering of the emissions. A certain version of angular ordering of parton shower emissions is used also in Monte Carlo programs based on DGLAP equation like HERWIG [9] and HERWIG++ [9]. The Monte Carlo program PYTHIA takes the coherence into account by vetoing emission chains which violate the angular ordering [8].

We will discuss the emergence of the coherence in QCD and its crucial role in the derivation of the CCFM [25] equation which interpolates between the DGLAP equation and the BFKL equation by summing logarithmic terms of $1/x$ and Q^2/μ^2 . We will also discuss its implementation in the Monte Carlo generator CASCADE [26].

3.4.1 Coherence effect of the QCD radiation

One can get an intuitive feeling for the QCD coherence by considering an emission of a gluon from a colour dipole. The figure 3.4.1 shows schematically that when the angle between the decaying parton (gluon in the figure) – θ and the emitted gluon is larger than the angle between the decaying parton and one of the partons forming a dipole – θ' (gluons in the figure) the emitted gluon cannot "resolve" the dipole and can be effectively treated as emitted from the initial decaying parton.

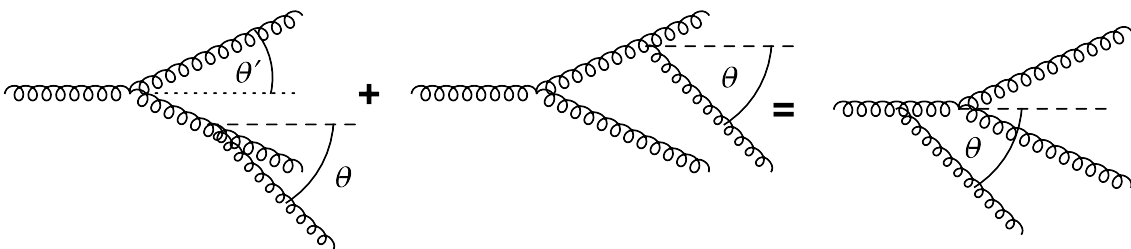


Figure 3.4.1: Soft gluon emission for $\theta > \theta'$.

One can see this behaviour on the basis of formulas by expressing the probability of an emission from a dipole. We will follow the argumentation from [16]. To derive the desired formula we will assume that the emitted gluon has a 4-momentum q which is much softer than 4-momentum of any of the external gluons. In such approximation we can use eikonal

approximation for the three-gluon vertex

$$\frac{p_I^\mu}{p_I \cdot q} \mathbf{t}_I^a \quad (3.4.1)$$

where p_I is the 4-momentum of the external leg from which is the soft gluon emitted (i labels the external partons) and \mathbf{t}_I^a is the corresponding colour charge of the external parton to which the emitted parton couples. The nominator of the expression (3.4.1) comes from the formula (3.3.3). The denominator is a factor coming from propagator which emerges after inserting an extra external line.

The amplitude of the soft emission factorises from the amplitude for the process with 3 external particles so that the amplitude for the process with 4 external particles can be written as their product. The total contribution to the factorised current in the eikonal approximation will be

$$\mathbf{J}^{a\mu}(q) = -\frac{p_I^\mu}{p_I \cdot q} \mathbf{t}_I^a + \frac{p_1^\mu}{p_1 \cdot q} \mathbf{t}_1^a + \frac{p_2^\mu}{p_2 \cdot q} \mathbf{t}_2^a \quad (3.4.2)$$

where index I means the initial decaying parton and indices 1 and 2 label the final state partons in the dipole. Every term in the equation (3.4.2) corresponds to an eikonal coupling of the soft gluon to a different leg of the diagram indicated by the lower index.

The factorised amplitude can be written as

$$\mathbf{H}(p_I, p_1, p_2, q) = \mathbf{h}(p_I, p_1, p_2) \cdot \mathbf{J}(q). \quad (3.4.3)$$

Because of factorisation we can get now the probability of the soft gluon emission in the eikonal approximation by squaring the expression for the eikonal current in equation (3.4.2)

$$\mathbf{J}^2(q) = -(2\mathbf{t}_I \mathbf{t}_1) W_{1I} - (2\mathbf{t}_I \mathbf{t}_2) W_{2I} + (2\mathbf{t}_1 \mathbf{t}_2) W_{12}. \quad (3.4.4)$$

where

$$W_{1I} = \frac{p_I \cdot p_1}{(p_I \cdot q)(p_1 \cdot q)}, \quad W_{2I} = \frac{p_I \cdot p_2}{(p_I \cdot q)(p_2 \cdot q)}, \quad W_{12} = \frac{p_1 \cdot p_2}{(p_1 \cdot q)(p_2 \cdot q)} \quad (3.4.5)$$

The products of the colour charge matrices which we encountered in (3.4.4) depend on the specific colour charge configuration of the particles in the process. Their values are just constant coefficients for the functions W_{1i} , W_{2i} and W_{12} which carry the information on the singularity structure and general momenta dependence of the emission probability.

Let us now study closer the function W_{1i} . This function is singular when the 4-momentum q is collinear with p_{in} and p_{1f} . Let us rewrite it as

$$W_{1I} = \frac{1}{E_q^2} \frac{\xi_{1I}}{\xi_{Iq} \xi_{1q}} \quad (3.4.6)$$

where ξ_{kl} is given by

$$\xi_{kl} = \frac{p_k \cdot p_l}{E_k E_l} = 1 - \cos \theta_{kl}. \quad (3.4.7)$$

The energy of parton k is called E_k . We can split W_{1i} into 2 parts singular only in one point separately

$$W_{1I} = W_{1I}^1 + W_{1I}^I \quad (3.4.8)$$

using the expressions for W_{1I}^1 , singular when $\theta_{Iq} \rightarrow 0$, and W_{1I}^I , singular when $\theta_{1q} \rightarrow 0$, in terms of ξ_{kl}

$$W_{1I}^1 = \frac{1}{2E_q^2 \xi_{1q}} \left(1 + \frac{\xi_{1I} - \xi_{1q}}{\xi_{Iq}} \right), \quad W_{1I}^I = \frac{1}{2E_q^2 \xi_{Iq}} \left(1 + \frac{\xi_{1I} - \xi_{Iq}}{\xi_{1q}} \right). \quad (3.4.9)$$

When $\theta_{1q} < \theta_{1I}$ the function W_{1I}^1 is positive and can be interpreted as probability for an emission. In the wave language one can say that the emitted soft gluon interferes with the dipole constructively. Outside of this region W_{1I}^1 oscillates and integrated over the azimuthal angle φ around the momentum of I gives

$$\int_{\pi}^{\pi} \frac{d\varphi}{2\pi} W_{1I}^1 = \frac{1}{E_q^2 \xi_{Iq}} \Theta(\theta_{1I} - \theta_{1q}) \quad (3.4.10)$$

Since W_{1I}^1 can be interpreted as a probability only inside the region $\theta_{1q} < \theta_{1I}$ we can use the fact that the average of it outside of this region is 0 and define

$$\tilde{W}_{1I}^I = W_{1I}^I \Theta(\theta_{1I} - \theta_{1q}), \quad (3.4.11)$$

and replace \tilde{W}_{1I}^I which can be used in a calculation without deviating too much from the exact value if the correct function W_{1I}^I would be used. The term \tilde{W}_{1I}^1 can be identified with emission from parton 1. As we can see one can say that for angles $\theta_{1q} > \theta_{1I}$ only terms \tilde{W}_{1I}^1 , \tilde{W}_{2I}^2 and \tilde{W}_{12} , which can be associated with emissions from partons 1 and 2, contribute significantly and explain the picture in Fig. 3.4.1. The factorisation mechanism discussed here can be generalised for any number of external legs of the diagram. Additional care must be taken when the extra parton is emitted from an inner virtual line. It can be shown that contribution from such emissions is sub-leading [25]. We will assume that such factorisation holds. We will consider only emissions from the parton I and assume that contributions from emissions from parton 1, 2 and all the final state partons are treated in another way for example by final state radiation algorithm. The dominant contribution from additional emissions will be in a phase space region in which

$$\theta_{j,I} > \theta_{j+1,I} \quad (3.4.12)$$

where $\theta_{j,I}$ is angle between the j -th emitted parton and the mother parton I . We will express the angles $\theta_{j,I}$ and $\theta_{j+1,I}$ in terms of components of 4-momenta of the emitting and emitted partons. First we will write the expressions for 4-momenta q_j and q_{j+1} (see figure 3.4.2)

$$q_j = z_{j+1}(1 - z_j)p + \frac{\mathbf{q}_j^2}{2(p \cdot n)(1 - z_j)z_{j+1}} n + q_{j\perp}, \quad (3.4.13)$$

$$q_{j+1} = (1 - z_{j+1})p + \frac{\mathbf{q}_{j+1}^2}{2(p \cdot n)(1 - z_{j+1})} n + q_{j+1\perp},$$

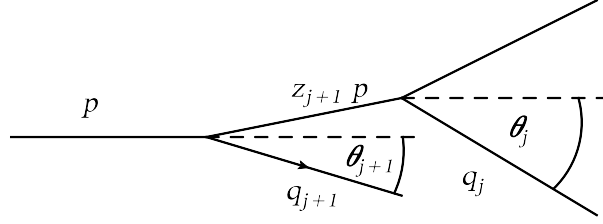


Figure 3.4.2: On derivation of the formula (3.4.18).

where n is an auxiliary 4-vector which satisfies $n^2 = 0$ and $p \cdot n > 0$. We will choose n in such way that $2p \cdot n = s$ the total collision energy squared. The result does not depend on the specific choice of n . Cosines of angles $\theta_{j,I}$ and $\theta_{j+1,I}$ can be expressed as

$$\cos \theta_{i,I} = 1 - \frac{p \cdot q_i}{E_p E_{q_i}}, \quad (3.4.14)$$

where $E_p = \sqrt{s}/2$ and E_{q_i} are the energies of particles p and q_i . Energies E_{q_i} for $i = j$ and $i = j + 1$ can be expressed as

$$\begin{aligned} E_{q_j} &= \frac{\sqrt{s}}{2} \left(1 - z_{j+1}(1 - z_j) + \frac{\mathbf{q}_j^2}{z_{j+1}(1 - z_j)s} \right), \\ E_{q_{j+1}} &= \frac{\sqrt{s}}{2} \left(1 - z_{j+1} + \frac{\mathbf{q}_{j+1}^2}{(1 - z_{j+1})s} \right). \end{aligned} \quad (3.4.15)$$

For small angles θ_i the ratios \mathbf{q}_i^2/s can be neglected and $\cos \theta_i = 1 - \theta_i^2/2$. Inserting equations (3.4.13) and (3.4.15) into (3.4.14) and using the small angle approximations we get

$$\theta_{j,I} \simeq \frac{2|\mathbf{q}_j|}{z_{j+1}(1 - z_j)s}, \quad (3.4.16)$$

$$\theta_{j+1,I} \simeq \frac{2|\mathbf{q}_{j+1}|}{(1 - z_{j+1})s}, \quad (3.4.17)$$

which translates the ordering condition (3.4.12) into

$$\frac{z_{i+1}|\mathbf{q}_{i+1}|}{1 - z_{i+1}} < \frac{|\mathbf{q}_i|}{1 - z_i}. \quad (3.4.18)$$

where \mathbf{q}_i is the transversal momentum of the i -th emitted parton and z_i is the mother parton momentum fraction carried by the i -th emitted parton. The ordering condition as it is described in equation (3.4.18) is implemented in the Monte Carlo generator CASCADE. The ordering condition (3.4.18) for small momentum fractions of emitted partons z_i and z_{i+1} changes to

$$|\mathbf{q}_i| > z_{i+1}|\mathbf{q}_{i+1}|. \quad (3.4.19)$$

and by realising for $z_{i+1} \rightarrow 0$ the \mathbf{q}_i are not ordered which is the situation in BFKL equation in which there is no ordering of transverse momenta of the emitted partons in the ladder. We see that angular ordering offers possibility to exploit the small- x dynamics of BFKL equation and large- x dynamics of the DGLAP equation.

3.4.2 Virtual corrections in the CCFM equation.

We will further work only with gluons. The reasons are that at small- x , when the proton momentum fraction of the initial state parton in the hard sub-process is small, the mother momentum fractions of all the emitted partons z_i are also small because $x = \prod_{i=0}^n z_i$. The splitting functions which include a $1/z_i$ pole are those in which the recoiled particle is a gluon. The splitting function $P_{gg}(z)$ is:

$$P_{gg}(z) = 2N_C \left[\frac{1}{z} + \frac{1}{(1-z)_+} - 2 + z(1-z) + \left(\frac{11}{12} - \frac{n_f}{18} \right) \delta(1-z) \right]. \quad (3.4.20)$$

It is important to point out that in the small z limit ($z \rightarrow 0$) the first term in the bracket in the equation (3.4.20) dominates, other terms are sub-leading, and in the large z limit ($z \rightarrow 1$) the second and the fifth term in the bracket dominates. We will concentrate on these two terms leaving the finite terms for later discussion.

The probability density for a splitting of a gluon into two gluons with angular ordering constraint will be (without inclusion of small- x virtual corrections)

$$d\mathcal{P}_i^\theta = \frac{\alpha_S}{2\pi} dz_i \frac{d^2 \mathbf{q}'_i}{\mathbf{q}'_i{}^2} \hat{P}_{gg}(z_i) \Theta(|\mathbf{q}'_i| > z_{i-1} |\mathbf{q}'_{i-1}|) \Theta(1 - z_i - \epsilon) \quad (3.4.21)$$

with the first Θ -function forcing angular ordering and the second introducing an infrared regulator ϵ , which can be shown has to be $\epsilon = \frac{Q_0}{|\mathbf{q}'_i|}$ [16]. We have also introduced $\mathbf{q}'_i = \mathbf{q}_i/(1-z_i)$ the transverse momentum of the emitted parton rescaled by factor $1/(1-z_i)$. By $\hat{P}_{gg}(z)$ we denote the gluon to gluon splitting function devoid of its non-singular terms.

We can of course split the probability $d\mathcal{P}_i^\theta$ into a part important for $z_i \rightarrow 1$ which will correspond to usual DGLAP equation and into a part important for $z_i \rightarrow 0$ which will be outside of the approximation considered by DGLAP and will correspond to BFKL equation. We can recall the sections 3.1 and 3.3 where virtual corrections in corresponding approximations and summing relevant logarithmic terms were calculated in a form of Sudakov form factor and Regge factor. Similar corrections have to be included also into the splitting function used in the CCFM equation. The difference between already introduced virtual correction factors is that to be consistent one should apply the angular ordering condition (3.4.18) also for the virtual corrections included in them.

The Sudakov form factor will read (see equation (3.1.4))

$$\Delta_S(\mathbf{q}'_i{}^2, (z_{i-1} \mathbf{q}'_{i-1})^2) = \exp \left(- \int_{(z_{i-1} \mathbf{q}'_{i-1})^2}^{\mathbf{q}'_i{}^2} \frac{d^2 \mathbf{q}'}{\mathbf{q}'^2} \int_0^{1-\frac{Q_0}{|\mathbf{q}'|}} dz \frac{\alpha_S}{\pi} \frac{N_C}{1-z} \right). \quad (3.4.22)$$

The Non-Sudakov form factor is

$$\Delta_{NS}(\mathbf{k}_i^2, (z_{i-1}\mathbf{q}'_{i-1})^2) = \exp\left(-\int_{(z_{i-1}\mathbf{q}'_{i-1})^2}^{\mathbf{k}_i^2} \frac{d\mathbf{q}^2}{\mathbf{q}^2} \int_{z_i}^1 dz \frac{\alpha_S}{\pi} \frac{N_C}{z}\right) \quad (3.4.23)$$

in analogy to Regge form factor used in the BFKL equation (3.3.13) respectively. The CCFM equation reads

$$\begin{aligned} \mathcal{F}(x, \mathbf{k}, \mathbf{q}'^2) = & \mathcal{F}(x, \mathbf{k}, \mathbf{q}_0'^2) + \int_{\mathbf{q}_0'^2}^{\mathbf{q}'^2} \frac{d^2\bar{\mathbf{q}}'}{\bar{\mathbf{q}}'^2} \frac{N_C \alpha_S}{\pi} \\ & \int_x^{1-\frac{Q_0}{|\mathbf{q}'|}} \frac{dz}{z} \mathcal{F}(x/z, \mathbf{k}', \bar{\mathbf{q}}'^2) \left(\frac{\Delta_{NS}(\mathbf{k}'^2, (z\bar{\mathbf{q}}')^2)}{z} + \frac{1}{1-z} \right) \Delta_S(\mathbf{q}'^2, (z\bar{\mathbf{q}}')^2), \end{aligned} \quad (3.4.24)$$

where $\mathbf{k}' = \mathbf{k} + \mathbf{q}$. The CCFM equation is very similar to the BFKL equation (3.3.21). However there are some obvious differences. The CCFM equation includes in addition to the term singular for $z \rightarrow 0$, a term singular for $z \rightarrow 1$. Virtual corrections regulating this singularity have to be included by multiplying the splitting function by the Sudakov form factor. Another difference comes from the angular ordering in the form presented above. This means that the unintegrated parton density function $\mathcal{F}(x, \mathbf{k}, \mathbf{q}'^2)$ is in not only function of the transverse momentum of the virtual parton \mathbf{k} , but also a function of the ordering scale \mathbf{q}'^2 . The presence of the term responsible for soft gluon emissions in the CCFM splitting function provides summation of logarithms of $\mathbf{q}'^2/\mathbf{q}_0'^2$ in addition to the $1/x$ logarithms summed by the BFKL equation in leading logarithmic precision.

3.5 uPDF evolution equations summary

In the section 5.2 we mentioned approaches of getting uPDFs based on solutions of the CCFM equation and BFKL equation. Since uPDFs carry information about the transversal momentum of the partons one can expect that by interpreting the kernels of the CCFM and the BFKL equations in a probabilistic sense and solving them by parton shower approaches should not lead to a different results than by solving them using a different numerical or analytical approach. The uPDFs calculated in both ways should be in principle identical. However, the probabilistic interpretation of the parton evolution is in a strict sense only possible for the CCFM equation. In the derivation of the BFKL equation in leading order, for real and virtual corrections, 4-momentum conservation is violated. It is taken into account in the CCFM equation. The consistency of uPDFs obtained by the parton shower algorithm and uPDFs obtained by solving the inclusive CCFM equation was demonstrated in [26]. The efforts to obtain uPDFs using available data from HERA experiments are represented by [27–29] and more recent [30].

Chapter 4

Monte Carlo generators PYTHIA, HERWIG and CASCADE

In this section we will describe some of the characteristics of Monte Carlo generators which were used to calculate results in this thesis.

4.1 PYTHIA

Monte Carlo generator PYTHIA [8] is a general purpose Monte Carlo generator with around 500 hard subprocesses available. The initial final state and initial state parton showers are based on the DGLAP equation [7]. There are several different options for the ordering of initial state parton showers including k_{\perp} -ordering – ordering in transverse momentum of the propagator parton, q^2 -ordering – ordering in virtuality of the propagator parton and p_{\perp} -ordering – ordering in transverse momentum of the emitted parton. The final state parton showers are ordered in angle. The hadronisation model, is the Lund string model [31].

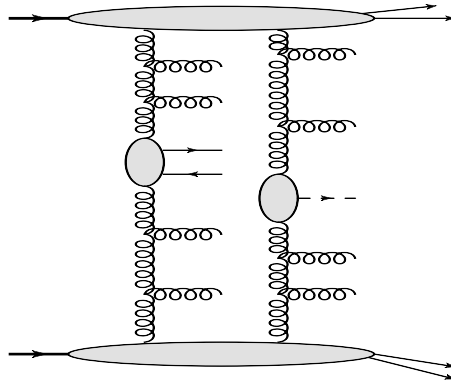


Figure 4.1.1: Schematic picture of MPI with two hard scattering subprocesses.

PYTHIA offers also experimentally well tested [32] models for multi parton interactions. The arguments for phenomenological relevance of MPI are based on simple assumptions [33]. More sophisticated models of MPI are described in [34]. We will describe here a simple argumentation on which some of the MPI models are based. As we already explained in the section 3.2.1 the $2 \rightarrow 2$ subprocesses diverge to infinity with transversal momentum \mathbf{p} of the final state particles $\mathbf{p} \rightarrow 0$. This strong rise of the partonic cross section σ_p causes that its value for certain value of $\mathbf{p} = \mathbf{p}_c$ becomes larger than the total cross section of pp or ep scattering $\sigma_p(\mathbf{p}_c) > \sigma_{tot}$. To solve this problem one can interpret the ratio $\sigma_p(\mathbf{p})/\sigma_{tot}$ as the average number of multiple parton interactions in one pp collision with certain \mathbf{p} . Another parton shower chain with a different hard subprocess can be generated with probability $(d\sigma/d\mathbf{p}^2)/\sigma_{tot}(s)$, figure 4.1.1, where

$$\frac{d\sigma}{d\mathbf{p}^2} = \sum_{i,j,k} \int_0^1 dx_1 \int_0^1 dx_2 \int dt f_i(x_1, Q^2) f_j(x_2, Q^2) \frac{d\hat{\sigma}_{ij}^k}{dt} \delta\left(\mathbf{p}^2 - \frac{\hat{t}\hat{u}}{\hat{s}}\right), \quad (4.1.1)$$

and \hat{t} , \hat{u} and \hat{s} are the Mandelstam variables. Partonic cross section is denoted by σ_{ij}^k and PDFs by f_i and f_j .

In the simplest models it is assumed that the probability of subcollisions are not correlated which leads to Poisson distribution of the number of MPI. Additional chains will not change the total cross section, but will change observables like jet multiplicity, transversal momentum spectra and correlations between jets because the parton emissions in the two parton shower chains are kinematically independent.

4.2 CASCADE

The Monte Carlo generator CASCADE [26] is able to simulate $e^\pm p$ and $pp(\bar{p})$ processes. In CASCADE the initial state parton showers are based on CCFM evolution equation with angular ordering as described in section 3.4.1 (section 3.4). The CCFM equation generates uPDFs so the partons entering the hard subprocess are off-shell. The off-shellness of the initial state partons in the hard subprocess is taken into account not only in the kinematics, but also in the hard matrix element of the subprocess. Processes like heavy quark-antiquark pair production in $e^\pm p$ and $pp(\bar{p})$, the higgs production are included. The final state parton showers are generated using PYTHIA. Final state parton showers are applied only on coloured particles from the hard subprocess. The hadronisation of the partons produced in parton showers is done using Lund string hadronisation model as implemented in PYTHIA.

The implementation of the CCFM equation is very much analogous to the implementation of the DGLAP equation described in section 3.1. There are some peculiarities with the appearance of two scales for α_S in the CCFM gluon splitting function and with kinematics in the backward evolution parton shower algorithm which were overcome by authors of [26].

The second problem is the gluon virtuality. The virtuality of the gluon entering the hard scattering subprocess can be reconstructed only after the whole chain of branchings has been generated. There is a kinematical reconstruction implemented in Monte Carlo

generator CASCADE to acquire the correct virtuality of the gluon entering the hard subprocess. The reconstruction starts from the gluon which is the closest to the proton (the last one generated in backward evolution) with virtuality

$$k_0^2 = \frac{\mathbf{k}_0^2}{1 - x_0} \quad (4.2.1)$$

The new virtuality of the gluon entering the hard subprocess is typically larger than it was before the reconstruction. A check is applied if the kinematics allows for production of particles in the hard subprocess.

It can be easily shown that the correct virtuality of the gluon entering the hard matrix element is

$$k^2 = \frac{\mathbf{k}^2}{1 - x} \left(1 + x \frac{m_{rem}^2}{\mathbf{k}^2} \right), \quad (4.2.2)$$

where m_{rem} is the invariant mass of all the partons produced except of the hard subprocess.

4.3 HERWIG and HERWIG++

HERWIG and HERWIG++ are general purpose Monte Carlo generators. Initial and final state parton showers in both Monte Carlo generators HERWIG and HERWIG++ [9] are based on the DGLAP equation. They adopt angular ordering of the emissions by defining a scale Q_i [16] by equation

$$Q_i = E_i \sqrt{\xi_i}, \quad (4.3.1)$$

where E_i is the energy of the i -th propagator parton. The variable ξ_i is defined using momentum of the parton which initiates the shower p and the momentum of the i -th emitted parton q_i

$$\xi_i = \frac{p \cdot q_i}{E_p E_{q_i}} = 1 - \cos \theta_{pi}, \quad (4.3.2)$$

with E_p and E_{q_i} being the energies of the partons. The angle θ_{pi} is then between the spacial components of 4-momenta of p and q_i . The ordering is defined by equation

$$Q_{i+1} < Q_i. \quad (4.3.3)$$

This ordering reduces to [16]

$$E_{i+1} \theta_{pi+1} < E_i \theta_{pi} \quad (4.3.4)$$

in the small angle limit. By rewriting it in way which was done for the equation (3.4.18) we get

$$\frac{|\mathbf{q}_{i+1}|}{1 - z_{i+1}} < \frac{|\mathbf{q}_i|}{1 - z_i}, \quad (4.3.5)$$

which is the correct angular ordering in the limit $z \rightarrow 1$, but leads to ordering of transversal momenta for $z \rightarrow 0$.

In HERWIG++ for initial state parton shower the evolution variable \tilde{q}^2 is defined by relation [9]

$$(1 - z)\tilde{q}^2 = -zm_k^2 + m_i^2 + \frac{zm_j^2}{1 - z} - \frac{\mathbf{p}^2}{1 - z}, \quad (4.3.6)$$

where z is the momentum fraction carried by the propagator parton j . Massive partons with masses m_i , m_j and m_k are assumed in the formula (4.3.6). The relative transversal momentum \mathbf{p} is defined as $\mathbf{p} = \mathbf{q}_i - z\mathbf{q}_k$. The formula (4.3.6) is a generalisation of the one in (4.3.1). The ordering for small angles reduces to (4.3.4) [9].

The ordering for the final state parton showers is defined in an analogous way [9].

The fragmentation in Herwig++ is modelled by implementation of the cluster fragmentation model.

Herwig++ offers also model of MPI described in [35].

Chapter 5

The transverse momentum of the Z -boson

For the same reasons we explained in the section 3.2 the naive application of the parton model to Z -boson production will result in a wrong result of the transversal momentum of the Z -boson $p_{Z\perp} = 0$. The $\mathcal{O}(\alpha_S)$ contribution in fixed order perturbation gives a reasonable spectrum for large $p_{Z\perp}$, but fails for small $p_{Z\perp}$. There is a good motivation to go beyond fixed order perturbation theory and resum the whole series of potentially dominant terms. We will discuss different approaches to the resummation in next subsections.

5.1 Analytical approaches

Part of the efforts to calculate the transverse momentum of the Z -boson concentrate on the cross section of the Z -boson production in hadron-hadron scattering as a function of $p_{Z\perp}$ and do not address other possible observables. In these approaches one analytically resums parton emissions by exponentiation of factorised cross sections or by solving the renormalisation group equation for parton emission corrections.

The resummation of logarithmic terms of the form $\alpha_S^n [\ln(\mu^2/\mathbf{q}^2)]^{2n-1}$, where μ is the hard scale of the process and \mathbf{q} is the transversal momentum generated by the emissions of partons, so called double-logarithmic approximation, for Z boson transversal momentum distribution has been done in end of 90's by authors of [36]. The authors found that leading contribution to the cross section in physical gauge is generated by dressed ladder diagrams. Every power of α_S is accompanied by a second power of $[\ln(\mu^2/\mathbf{q}^2)]^n$ in which one of the logarithms comes from the collinear singularity and the other originates from the soft singularity of the emitted parton. The resummation has been done in the transversal momentum space ensuring the factorisation of the parton emission and the phase space by strong ordering of the transversal momenta of the emitted partons - $\mathbf{q}_i^2 \gg \mathbf{q}_{(i+1)}^2$. By such a condition the delta function in the phase space which guaranties the transversal momentum conservation $\delta\left(\sum_{i=1}^n \mathbf{q}_i + \mathbf{q}\right)$ reduces to $\delta(\mathbf{q}_n + \mathbf{q})$ and phase space can be factorised and parton emissions can be resummed by exponentiation.

The authors of [37,38] have shown that one can resum also subleading terms of the form $\alpha_S^n [\ln(\mu^2/\mathbf{q}^2)]^{2n-m}$, where $m = 1, \dots, 4$ when one relaxes the strong transversal momenta ordering condition, but keeps the transversal momenta ordered. To be able to factorise the phase space one performs a Fourier transform to \mathbf{b} space where the transversal momentum conservation delta function factorises

$$\int \frac{d^2\mathbf{q}}{(2\pi)^2} \delta\left(\sum_{i=1}^n \mathbf{q}_i + \mathbf{q}\right) e^{i\mathbf{b}\cdot\mathbf{q}} = e^{-i\mathbf{b}\cdot\left(\sum_{i=1}^n \mathbf{q}_i\right)} = \prod_{i=1}^n e^{-i\mathbf{b}\cdot\mathbf{q}_i}. \quad (5.1.1)$$

One can then perform the resummation in the \mathbf{b} space and return to \mathbf{q} space by an inverse Fourier transform.

In the formalism described in [37,38] the cross section can be written in a compact form

$$\begin{aligned} \frac{d\sigma}{dQ^2 dy d\mathbf{q}^2} &\sim \frac{4\pi^2\alpha^2}{9Q^2s} (2\pi)^{-2} \int d^2\mathbf{b} e^{i\mathbf{q}\cdot\mathbf{b}} \sum_j e_j^2 \\ &\times \sum_a \int_{x_1}^1 \frac{d\xi_1}{\xi_1} f_{a/1}(\xi_1, 1/|\mathbf{b}|) \times \sum_b \int_{x_2}^1 \frac{d\xi_2}{\xi_2} f_{b/2}(\xi_2, 1/|\mathbf{b}|) \\ &\times \exp\left\{-\int_{1/|\mathbf{b}^2}^{Q^2} \frac{d\bar{\mu}^2}{\bar{\mu}^2} \left[\ln\left(\frac{Q^2}{\bar{\mu}^2}\right) A(\alpha_S(\bar{\mu})) + B(\alpha_S(\bar{\mu}))\right]\right\} \\ &\times \mathcal{C}_{ja}\left(\frac{x_1}{\xi_1}, \alpha_S(1/|\mathbf{b}|)\right) \mathcal{C}_{\bar{j}b}\left(\frac{x_2}{\xi_2}, \alpha_S(1/|\mathbf{b}|)\right) \\ &+ Y(\mathbf{q}, Q, x_1, x_2). \end{aligned} \quad (5.1.2)$$

In equation (5.1.2) Q^2 is the hard scale of the process, s is the proton-proton collision energy squared, e_j are the charges of the annihilating quark and antiquark, x_1 and x_2 are the momentum fractions of the initial state partons which can differ from the quark-antiquark pair in higher orders of the perturbation theory. The indices a and b run over parton species. The cross section is a Fourier transform of a convolution of PDFs $f_{a/1}$ and $f_{b/2}$, the Sudakov form factor is represented by an exponential of an integral of perturbatively calculable functions A and B and coefficient functions \mathcal{C} which characterise the transition from partons a and b in the initial state to annihilating quark-antiquark pair $j\bar{j}$ and the Y term. The factors included in the convolution integral (the first term) include pieces of the hard subprocess which are singular for $\mathbf{q}^2 \rightarrow 0$. This part of the cross section dominates in the region where $\mathbf{q}^2 \ll Q^2$, but is valid also for $\mathbf{q}^2 \leq Q^2$. The term Y includes the finite and at most singular as \mathbf{q}^{-2} for $\mathbf{q}^2 \rightarrow 0$ pieces of the cross section.

The authors of [37,38] were able to calculate the functions A , B , \mathcal{C} and Y . The steps which have to be done to calculate these functions in any order of the perturbation theory are well defined.

The resummation method fails when $\mathbf{q} \gg \mu^2$ roughly around the electroweak gauge boson mass $m_Z^2 \sim \mu^2$ since the method is not valid for too large \mathbf{q}^2 . Since the fixed

order calculation works for large \mathbf{q}^2 one can interpolate between these two regimes and obtain the full differential cross section. The authors of [39] pointed out that the cross section calculated in the \mathbf{b} space is unstable in the region of interpolation and performed a resummation in \mathbf{q} space which stabilises the cross section and allows for easier interpolation with the fixed order cross section.

The authors of [40] argue that simultaneous resummation of the logarithms of $1/x$ in addition to logarithms of μ^2/\mathbf{q}^2 might be important for the shape of the gauge bosons transversal momentum differential cross section. They find that these additional terms lead to a broadening of the turnover peak of the distribution.

In [41] the authors resummed simultaneously logarithmic terms of $1/x$ and μ^2/\mathbf{q}^2 by solving analytically the CCFM equation [25] in \mathbf{b} space and obtaining uPDFs which were calculated in [42]. The formula for the cross section described in [41] is formally identical to the standard resummation formula introduced in [37]. The authors also studied different non-perturbative factors which affect the spectrum of the transversal momentum of electroweak boson.

The electroweak boson production can be considered as one of the main contributions to the Higgs boson production background. The authors of [43] considered electroweak boson production and $b\bar{b}$ production from two independent parton evolution chains. For this purpose they calculated W production from a single evolution chain by solving the leading order BFKL equation and convoluting the resulting uPDFs with the dominant contribution diagrams, with t -channel quark exchanges, of the subprocess $g^*g^* \rightarrow Wq_i\bar{q}_j$, with g^* being off-shell gluon and i and j labelling the flavours of the quarks.

5.2 Semi-analytical approaches

Another approach to resummation of enhanced logarithmic terms and keeping track of the transverse momentum of the parton emissions is based on formulating the evolution equations for PDFs or transverse momentum dependent PDFs also called unintegrated PDFs - uPDFs and their numerical solving. Semi-analytical methods allow for calculation of a wider range of observables. The special class of methods to solve the evolution equation is based on Monte Carlo generators and was shortly described in separate subsection.

Although there was some development in the direction of quark uPDFs [44], the formalism in which the CCFM equation was derived is most consistent for purely gluon evolution chains. That is why the authors of [45] consider a hard subprocess $g^*g^* \rightarrow Z/W^\pm/\gamma q_i\bar{q}_j$ in pp scattering which allows for gauge boson production with gluons in initial state. However, also the channels $g^*q_i \rightarrow Z/W^\pm/\gamma q_j$ and $\bar{q}_i q_j \rightarrow Z/W^\pm/\gamma$ were considered. The cross section for $Z/W^\pm/\gamma$ production was obtained by convolution of the hard off-shell matrix element with uPDFs calculated numerically by solving the CCFM equation in \mathbf{k} space by a Monte Carlo method, with \mathbf{k} being the transversal momentum of the initial state gluon and by uPDFs generated by the KMR [46] method in which the PDFs are evolved by the DGLAP equation and only in the last splitting, the one closest to the hard subprocess, is left unintegrated and in fact generates the transversal momentum of the initial state

parton. The authors of [46] define an uPDF of parton species a using a partial derivative of the integrated PDF according to the logarithm of the scale squared $\ln \mu^2$:

$$\mathcal{A}_a(x, \mathbf{k}^2) = \left. \frac{\partial f_a(x, \mu^2)}{\partial \ln \mu^2} \right|_{\mu^2=\mathbf{k}^2} = \frac{\alpha_S(\mathbf{k}^2)}{2\pi} \sum_{a'} \int_x^{1-\Delta} dz P_{aa'} f_{a'}\left(\frac{x}{z}, \mathbf{k}^2\right). \quad (5.2.1)$$

The most right side of the equation (5.2.1) follows after applying the DGLAP equation. Since the virtual contribution does not change the \mathbf{k} it can be resummed to give the no-emission probability in a form of a Sudakov form factor

$$T_a(\mathbf{k}, \mu) = \exp\left(-\int_{\mathbf{k}^2}^{\mu^2} \frac{d\mathbf{k}'^2}{\mathbf{k}'^2} \frac{\alpha_S(\mathbf{k}'^2)}{2\pi} \sum_{a'} \int_0^{1-\Delta} dz' P_{a'a}(z')\right) \quad (5.2.2)$$

The probability to find a parton a with transversal momentum \mathbf{k} which initiates the hard subprocess at the scale μ is

$$\mathcal{A}_a(x, \mathbf{k}^2, \mu^2) = \left. \frac{\partial f_a(x, \mu^2)}{\partial \ln \mu^2} \right|_{\mu^2=\mathbf{k}^2} = T_a(\mathbf{k}, \mu) \frac{\alpha_S(\mathbf{k}^2)}{2\pi} \sum_{a'} \int_x^{1-\Delta} dz P_{aa'} f_{a'}\left(\frac{x}{z}, \mathbf{k}^2\right). \quad (5.2.3)$$

The uPDF $\mathcal{A}_a(x, \mathbf{k}^2, \mu^2)$ becomes a function of two scales only in the last step of the evolution when the transversal momentum of the parton which initiates the hard subprocess is generated. Before this step the transversal momentum in the evolution remains untouched. The proper choice of the cut-off parameter $\Delta = |\mathbf{k}|/(|\mathbf{k}| + \mu)$ appearing in equations (5.2.1), (5.2.2) and (5.2.3) to regularise the integrals over the momentum fraction z was in [46] chosen to acquire for angular ordering of the gluon emissions¹. It follows from the relation $\mu > z|\mathbf{k}|/(1-z)$. The authors of [46] further discuss also inclusion of $\ln 1/x$ corrections.

For the initial state quarks only valence quarks were considered using standard PDFs. In the process of calculating the cross section one integrates over the phase space of quark and antiquark in the final state of $g^*g^* \rightarrow Z/W^\pm/\gamma q_i \bar{q}_j$ and $g^*q_i \rightarrow Z/W^\pm/\gamma q_j$. The collinear and soft singularities connected with emission of these quarks were regulated by considering massive quarks.

The same authors as in the previous paragraph discussed in [47] also the sea-quark contribution to the production cross section of electroweak gauge boson. In this work they considered also the subprocesses $g^*q \rightarrow \gamma q$, $q\bar{q} \rightarrow \gamma g$ and $q_i \bar{q}_j \rightarrow Z/W^*$ with sea-quarks in the initial state. The uPDFs for the sea-quarks being produced according to the KMR framework. Only the last splitting $g \rightarrow q\bar{q}$ produces the unintegrated sea-quark distribution.

In the publication [48] we studied the process $g^*g^* \rightarrow Z/W^\pm q_i \bar{q}_j$ with the motivation to describe hard subprocess electroweak boson production with off-shell gluons in the initial

¹Importance of angular ordering for gluon emissions is explained in section 3.4.

state by convoluting it with CCFM uPDFs. We also studied Z/W^\pm production associated with heavy quark-antiquark pair. The calculation and discussion of phenomenological results will be described in section 6.

Chapter 6

Drell-Yan production in heavy quark-antiquark annihilation

In this section we will focus on the Drell-Yan production of electro-weak gauge bosons - Z , W and γ - by emphasising the heavy quark-antiquark annihilation - $Q\bar{Q} \rightarrow Z/W/\gamma$ - channel in proton-proton collisions. Consideration of heavy quarks in the initial state naturally leads to appearance of heavy quarks in the final state. We can show it easily by considering backward evolution of such a heavy quark. To evolve it backwards it had to radiate gluon or a heavy quark. In latter case the radiated heavy quark will be the one appearing in the final state. Heavy quark radiation has to happen at some scale because by evolving the heavy quark backwards by gluon emissions the scale will decrease close to the heavy quark mass m_Q . At such a point the m_Q will be the natural hard scale. To get lower in scale one then needs, because of momentum conservation, to radiate the heavy quark. The non-perturbative scale is at the order of the proton mass $m_p < m_Q$ as we consider quarks heavier than the proton to be heavy. That is why we do not expect to find a heavy quark inside a proton at the scale of the proton mass. From an experimental point of view to be able to say if the gauge boson was produced in a heavy quark-antiquark annihilation one needs to have an identified $Q\bar{Q}$ pair. For reasons listed above one should rather talk about electro-weak gauge boson production in association with heavy quark-antiquark pair - $pp \rightarrow Q_i\bar{Q}_j Z/W/\gamma + X$.

We will describe two approaches to the calculation of this process and discuss them in more detail in next subsections. However let us first discuss the importance of this process in context of LHC physics.

The most important extensions of the Standard Model (SM) of particle physics which will be looked for at LHC are its supersymmetric (SUSY) extensions. SUSY models predict at least a fermion partner for each boson from the SM and a boson partner for each fermion from the SM. In addition SUSY SM extensions predict at least four Higgs particles and their fermionic superpartners. These *superpartners* of SM particles were not yet discovered so they have to be heavy enough to be not produced at colliders except the LHC. This implies that supersymmetry is broken since exact supersymmetry predicts the *superpartners* to have equal masses [49]. Final states in pp collisions predicted by SUSY models consist

of multi-jets and missing mass - undetected energy - which is a consequence of the large masses (multi-jets) of the supersymmetric particles and the so called R-parity which forces the conservation of the number of superparticles and leads to a stable lightest superparticle. R-parity is not required by the most general SUSY lagrangian [49]. Since the gauge boson W can decay into a lepton l and an undetected neutrino ν_l the process $pp \rightarrow Q_i \bar{Q}_j Z/W/\gamma$ can mimic such final states. In case when the heavy quark-antiquark pair consists of b -quarks the missing energy can originate from a decay $b \rightarrow cW \rightarrow cl\nu_l$.

The process $pp \rightarrow Q_i \bar{Q}_j Z/W/\gamma + X$ is also background to SM Higgs production. Especially for the process called Higgsstrahlung in which Higgs is produced in association with Z boson by being emitted from it as bremsstrahlung. The Higgs can then decay into a $b\bar{b}$ pair producing exactly the same final state as the process $pp \rightarrow b\bar{b}Z + X$. The Z particle in the latter process is emitted from the b -quark line. By replacing it by Higgs particle and assuming the same decay as for the Z (for example $Z/H \rightarrow \mu^+\mu^-$) we get directly another Higgs production channel for which is this process a background.

6.1 Z and W production associated with heavy quark-antiquark pair in k_\perp -factorisation.

In this section we will discuss the calculation of Z , W and γ bosons production associated with heavy quark-antiquark pair in k_\perp -factorisation in proton-proton collisions at LHC - $pp \rightarrow Q_i \bar{Q}_j + Z/W/\gamma + X$, where indices $i = j$ in case of Z and γ production. We will focus on the hard subprocess in which we expect the final state particles to be produced. One would naively expect initial states of the hard subprocess to consist from these channels:

- $Q_i \bar{Q}_j \rightarrow Q_i \bar{Q}_k + Z/W/\gamma$
- $q_i \bar{Q}_j \rightarrow Q_k \bar{Q}_j + W$
- $gg \rightarrow Q_i \bar{Q}_j + Z/W/\gamma$

We will be working in fixed flavour number scheme so we treat the heavy quarks only perturbatively. The mass of heavy quarks is taken into account in the hard scattering matrix element. We will also drop the contribution of channels with massless quarks in the initial state. Those should be included for phenomenological reasons in a full calculation. There is no reason to leave them out in a collinear calculation since the PDFs for sea and valence quarks are available. The situation in k_\perp -factorisation is more complicated. There are models for sea-quark uPDFs [42, 46] and evolution equation for valence quarks is available. However we can argue that gluon uPDFs are sufficient for phenomenological studies. On such assumption is based also the Monte Carlo generator CASCADE. The main argument on phenomenological sufficiency of gluon uPDFs is based on the gluon uPDF dominance at the LHC energies especially at small- x . To show relevance of the assumption of the gluon dominance in the context of the $gg \rightarrow Z/W/\gamma + Q_i \bar{Q}_j$ production we have to show that the gluons in the hard subprocess for this process at the LHC carry mostly

small proton momentum fraction. A typical scale in the hard subprocess is the Z/W mass $m_{Z/W} \sim 100 \text{ GeV}$. Assuming this we can calculate the typical proton momentum fractions carried by the electroweak gauge boson using simple formula $x \sim \sqrt{\frac{m_{Z/W}^2}{s}} \sim 0.007$ which is a value at which the gluon PDF dominates. In contrast of typical proton momentum fraction at TeVatron, where $x \sim \sqrt{\frac{m_{Z/W}^2}{s}} \sim 0.04$ which does not allow for gluon dominance. Other arguments for pure gluon phenomenology are based on suppression of sea-quark contribution in the BFKL framework. As we know in BFKL the gluon reggeizes. Quark reggeization can be also obtained, but the resulting cross section is suppressed by factor of \sqrt{s}^{-1} . The reggeized quark represents leading contribution to the sea-quark uPDFs in the framework of BFKL equation. However there are studies which looked at the contribution of reggeized quarks and argue for their relevance by showing a good agreement with data [50]. Valence quarks can be neglected in our study because their PDFs, in contrast to sea-quark PDFs growing with decreasing x , are strongly suppressed at small- x . In the case of light sea-quarks the g^*qq vertex generates the sea-quark which annihilates with an anti-quark to produce the electro-weak gauge boson. In this way the last splitting in the evolution which would produce the sea-quark distribution is included in the hard matrix element.

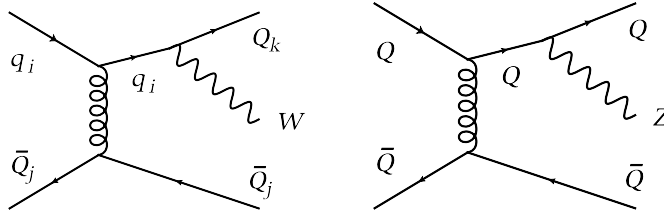


Figure 6.1.1: Diagrams for W and Z production.

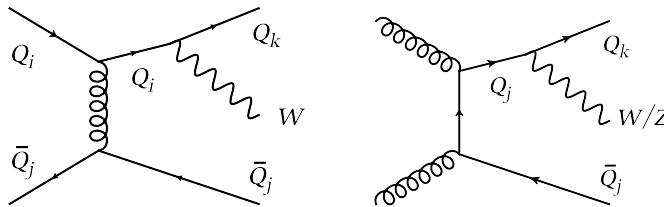


Figure 6.1.2: Diagrams for W and Z production.

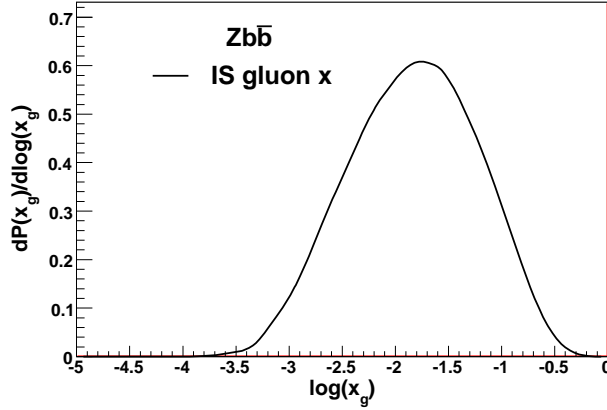


Figure 6.1.3: Probability distribution of x_g in $Z/W + Q\bar{Q}$ in Monte Carlo generator CASCADE.

For the reasons listed above we will describe the calculation of $W/Z/\gamma$ electroweak gauge bosons associated with a pair of heavy quark and antiquark produced with gluons in the initial state in so called gluon-gluon fusion with both gluons off-shell. The arguments from the previous paragraph also apply to electroweak boson production associated with light quarks which would in the framework of having only gluons in the initial state correspond (as done in [45]) to Drell-Yan gauge boson production process.

In next subsections we will describe kinematics of the $2 \rightarrow 3$ subprocess with initial state particles off-shell. Then we will discuss the gauge invariance of the matrix element. Further we will discuss details of the calculation including *method of orthogonal amplitudes*. We will discuss some aspects of the results - how more correct kinematics mimics next to leading order effects and affects the transversal momentum spectra of particles. The calculation was published [48] and is included in the Appendix.

6.1.1 Discussion of the kinematics

We would like to calculate and study production of $W/Z/\gamma + Q\bar{Q}$ at the LHC energy $14 TeV$. This energy region allows particles to be produced in the regime in which $|t| \ll s$ (t is the momentum exchange squared and s the total energy squared of the proton-proton collision), but still keeping $|t| \gg \Lambda_{QCD}$. A consequence is that the initial state particles are allowed to and quite often carry small fractions of the protons 4-momenta. To show that this is also the case for $g^*g^* \rightarrow W/Z/\gamma + Q\bar{Q}$, we can plot the probability distribution of proton momentum fraction x_g carried by the initial state gluon in figure 6.1.3. The distribution peaks at rather small $x_g \sim 10^{-2}$ and extends to lower x_g values.

Formally the calculation in k_\perp -factorisation with off-shell quarks assumes a kinematic regime described above, but is valid also for larger values of the proton momentum fractions carried by initial state gluons.

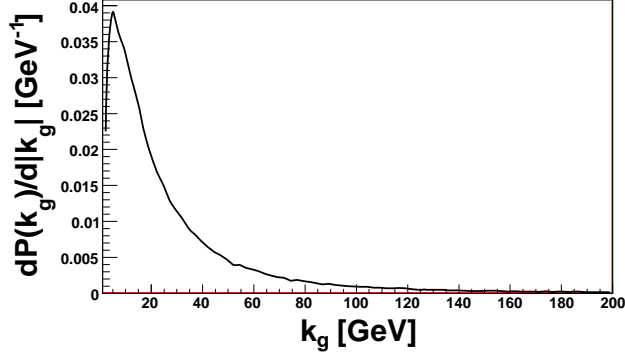


Figure 6.1.4: Probability distribution of k_g in $Z/W + Q\bar{Q}$ in Monte Carlo generator CASCADE.

To illustrate that the transversal momenta of initial state off-shell gluons are significantly large to affect observables connected to transversal momenta of the final state particles we show also the k_g transversal momentum distribution of the initial state gluon in figure 6.1.4. We see that it extends to rather large values.

In the following subsections we will use q_A and q_B to denote the 4-momenta of the initial state protons also assigned to initial state auxiliary quarks. 4-momenta k_1 and k_2 will be the final state quarks 4-momenta.

6.1.2 Discussion of the gauge invariance

The matrix element of the process $g^*g^* \rightarrow Z/W/\gamma + Q_i\bar{Q}_j$ can be calculated in two different ways. A closer look on their relation reveals the nature of the mechanism of gauge invariance of the hard matrix elements calculated in k_{\perp} -factorisation. We will present both ways of calculation and discuss the relation between them in this section.

We will not only discuss the $SU(3)$ gauge invariance of the matrix element, but also study the broken gauge symmetry of the $SU(2)$ which comes into play because of presence of electroweak gauge bosons in the final state.

SU(3) gauge invariance

From the QCD point of view the two calculation methods/ways differ in the choice of diagrams, the set of diagrams which has to be taken into account, and the choice of polarisation densities for the initial and final state gluons. It should be pointed out, to cause no confusion, that ghost diagrams, as we will see, do not appear in any of the calculations. Let us discuss the first method. The arguments which we will use are independent on the choice of the final state particles we are considering so we will call them in the following simply S_f as final state. Of course it does not make sense to consider the process $g^*g^* \rightarrow S_f$ without having in mind that it is only a subprocess of the process $pp \rightarrow S_f + X$ with S_f

created in collision of two off-shell gluons originating from pp collisions. What is nontrivial about this consideration is that we expect the subprocess $g^*g^* \rightarrow S_f$ to factorise from the larger hadronic process. By taking this into account we realise that it should not matter if we consider protons colliding or other particles, because, if factorisation works, it does not change the nature of the subprocess and by that also the hard matrix element. To simplify the calculation we can then consider the process $q_A q_B \rightarrow g^*g^* + q_A q_B \rightarrow S_f + q_A q_B$ (we will label q_A and q_B also the four-momenta of the corresponding quarks). Now we have to calculate the hard matrix element of this process by considering also the kinematics of the process and extract the hard matrix element of the subprocess $g^*g^* \rightarrow S_f$. Of course in the end we should see that it factorises from the larger quark-quark scattering process to validate our assumption about the factorisation of the subprocess and to approve the simplification of the calculation by the replacement of the protons by quarks. By adapting the kinematics from the previous subsection, $|t| \ll s$, we realise that we can neglect the component in the direction of the momentum of q_B of the momentum of gluon coupling to q_A (see the diagrams in Fig. 6.1.2). The vertex of the coupling of the gluon to the quark is then modified to the eikonal vertex as was described in the section 3.3 (see equation (3.3.6)). So, we have the effective polarisation vectors of the gluons

$$\epsilon_A^\mu(q_A) = \frac{2q_A^\mu}{\sqrt{s}}, \quad (6.1.1)$$

$$\epsilon_B^\mu(q_B) = \frac{2q_B^\mu}{\sqrt{s}} \quad (6.1.2)$$

called 'non-sense' polarisations. The factor $1/\sqrt{s}$ ensures that the polarisation vector is dimensionless. The factor 2 is just a matter of definition. The motivation for this name is that these polarisation vectors are not normalized to 1 as usual polarisation vectors, however this does not prevent us to interpret them as polarisation vectors.

We can also reduce the number of diagrams when we modify the three-gluon vertex as we did in the section about the BFKL equation 3.3 in the equation (3.3.6). However after calculating the matrix element and performing the collinear limit by averaging over the polar angles ϕ_A and ϕ_B of the transversal momenta $\mathbf{k}_{A\perp}$ and $\mathbf{k}_{B\perp}$ and taking the limits $k_{A\perp} \rightarrow 0$ and $k_{B\perp} \rightarrow 0$ and comparing with the matrix element calculated with on-shell initial state gluons in the standard way (summing the proper set of diagrams with proper polarisation sums) we discover that results differ by a factor. More precisely

$$\mathcal{M}_{on-shell} = \left[\frac{\alpha^2 \beta^2 s^2}{t_1 t_2} \mathcal{M}_{off-shell}^I \right]_{t_1=0, t_2=0} \quad (6.1.3)$$

where the subscript means the angular averaging and limits $t_1 \rightarrow 0$ and $t_2 \rightarrow 0$. The factor $\frac{\alpha^2 \beta^2 s^2}{t_1 t_2}$ does not depend on the character of the final state S_f - it is universal, and it can be calculated for simpler process and applied to the one of interest.

The interpretation of this fact is that by letting gluons explicitly couple to the quark line we have chosen a certain model of uPDFs for the gluons. If we would calculate the

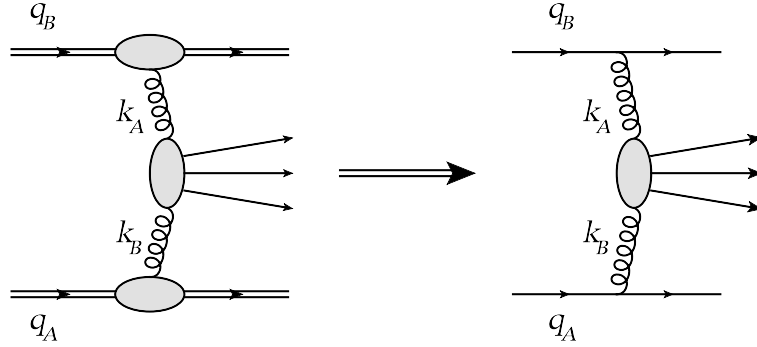


Figure 6.1.5: Replacing protons by quarks.

process $pp \rightarrow S_f$ we would obtain the correct proton uPDFs. We will comment on the origin of the factor later after the description of the second approach to the calculation.

In the second approach there are only 5 diagrams, those used in the case when the initial state gluons are on-shell and physical polarisation sums are used for gluon lines. We are taking the initial state gluons to be off-shell and in this approach we choose their polarisation vectors as

$$\epsilon_A^\mu(k_A) = \frac{k_{A\perp}^\mu}{|\mathbf{k}_{A\perp}|}, \quad (6.1.4)$$

$$\epsilon_B^\mu(k_B) = \frac{k_{B\perp}^\mu}{|\mathbf{k}_{B\perp}|} \quad (6.1.5)$$

These polarisation vectors have the property that they are normalized to 1. Another nice property is that after angular averaging and the on-shell limit we obtain exactly the on-shell result

$$\mathcal{M}_{on-shell} = \left[\mathcal{M}_{off-shell}^H \right]_{t_1=0, t_2=0} \quad (6.1.6)$$

We will describe shortly how one obtains the polarisation vectors (6.1.4). The key point is the observation that

$$p_A^\mu d_{\mu\nu}^{(n)}(k_A) = \frac{k_{A\perp\nu}}{\alpha}, \quad p_B^\mu d_{\mu\nu}^{(n)}(k_B) = \frac{k_{B\perp\nu}}{\beta}. \quad (6.1.7)$$

where $d_{\mu\nu}^{(n)}(k)$ is a gluon polarisation tensor in the axial gauge

$$d_{\mu\nu}^{(n)}(k) = -g_{\mu\nu} + \frac{n_\mu k_\nu + k_\mu n_\nu}{n \cdot k} - n^2 \frac{k_\mu k_\nu}{(n \cdot k)^2} \quad (6.1.8)$$

Using the polarisation vectors (6.1.1) contracted with (6.1.8) one obtains the polarisation vectors (6.1.4) times some factor. This factor is included in the formula (6.1.3), but is absent in the formula (6.1.6). In this way of calculation the model PDFs do not appear in the calculation and are removed by special definition of the polarisation vectors. On the

other hand the calculation is not manifestly gauge invariant. The removal of the model PDFs works in principle only in the axial gauge. The existence of a connection between these two approaches justifies k_{\perp} -factorisation and shows that the calculation formally differs from the calculation in the collinear factorisation only by the fact that initial state gluons are off-shell and by a specific choice of the polarisation density.

SU(2) gauge invariance

In the publication [48] we note that there is freedom in choosing the polarisation sum for the massive electroweak gauge boson. The gauge freedom can be parametrised in following way

$$d_{\mu\nu}^{W/Z}(q) = -g_{\mu\nu} + \frac{q_{\mu}q_{\nu}}{q^2 - \xi m_{W/Z}^2}(1 - \xi) \quad (6.1.9)$$

Since the gauge symmetry is broken one needs to add diagrams with goldstone bosons. The propagator for the goldstone boson is parametrised by the same parameter ξ and takes the form

$$\frac{i}{q^2 - \xi m_{W/Z}^2}. \quad (6.1.10)$$

By choosing $\xi = 0$ the goldstone boson diagrams do not contribute. However, from computational reason it is more efficient to choose a gauge in which the polarisation sum of the gauge boson simplifies to $-g_{\mu\nu}$. In such a gauge the goldstone boson diagrams are necessary.

The coupling constants of the quark-goldstone boson coupling can be easily derived from the Yukawa part of the Standard Model Lagrangian.

6.1.3 Discussion of some aspects of the results

In this section we will discuss results published in [48]. We will focus on the transversal momentum distribution of the electroweak boson Z . For this purpose we will get back to the publications [40] mentioned in the section 5.1 in which the authors demonstrated how the small- x logarithm resummation can affect the transversal momentum of the Z boson at the LHC. In their formalism, motivated by [37], the cross section for Z production can be written as a convolution of PDFs, coefficient functions and modified Sudakov form factor in impact parameter \mathbf{b} space

$$\begin{aligned} \frac{d\sigma}{dyd\mathbf{q}^2} &= \frac{\sigma_0}{s} \int \frac{d^2\mathbf{b}}{(2\pi)^2} e^{-i\mathbf{q}\cdot\mathbf{b}} (\mathcal{C} \otimes f)(x_1, b_0/b_*) (\mathcal{C} \otimes f)(x_2, b_0/b_*) \\ &\times e^{-S_P(b_*, Q) - S_{NP}(|\mathbf{b}|, Q) - \mathbf{b}^2 \rho(x_1) - \mathbf{b}^2 \rho(x_2)} + Y(\mathbf{q}, Q, x_1, x_2), \end{aligned} \quad (6.1.11)$$

where σ_0 is the born cross section for the Z production, s is the proton-proton collision energy squared, Q is the hard scale of the process and the transversal momentum of Z is labeled by \mathbf{q} . The PDFs f and coefficient functions \mathcal{C} are functions of the momentum

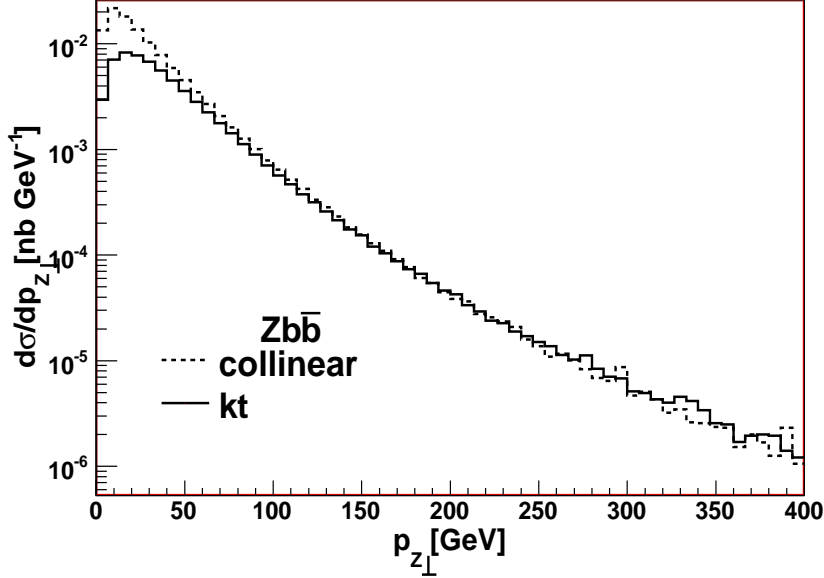


Figure 6.1.6: Transverse momentum distributions of the produced Z gauge bosons. Calculation with massive b -quarks. Both calculations are in LO of perturbation series.

fractions x_1 and x_2 and of the scale $\mu = b_0/b_*$, b_0 is a commonly appearing constant factor $2e^{-\gamma_E}$, γ_E being the Euler gamma constant. The function Y is the finite part of the Z production cross section. The parameter b_* is related to the impact parameter by the relation $b_* = |\mathbf{b}|/\sqrt{1 + \mathbf{b}^2/(0.25 \text{ GeV}^{-2})}$ and together with the non-perturbative form factor S_{NP} was introduced to take non-perturbative effects into account. The form factor S_P is the form factor calculated in [37]. The key modification to the [37] approach are the terms $\mathbf{b}^2\rho(x)$ ($x = x_1$ and $x = x_2$) which mimic a modification of the form factor by resummation of terms of the form $\alpha_S^n \ln(\mathbf{q}^2/Q^2)^l \ln(1/x)^m$. In the study done in [40] a simple form of the function ρ was chosen

$$\rho(x) = c_0 \left(\sqrt{\frac{1}{x^2} + \frac{1}{x_0^2}} - \frac{1}{x_0} \right). \quad (6.1.12)$$

The parameters x_0 and c_0 are constants which set the strength of the small- x effects. parameter x_0 sets the value of x for which the small- x dynamics starts to be important. Note that the function $\rho(x) \rightarrow c_0/x$ for small values of x and becomes small for large values of x . The authors of [40] demonstrated that the factors $e^{-\mathbf{b}^2\rho(x_{1,2})}$ for small- x cause the transversal momentum distribution of Z to get broader. At the TeVatron collision energy 1 TeV is the effect negligible and is pronounced only when one restricts the Z phase space to large rapidities $|y_Z| > 2$, but is significant at the LHC energy 14 TeV even when one integrates over the whole phase space of the Z boson.

We can now look at the cross section of the Z boson in the light of the results of [40].

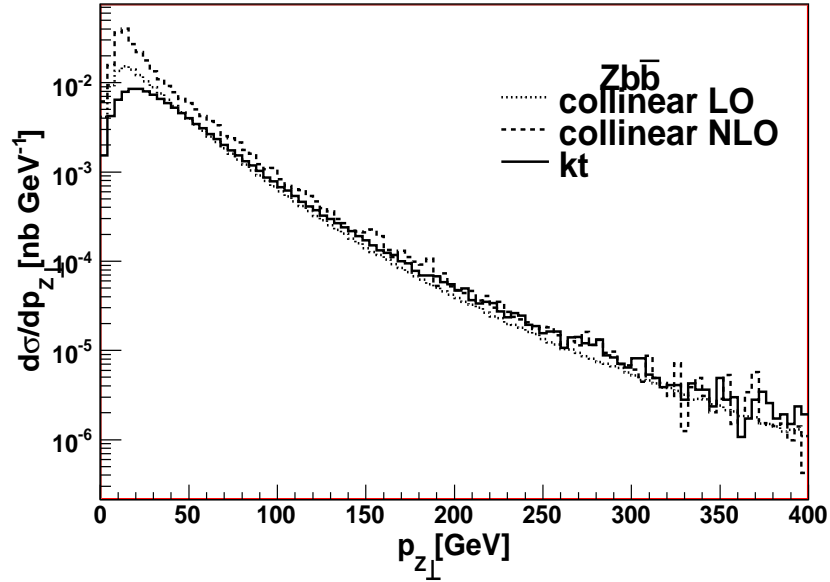


Figure 6.1.7: Comparison of cross sections differential in transverse momentum of the produced Z gauge boson. Calculation with massless b -quarks. The applied cuts are described in the text.

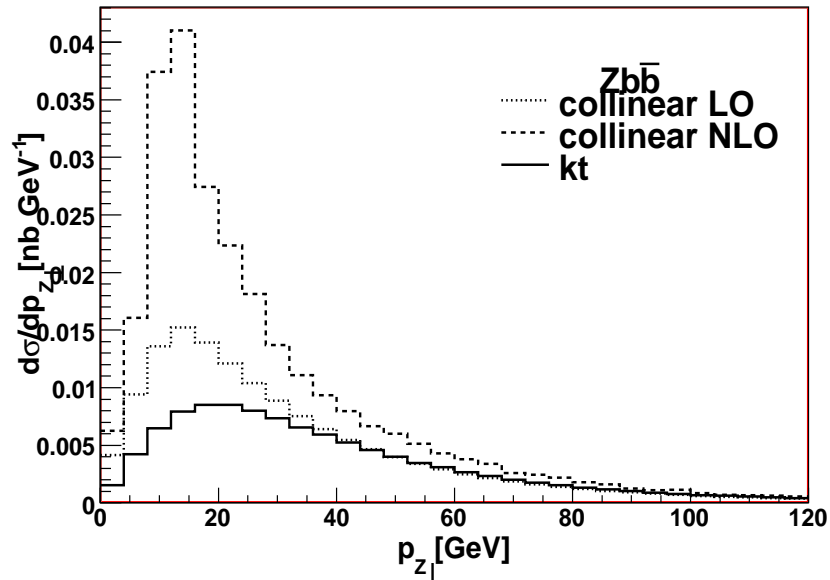


Figure 6.1.8: Comparison of cross sections differential in transverse momentum of the produced Z gauge boson (linear scale). Calculation with massless b -quarks. The applied cuts are described in the text.

The cross section of $g^*g^* \rightarrow ZQ\bar{Q}$ differential in \mathbf{p}_Z calculated using formula B.10 with $\mathcal{A}(x_{1,2}, \mathbf{k}_1^2, Q^2)$ being uPDFs which obey the CCFM equation, is plotted in figures 6.1.6, 6.1.7 and 6.1.8 (see also section B.3). In comparison with the cross section calculated using fixed order matrix element the turn-over of the \mathbf{p}_Z distribution calculated in k_\perp -factorisation is much broader which is apparent mostly from the plot 6.1.8. There are, however, some details which have to be pointed out. The transversal momentum of the Z boson in the fixed order calculation of the comparison is in leading order balanced with the transversal momentum of the quark-antiquark pair $\mathbf{p}_{q\bar{q}}$. Each $gq\bar{q}$ vertex contributes with a logarithm of $\mathbf{k}_{1,2}^2/\mu^2$. On the other hand, in k_\perp -factorisation uPDFs resum the whole set of logarithmic terms. One can therefore expect a similar effect of broadening of the transversal momentum spectrum as discussed in [40]. A broader \mathbf{p}_Z spectrum can therefore be expected and as we can see also results from the calculation in the k_\perp -factorisation framework.

We have discussed the behaviour of the \mathbf{p}_Z spectrum in energy range around $\sim 20 \text{ GeV}$ around the peak of the distribution. The behaviour at large $\mathbf{p}_Z^2 > m_Z^2$ in k_\perp -factorisation matches the behaviour of the \mathbf{p}_Z in fixed order perturbation theory. This can be understood from the fact that in k_\perp -factorisation at large \mathbf{p}_Z the transversal momenta of the initial state off-shell gluons are much smaller than \mathbf{p}_Z and can be neglected. Effectively the process $g^*g^* \rightarrow ZQ\bar{Q}$ with off-shell gluons behaves at large transversal momenta as $gg \rightarrow ZQ\bar{Q}$ with on-shell gluons. The limit for very small gluon virtualities $\mathbf{k}_{1,2}^2 \rightarrow 0$ was checked also analytically.

Our result for the transverse momentum spectrum of the electroweak gauge boson Z – \mathbf{p}_Z is consistent with theoretical expectations predicted before by [40] and shows significant modification of the transverse momentum spectrum at the turn-over compared to transverse momentum spectra calculated at a fixed order perturbation theory. As expected the cross sections agree at very large values of $|\mathbf{p}_Z|$ where the transverse momentum of the initial state gluons from uPDFs can be neglected. These results are a strong indication of consistency of the calculation [48] and show its importance for the physics at the LHC.

6.2 Z and W production associated with heavy quark-antiquark pair in HERWIG++

6.2.1 Introduction

Monte Carlo generators are important tools for predicting signals and their backgrounds measured at modern particle colliders such as the LHC and the TeVatron. In last decades a lot of effort was spent to include theoretical predictions into Monte Carlo generators to make them more reliable and to make them agree with data. Special attention was paid to the production of heavy quarks. What makes the appearance of heavy quarks in the hard process special is their heaviness - the fact that the mass of the quarks can not be neglected compared to the hard scale of the process. The mass of the heavy quark is a new scale in the hard process and results in appearance of logarithmic terms of the form

$[\alpha_S \ln(\mu^2/m_Q^2)]^n$ [51] in perturbation series. These logarithms are potentially important because they get large for large scale values.

There are two approaches to solve the problem of the heavy quark mass. First one is called *fixed flavour-number scheme* (FFNS). This approach completely ignores the logarithmic terms. Heavy quarks in FFNS appear only in the final state of the hard subprocess. Only massless flavours - $m_q < \Lambda_{QCD}$ are treated as partons. The second approach is called *variable flavour-number scheme* (VFNS). In VFNS there can be heavy quarks in the initial state of hard subprocess, but are treated as massless [52]. Massive quarks are treated as infinitely heavy below some scale μ_T and as massless above scale μ_T . The number of flavours at the scale μ_T usually chosen to be $\mu_T = m_Q$ changes from n to $n + 1$. VFNS cannot describe threshold effects. It does not take into account that heavy flavour quarks can be generated only for $\hat{s}_x = \mu^2(1/x - 1) \geq 4m_Q^2$, where \hat{s}_x is the energy between the evolving quark and the hard subprocess at the scale μ^2 , and introduces error $\mathcal{O}(m_Q^2/\mu^2)$. It is valid only for $\mu^2 \gg m_Q^2$ where the error vanishes. The threshold effects are described in FFNS where the mass effects are kept in the fixed order hard subprocess matrix elements and the mass is fully taken into account. The error which FFNS introduces is $\mathcal{O}(\Lambda_{QCD}^2/m_Q^2)$. The perturbative expansion of the hard matrix element behaves like

$$|\mathcal{M}(\alpha_S(\mu^2), m_Q^2/\mu^2)|^2 = \sum_{n=1}^{\infty} \sum_{p=q}^n \mathcal{C}_{n,p} \alpha_S^n(\mu^2) \ln^{n-p}(\mu^2/m_Q^2), \quad (6.2.1)$$

where the coefficients $\mathcal{C}_{n,p}$ are finite functions of μ^2 and q is a process dependent number. In FFNS one truncates the expansion (6.2.1). When $\mu^2/m_Q^2 \rightarrow \infty$ the terms not taken into account represent a potentially large contribution and the truncated part does not approximate the correct behaviour of the process. It would be desirable to resum all the contributions in (6.2.1) which is done in VFNS.

The aim of a Monte Carlo generator should be to describe the threshold effects, to resum the logarithmic terms and to treat the heavy quarks as massive particles.

In case of not neglecting the mass of the heavy quark in a Monte Carlo generator the mentioned logarithms would be resummed by the showering algorithm, which controls the evolution of the parton density functions and simulates soft parton radiation, taking into account that heavy quarks undergo a similar evolution/shower process as massless particles. How the parton showering of the initial state heavy partons should be modified compared to the massless case is subject of this paper. In case of the Monte Carlo generator HERWIG++ modifications which include the mass of heavy quarks has been done for the final state showering algorithm.

There is another aspect of inclusion of massive quarks into HERWIG++ initial state parton shower algorithm. In case of Drell-Yan electro-weak gauge boson (γ , Z or W^\pm) production in proton-proton scattering a fraction of the gauge bosons is produced in annihilation of heavy quarks. When the heavy quarks are tagged the proper description of the hard subprocess in FFNS would be achieved by calculating the matrix element $gg \rightarrow VQ\bar{Q}$ where V is the gauge boson and Q and \bar{Q} are the heavy quark and anti-quark. The integration of a matrix element with three particles in the final state is time consuming and

as was mentioned in the previous paragraph we would lose the resummation of the terms with powers of logarithms of ratio of heavy quark mass and the hard scale. If one would on the other hand produce the emissions of heavy quarks by shower algorithm then the terms with powers of logarithms would be resummed in Sudakov formfaktors.

6.2.2 Transverse momentum of b-quark jets in Fortran HERWIG and in HERWIG++

To motivate the effort we have to make to treat the mass effects for heavy quarks, to treat the heavy quarks differently than massless partons, we will review here the problems with bottom quark production in Fortran HERWIG and HERWIG++ Monte Carlo programs.

The process in which heavy quarks appear naturally is the Drell-Yan process where the gauge boson, a Z boson or a photon, is produced in quark-antiquark annihilation. Most of the gauge bosons are produced in light quark annihilation, but there is a fraction of events in which two heavy quarks annihilate to produce the gauge boson. To tag on such processes one can tag the heavy flavour by measuring the properties meson to which the heavy quark fragmented. The fragmented heavy quark will be typically part of a jet of particles which it produces by parton radiation. We will call the jet which includes a b-quark a b-jet.

To investigate the properties of the production of b-jets in a Monte Carlo generator one can study the properties of the distributions of observables of b-jets simulated on parton level neglecting the decay and hadronization effects.

We have plotted the correlation transversal momentum and pseudo-rapidity of the b-jet (Fig. 6.2.1) from Fortran HERWIG. In the plot one can see a gap in the transversal momentum from 0 GeV to 4 – 5 GeV. This gap is caused by a cut on the minimum transversal momentum of the radiated particle in the splitting. The cut is important in the case of $Q \rightarrow Qg$ where g is the radiated gluon in the final state. A cut on the minimum transversal momentum of the radiated gluon should in such case simulate the dead-cone [53] effect - suppression of gluon radiation from propagating heavy quark below scale m_Q . To keep the code of Monte Carlo generator HERWIG the cut on the final state showered particle is not only applied to gluons, but also to quarks. There is no reason to expect dead-cone effect in the splitting $g \rightarrow Q\bar{Q}$.

6.2.3 Initial state splitting functions in quasi-collinear limit

The inclusion of effects connected by taking the mass of the heavy quark into account should generate the dead-cone effect and avoid the presence of the cut in all the splittings present in the Monte Carlo generator HERWIG.

To include mass effects into the parton showers we decided to calculate the initial state splitting functions in the quasi-collinear limit. In quasi-collinear limit, similarly to the usual collinear limit, one assumes that the transversal momentum of the emitted parton is small, but on the other hand one assumes that $m_Q \sim p_{Q\perp}$, where m_Q is the mass of the heavy emitted parton and $p_{Q\perp}$ is its transversal momentum. The result of this approximation is that the splitting functions will depend not only on the momentum fraction of the splitted

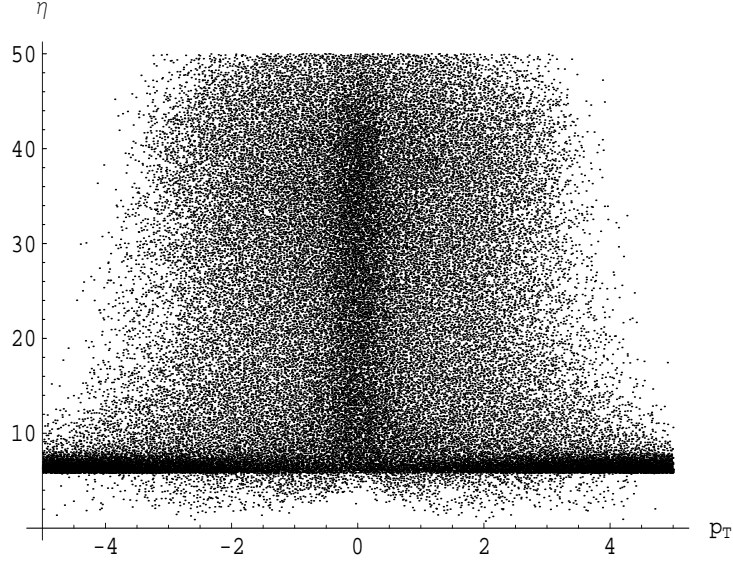


Figure 6.2.1: Rapidity-transversal momentum correlation plot.

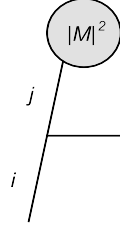


Figure 6.2.2: Schematic diagram of the calculation of the splitting function.

parton z , but also on the ratio $\frac{m_Q}{p_{Q\perp}}$. We have calculated the splitting functions in the quasi collinear limit. The results are:

$$\begin{aligned}
 P_{gQ}\left(z, \frac{m_Q}{p_{Q\perp}}\right) &= T_R \left(\frac{2m_Q^2}{m_Q^2 + p_{Q\perp}^2} z(1-z) + z^2 + (1-z)^2 \right), \\
 P_{Qg}\left(z, \frac{m_Q}{p_{Q\perp}}\right) &= C_F \left(-\frac{2m_Q^2}{z^2 m_Q^2 + p_{Q\perp}^2} z(1-z) + \frac{1-z^2}{z} \right), \\
 P_{QQ}\left(z, \frac{m_Q}{p_{Q\perp}}\right) &= C_F \left(-\frac{2m_Q^2}{(1-z)^2 m_Q^2 + p_{Q\perp}^2} z(1-z) + \frac{1-z^2}{1-z} \right).
 \end{aligned} \tag{6.2.2}$$

The index Q labels the heavy quark flavour. Because we consider the gluon as a massless parton the splitting function $P_{gg}(z, m_Q/p_{Q\perp})$ remains only a function of the momentum fraction z . The factors T_R and C_F are colour factors $\frac{1}{2}$ and $\frac{N_C^2-1}{2N_C}$ respectively.

It is easy to see that in the limit $m_Q \rightarrow 0$ we get from the splitting functions 6.2.2 the usual Altareli-Parisi splitting functions for massless quarks and gluons.

6.2.4 Evolution of massive b-quarks in HERWIG++

The evolution of parton showers in Monte Carlo HERWIG++ (and in Fortran HERWIG as well) goes backwards from the hard subprocess to the proton. This means in praxis that first the momenta of b-quarks and Z boson are generated, the hard matrix element for Drell-Yan production of Z boson is calculated and then the parton shower follows by lowering the scale starting from the hard scale Q to Q_0 where the parton shower ceases reproducing the correct parton density functions.

In PYTHIA Monte Carlo generator this has been done [8].

To implement the possibility to treat the heavy quark emission separately we have written a routine which generates the b-quark emission independently of the following parton shower routine. The independent routine will give us freedom to choose a different evolution scale for the splitting of gluon into a heavy quark-antiquark pair, to apply, as well as to remove, various cuts on the phase space variables and to include mass effects into the splitting function. At this level of the project we neglect the emissions of gluons by the heavy (anti)quark. The first branch will be the gluon splitting into a heavy quark-antiquark pair. This means that we will implement only the splitting function $P_{gQ}\left(z, \frac{m_Q}{p_{Q\perp}}\right)$. The probability of emission of a heavy quark from a backward evolving heavy antiquark in a given scale interval $(\tilde{q}, \tilde{q} + d\tilde{q})$ with any z is

$$d\mathcal{P}_{gQ}(\tilde{q}, x, m_Q) = \frac{\alpha_S(\tilde{q})}{2\pi} \frac{d\tilde{q}}{\tilde{q}} \int_x^1 dz P_{gQ}\left(z, \frac{m_Q}{p_{Q\perp}}\right) \frac{\frac{x}{z} f_g(x/z, \tilde{q})}{x f_b(x, \tilde{q})} \quad (6.2.3)$$

where x is the momentum fraction of heavy (anti)quark in the hard subprocess $Q\bar{Q} \rightarrow Z(\gamma)$.

The probability expression in equation 6.2.3 uses already all the variables and functions which are present in the parton shower algorithm. There are few places where we can include the mass of the heavy quark: the splitting function, the scale and the parton density function (PDF) of the heavy quark.

Of course we have to treat both quarks, but the procedure is the same for the other heavy quark so we focus only on one. The probability of not radiating a gluon in the same interval is

$$\mathcal{P}_Q(\tilde{q}, x, m_Q) = 1 - d\mathcal{P}_{gQ}(\tilde{q}, x, m_Q) \quad (6.2.4)$$

The probability of no emission going from higher scale \tilde{q}_0 to \tilde{q} is a product of probabilities 6.2.4 and is an exponential of expression 6.2.3

$$\Delta(\tilde{q}_0, \tilde{q}, x, m_Q) = \exp\left(-\int_{\tilde{q}}^{\tilde{q}_0} \frac{d\tilde{q}'}{\tilde{q}'} \frac{\alpha_S(\tilde{q}')}{2\pi} \int_x^1 dz P_{gQ}\left(z, \frac{m_Q}{p_{Q\perp}}\right) \frac{\frac{x}{z} f_g(x/z, \tilde{q}')}{x f_b(x, \tilde{q}')}\right) \quad (6.2.5)$$

The expression $\Delta(\tilde{q}_0, \tilde{q}, x, m_Q)$ is called the Sudakov formfaktor. Finally the probability of emission of a heavy antiquark from a backward evolving heavy quark going from higher scale \tilde{q}_0 to \tilde{q} is a product of the probabilities 6.2.5 and 6.2.3

$$\mathcal{P}_{gQ}(\tilde{q}, x, m_Q) = \frac{\alpha_S(\tilde{q})}{2\pi} \frac{d\tilde{q}}{\tilde{q}} \Delta(\tilde{q}_0, \tilde{q}, x, m_Q) \int_x^1 dz P_{gQ}\left(z, \frac{m_Q}{p_{Q\perp}}\right) \frac{\frac{x}{z} f_g(x/z, \tilde{q})}{x f_b(x, \tilde{q})} \quad (6.2.6)$$

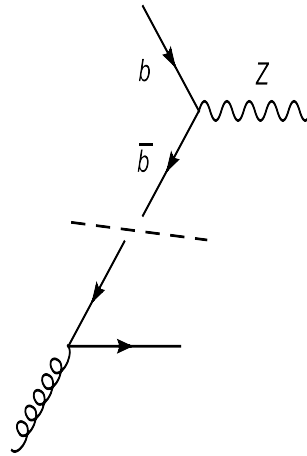


Figure 6.2.3: Schematic diagram of $b\bar{b}$ annihilation into Z boson with \bar{b} originating from $g \rightarrow b\bar{b}$ splitting.

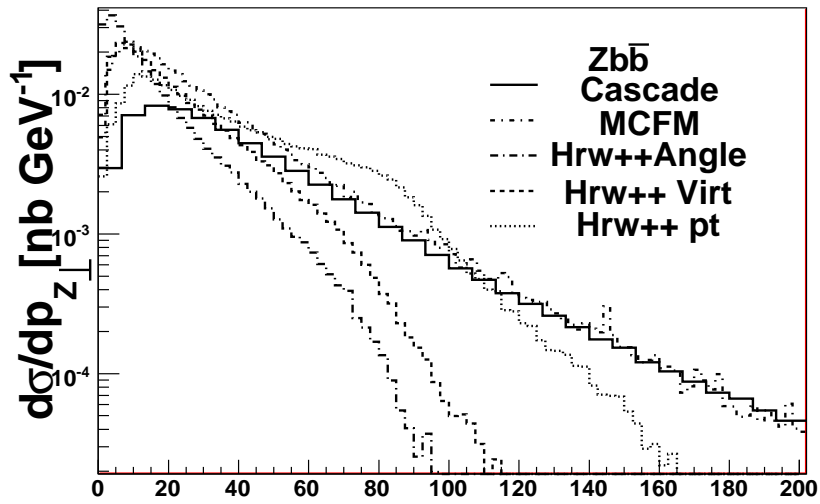


Figure 6.2.4: Transversal momentum spectrum of the Z boson for different evolution scales.

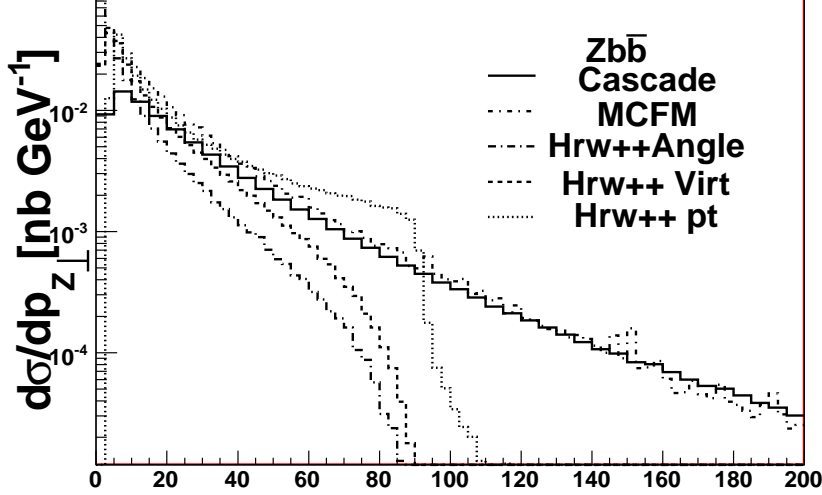


Figure 6.2.5: Transversal momentum spectrum of the b/\bar{b} quark for different evolution scales.

We will pay special attention to the scale variable \tilde{q} (appearing in all equations in this chapter). In the original parton shower algorithm in HERWIG++ we have: $\tilde{q} \sim E\theta$, where E is the energy of the incoming parton and θ is the angle between the daughters in which the incoming particle decays. This is important because it takes coherence effects into account. There is no reason to prefer this scale over other choices in case of quark emission by a gluon. On the other hand the spectrum of transversal momentum of the emitted heavy quark will strongly depend on the choice of the scale. One needs some criteria to choose the correct scale. One of such criteria is to compare the transversal momenta spectra of the final state b , \bar{b} and Z in a case where the b and \bar{b} come from parton showers with the transversal momenta spectra of the same particle calculated using the full matrix element of the subprocess $gg \rightarrow Zb\bar{b}$. We compared the spectra produced by the our heavy quark backward evolution with the spectra obtained from Monte Carlo generator MCFM where the full subprocess $gg \rightarrow Zb\bar{b}$ is implemented.

We have compared the spectra of transverse momenta (6.2.4 and 6.2.5) calculated in our approach with those obtained from Monte Carlo generator MCFM [54] using

1. $\tilde{q} = p_{Q\perp}$,
2. $\tilde{q} = p_{Q\perp}/\sqrt{1-z}$ and
3. $\tilde{q} = p_{Q\perp}/(1-z)$

where the second choice approximately corresponds to the virtuality of the evolved b -quark. The third choice approximately corresponds to the standard HERWIG++ evolution

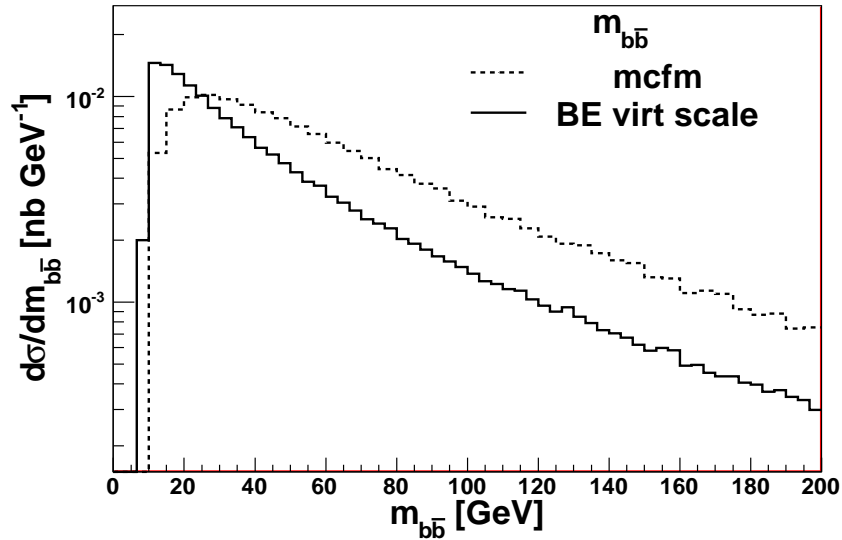


Figure 6.2.6: Invariant mass of the $b\bar{b}$ pair from HERWIG++ and MCFM

variable. As one can see from the figures 6.2.4 and 6.2.5, the best agreement of the transverse momenta spectra, at low values, are obtained by choosing $\tilde{q} = p_{Q\perp}/\sqrt{1-z}$. The transverse momenta spectra differ at large values of $p_{Q\perp}$ and $p_{Z\perp}$ because the parton shower fails in this region. The reason is that the evolution scale is restricted by the mass of the gauge boson. To correct for the high transverse momenta one needs to include matrix element corrections.

Interesting is also comparison of invariant mass of the $b\bar{b}$ pair $m_{b\bar{b}}$ spectra for which we chose as the scale, according to the results from plots 6.2.4 and 6.2.5, the virtuality of the b -quark. We see in figure 6.2.6 difference not only for large values of $m_{b\bar{b}}$, but also for small values of $m_{b\bar{b}}$.

Chapter 7

Forward jets at the LHC in high energy factorisation

In this section we will describe details of the calculations results of which are published in [55] also included in the chapter 9.

As we mentioned in previous sections, by considering a region of phase space in which the proton momentum fractions of the initial state partons are small, contributions to the scattering cross section of the form $[\alpha_S \ln(1/x)]^n$ become important and need to be resummed to save the predictivity of the perturbative approach. The importance of the small- x resummation should be more apparent if the phase space region in which x is very small is more dominant. It would be therefore interesting to study processes which are dominated by small x phase space region at very small x theoretically and also experimentally. One should observe deviations of the predictions from calculations without small x resummation with the data. On the other hand one can test the predictions of the small x resummation.

Attempts to probe small x phase space region and test the available theoretical approaches have been done with HERA [56] data and Tevatron data [57]. On this data many known approaches were tested and further improved and new approaches were developed to produce predictions which could be compared with data.

A lot of work was invested to describe the HERA forward jet measured by experiments H1 and ZEUS.

Most of the theoretical calculations dedicated for solving the problem of forward jets is based on the calculation of the cross section using the BFKL Green function. The authors of [58] calculated the azimuthal angle correlation between the outgoing lepton and a jet separated from the outgoing lepton by a rapidity distance Y as a function of Y . They made prediction of this quantity for electron proton collider LHeC which is now under discussion [59]. Similar calculations have been performed in [60].

Forward jets as a probe of small- x dynamics have become again important with coming of awaited start of the LHC. Very interesting are the prospects to measure processes probing the small x phase space region at the LHC [61–63]. An unprecedented forward rapidity coverage can be obtained by the forward calorimeters [64] of the CMS experiment.

Although the most forward calorimeters (rapidity range from 5.2 to 6.6) are not able to resolve jets in rapidity, they are able to measure the energy deposit and the azimuthal angle of the jet. In combination with a forward calorimeter (rapidity range from 3 to 5) it will be possible to measure jets in a relatively large interval of forward rapidities.

Azimuthal decorrelations between jets separated in rapidity in hadron-hadron collisions have been studied in the BFKL framework in [65]. In the first two references from [65] the authors used the NLO BFKL kernel stabilised by collinear resummation. The importance of the NLO corrections was shown in [66]. The scheme is motivated by [67] in which two approximately equally hard jets separated by a large rapidity distance were studied. In such a situation the collinear evolution between the hard jets, which assumes monotonous growth of the factorisation scale from the non-perturbative object at a small scale to a hard object at a large scale, should be suppressed because of existence of two equally large scales. This jet configuration is called *Mueller-Navalelet jets* by authors of [67]. The relevance of Mueller-Navalelet jets and azimuthal correlation between them was further discussed in [68] and [69].

In [22] and [23] the authors calculated the azimuthal correlation of Mueller-Navalelet jets using a Monte Carlo implementation of the BFKL equation. The BFKL equation they implemented into a Monte Carlo program was formally at leading order, but they included also subleading effects as the momentum conservation and running coupling. For the purpose of Monte Carlo implementation they reformulated the BFKL equation by 'unfolding' the summation over the gluon intermediate gluon emissions and by making their contributions explicit. They introduced an infrared cut-off μ_0 on the transversal momenta of the emitted gluons to separate unresolved and resolved emissions. By iteratively solving the resulting BFKL equation with the μ_0 cut-off they obtained a solution which can be directly implemented in a Monte Carlo generator to obtain exclusive final states. In the limit $\mu_0 \rightarrow 0$ they reproduced the BFKL equation.

The approach to calculate forward jet cross section and various observables in [55] (see also section 9) adopts the high energy factorisation scheme and attempts to describe forward jet production in asymmetric kinematical situation using CCFM gluon uPDF and a parton shower algorithm to describe gluon emissions.

7.1 Forward jets in asymmetric kinematical situation

Let us first recall the motivation for this calculation. The LHC will open larger phase space region allowing for hard subprocess at a typical scale $\mu^2 \gg \Lambda_{QCD}$ having at the same time the total proton-proton collision energy $s \gg \mu^2$. In such situation the momentum fraction x carried at least by one of the exchanged partons can be very small $x \sim \sqrt{\mu^2/s} \sim 10^{-5}$. It is known that the small- x region – $x < 10^{-2}$ is dominated by the gluon density. The gluon density function is much larger than other PDFs. To probe partons carrying a very small proton momentum fractions $x_{1,2}$ at the LHC energy, it is necessary to assume that $x_1 \gg x_2$. To see this we can assume $x_1 \sim x_2$ and take $\mu^2 = (2 \times 50)^2 \text{ GeV}^2$ and $s = 14000^2 \text{ GeV}^2$ – the LHC proton-proton collision energy. One finds $x_{1,2} \sim \sqrt{\mu^2/s} = 4 \times 10^{-3}$. By requiring

one of the partons to be around $x_1 \sim 0.1$, we can approach $x_2 \sim 10^{-5}$ with the other one. The consequence of such a kinematical arrangement will be that all the particles produced in the final state of the hard subprocess will be highly boosted into the high rapidity region in the direction of the proton from which the large- x parton originated. The rapidity of the system of the final state particles will be

$$y_S = \frac{1}{2} \ln \left(\frac{x_1}{x_2} \right) \sim 5. \quad (7.1.1)$$

From simple calculations we made in the previous paragraph we can see that one should look for experimental evidence of small- x dynamics in a rather large rapidity region. There are experiments close to the LHC interaction points ready to measure particle production at very large forward rapidities [61–63]. Similar measurements, however at higher proton momenta fractions, were already performed at the HERA accelerator and the data could not be satisfactorily described by conventional Monte Carlo generators like PYTHIA or HERWIG and $\mathcal{O}(\alpha_S)$ and $\mathcal{O}(\alpha_S^2)$ calculations.

In the situation when the momentum fraction of the proton carried by the parton is very small high energy logarithms could be important. To resum them we can adopt the framework developed in [25] for unintegrated parton distribution functions.

7.2 Kinematics and dynamics

We are interested in a kinematical regime where jets are produced at large rapidity y at the forward region in association with a high- p_T event - a jet in the central rapidity region. This selects configuration in proton proton scattering where a parton with a small longitudinal momentum fraction of the proton scatters with a parton carrying relatively large longitudinal momentum fraction of the second proton. We consider p_\perp of the observed jets to be high enough (eg, $|\mathbf{p}| \geq 10 \text{ GeV}$) for a perturbative treatment to apply. Because of the asymmetric kinematics, the process is sensitive to significant correlations among high- p_\perp produced across a large rapidity interval. These rapidity correlations receive contribution from regions not ordered in the transverse momenta. Taking this into account requires going beyond collinear approximations, and therefore computing k_\perp dependent matrix elements and showering. The underlying factorization formula for the forward-jet cross section is schematically

$$\sigma^{(\text{forward-jet})} = \sum_a \int \frac{d^2\mathbf{k}}{2\pi} \int_0^1 dx_1 \int_0^1 dx_2 \hat{\sigma}_{ag^*}(x_1, x_2, \mathbf{k}) f_a(x_1, \mu) f_{g^*}(x_2, \mathbf{k}, \mu) \quad (7.2.1)$$

where μ^2 is on the order of p_\perp^2 , parton g^* is small- x and off-shell, while parton a is large- x and near mass shell. The hard event depends on matrix elements M_{ag^*} with one off-shell incoming line.

In this arrangement one uses small x dynamics for the gluon and on the other hand large x dynamics for the valence quark.

7.2.1 Calculation of matrix element

We expect 3 hard subprocesses to dominate the forward jet production. In all of them there is an off-shell gluon and other on-shell parton:

$$qg^* \rightarrow qg, \quad (7.2.2)$$

$$gg^* \rightarrow gg, \quad (7.2.3)$$

$$gg^* \rightarrow q\bar{q}. \quad (7.2.4)$$

From subprocesses (7.2.2), (7.2.3) and (7.2.4) the qg^* channel will be dominant because quark PDFs dominate over gluon PDFs at $x \sim 1$. However the partonic cross section of the subprocess (7.2.3) is one order larger than the one of (7.2.2) which compensates the suppression of the gluon PDFs at large x . The result is that the subprocess (7.2.3) contributes to the forward jet cross section in magnitude comparable with the contribution of the subprocess (7.2.2). The partonic cross section of the subprocess (7.2.4) is roughly 3 orders smaller than the partonic cross sections of (7.2.2) and (7.2.3) and there is additional suppression by the gluon PDF which results in negligible contribution of (7.2.4) to the forward jet cross section.

Next we will illustrate the derivation of the unpolarised matrix elements for subprocess (7.2.2), (7.2.3) and (7.2.4) in high energy factorisation with the example of the subprocess (7.2.2).

To calculate the $qg^* \rightarrow qg$ matrix element we follow the k_T factorisation prescription. This allows by a certain choice of polarisation sum of incoming gluon to generalise the $qg \rightarrow qg$ scattering to processes where incoming gluon is off-shell. The convenient way to parametrise the four momenta of initial and final state particles is the following:

$$k = \alpha_1 p_1 + k_\perp \quad (7.2.5)$$

$$q = \beta_1 p_2 \quad (7.2.6)$$

$$k' = \alpha'_1 p_1 + \beta'_1 p_2 + k'_\perp \quad (7.2.7)$$

$$q' = \alpha'_2 p_1 + \beta'_2 p_2 + q'_\perp \quad (7.2.8)$$

where $p_1 = (\sqrt{\frac{s}{2}}, 0, 0, 0)$ and $p_2 = (0, 0, 0, -\sqrt{\frac{s}{2}})$ are the four-momenta of the beam protons, k , q , k' and q' are the initial state gluon, valence quark, final state gluon and final state quark four-momenta respectively. The initial state gluon is off-shell by $k^2 = -\mathbf{k}^2$, while the other partons satisfy $q^2 = 0$, $q'^2 = 0$, $k'^2 = 0$. The longitudinal components expressed in the Lorentz invariant expressions are:

$$\alpha_1 = \frac{k \cdot p_2}{p_1 \cdot p_2}, \beta_1 = \frac{q \cdot p_1}{p_1 \cdot p_2}$$

$$\alpha'_1 = \frac{k' \cdot p_2}{p_1 \cdot p_2}, \beta'_1 = \frac{k' \cdot p_1}{p_1 \cdot p_2}, \alpha'_2 = \frac{q' \cdot p_2}{p_1 \cdot p_2}, \beta'_2 = \frac{q' \cdot p_1}{p_1 \cdot p_2} \quad (7.2.9)$$

$$(7.2.10)$$

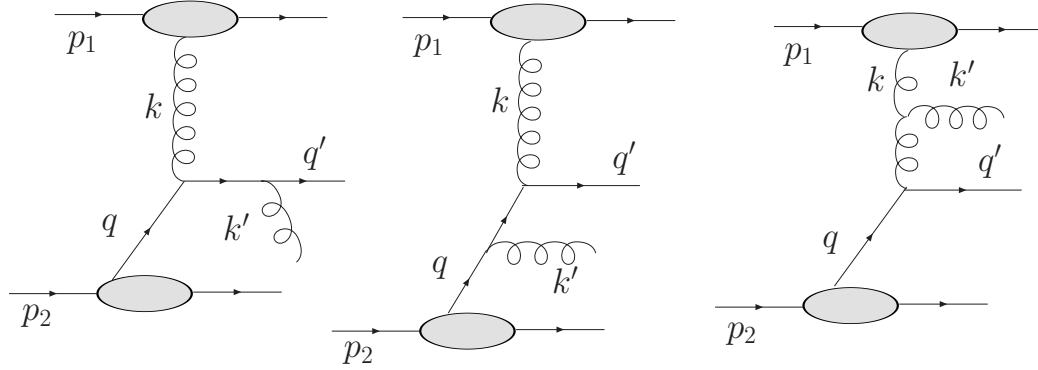


Figure 7.2.1: Set of diagrams of $q g^* \rightarrow q g$ with initial state gluon off-shell and initial state quark on-shell.

The expressions for the amplitude reads:

$$\begin{aligned} \mathcal{M}_{\xi\xi'} = & -i g_S^2 \bar{u}_\xi(q') \left[\hat{\epsilon}_{\lambda'}^* t_a \frac{\hat{q} + \hat{k}}{(q+k)^2} u t_b \hat{\epsilon}_\lambda + \hat{\epsilon}_{\lambda'}^* t_b \frac{\hat{k}' - \hat{q}}{(k'-q)^2} t_a \hat{\epsilon}_\lambda \right. \\ & \left. + i \epsilon_{\lambda'}^{*\mu} V_{\mu\nu\kappa}^{abc} \epsilon_\lambda^\kappa \frac{d^{\nu\zeta}}{(q-q')^2} t_c \gamma_\zeta \right] u_{\xi'}(q) \end{aligned} \quad (7.2.11)$$

where "hat" on a momentum variable means contraction with a gamma matrix, $\epsilon_\lambda \equiv \epsilon_\lambda^\mu(k')$ is the polarization of initial state gluon, $\epsilon'_\lambda \equiv \epsilon_\lambda^\mu(k')$ is the polarization of final state gluon, V is the triple gluon vertex

$$V_{\mu\nu\kappa}^{abc} = f_{abc} [-g_{\mu\nu}(k' - 2k)_\kappa - g_{\mu\kappa}(k + k')_\nu + g_{\nu\kappa}(2k' - k)_\mu] \quad (7.2.12)$$

and $u(\bar{u})$ denotes $u \equiv u(q, \zeta)$ ($\bar{u} \equiv \bar{u}(q', \xi)$) and the $d^{\nu\zeta}$ in lightcone gauge is

$$d_{\nu\zeta} = g_{\nu\zeta} - \frac{p_{1\nu}(q - q')_\zeta + p_{1\zeta}(q - q')_\nu}{p_1 \cdot (q - q')} \quad (7.2.13)$$

where p is a lightlike vector satisfying $p_1^2 = 0$. Using the k_T factorisation prescription the sum over polarisation on incoming gluon is:

$$\sum_\lambda \epsilon_\lambda^\mu(k) \epsilon_\lambda^\nu(k) = \frac{2k_T^\mu k_T^\nu}{\mathbf{k}^2} \quad (7.2.14)$$

while for outgoing gluon we have:

$$\sum_{\lambda'} \epsilon_{\lambda'}^\mu(k') \epsilon_{\lambda'}^\nu(k') = -g_{\mu\nu} + \frac{k'_\mu p_{1\nu} + k'_\nu p_{1\mu}}{p_1 \cdot k'} \quad (7.2.15)$$

We then obtain for the unpolarized matrix element squared $|\mathcal{M}|^2$

$$|\mathcal{M}|^2 = \frac{1}{4} \frac{1}{N_c(N_c^2 - 1)} \left(C_A C_F^2 A_{abelian} + C_A^2 C_F A_{non-abelian} \right) \quad (7.2.16)$$

where

$$A_{abelian} = (4\pi\alpha_s)^2 \left(\frac{k \cdot q}{p_1 \cdot q} \right)^2 \frac{(p_1 \cdot q)^2 + (p_1 \cdot q')^2}{k' \cdot q \ k' \cdot q'} \quad (7.2.17)$$

and

$$A_{non-abelian} = (4\pi\alpha_s)^2 \left(\frac{k \cdot q}{p_1 \cdot q} \right)^2 \frac{(p_1 \cdot q)^2 + (p_1 \cdot q')^2}{2k' \cdot q \ k' \cdot q'} \left(\frac{2k' \cdot q' \ p_1 \cdot q}{-t \ k' \cdot p_1} + \frac{2k' \cdot q \ p_1 \cdot q'}{-t \ k' \cdot p_1} - 1 \right) \quad (7.2.18)$$

with $C_A = N_c$, $C_F = (N_c^2 - 1)/(2N_c)$ and N_c being the number of colours. The limit $k_\perp \rightarrow 0$ can be performed and the collinear matrix element for $qg \rightarrow qg$ is recovered.

The derivation of the matrix elements for subprocesses (7.2.3) and (7.2.4) is analogous to the derivation described above. However, there is another way how to derive the same expressions for the matrix elements by using $2 \rightarrow 3$ processes and performing the small x limit. The initial partons in a $2 \rightarrow 3$ process carry momenta p_1 and p_2 . By performing the limit in which the 4-products between p_2 and 4-momenta k , q , k' and q' and among each other are of the same order and very small compared to dot-products with p_1 one obtains the matrix element for a $2 \rightarrow 2$ subprocess with momentum k being off-shell times a simple calculable factor. For a cross check the matrix elements were derived also using last mentioned method.

7.3 Implementation into Monte Carlo program

There are collinear singularities present in the matrix elements which have to be avoided by cuts on transversal momenta of the final state partons.

We use running coupling in our calculations $\alpha_s(\mu_R^2)$. We choose the scale for $\mu_R^2 = \max(\mathbf{k}'^2, \mathbf{q}'^2)$.

To avoid the collinear singularities we applied cuts $|\mathbf{k}'| > |\mathbf{k}'_{\min}|$ and $|\mathbf{q}'| > |\mathbf{q}'_{\min}|$ on final state transversal momenta. To obtain the proper collinear limit we choose $|\mathbf{q}'_{\min}| = |\mathbf{k}'_{\min}|$. Transversal momenta of the final state partons provide a hard scale which also ensures factorization. We have implemented the matrix element into the Monte Carlo generator CASCADE. We have to note that in the program the parton showers from the valence quark side are at the moment not available. Only parton showers from the initial gluon side are available. However, we can safely say that the presence of extra radiation from the valence quark side will not make a significant contribution to jet cross sections because the gluon radiation from a quark is dominated by soft emissions and we expect that they will not affect the jet analysis.

7.4 Results

The calculation described in previous section is important especially for jet production at very forward rapidity intervals at the LHC experiments. To investigate experimentally

measurable quantities we focus our attention on existing detector of CMS experiment which is covering very forward rapidity region: the Hadronic Forward (HF)-CMS calorimeter covering the pseudo rapidity region $3 < \eta < 5$.

Inspired by the analyses done for Mueller-Navale jets described in the beginning of the section 7 we have studied azimuthal angle correlations $\Delta\phi$ of a forward jet in HF rapidity region and a jet in the central rapidity region $|\eta| < 2$ (later referred to as central rapidity region). We expect that the central jets will be dominantly produced from the parton showers from the gluon evolution chain. The forward jets will be mostly produced by the fragmentation of hard subprocess partons.

We are also interested in the energy flow, transversal momentum and jet multiplicity in forward and central rapidity region which are directly affected by the parton shower algorithm.

We compare our results with the results obtained from PYTHIA Monte Carlo generator which is based on collinear factorization, we also check the influence of a model for multiple parton interactions (MPI). Since the unintegrated CCFM parton showers increase the decorrelation between jets and predict higher jet multiplicities, it is interesting to compare the CCFM parton showers with DGLAP parton showers with a MPI model to see how MPI can mimic CCFM effects and to which degree these two are distinguishable. We will therefore compare our results obtained using the CCFM parton showers with those obtained using PYTHIA with MPI model switched on.

7.4.1 Transversal momentum and energy flows in forward rapidity region

Because of the higher jet activity produced in a CCFM based shower and a different treatment of transversal momentum we expect differences in the spectra of transversal momentum of jets especially in the forward rapidity regions.

To calculate the cross sections we have chosen the gluon uPDF set A0. For the initial state quark density we used non-singlet quark CTEQ6.0 PDF evolved by the CCFM equation. In PYTHIA we used CTEQ 5L PDFs and default p_{\perp}^2 and opening angle ordered parton showers [8]. We have used options with MPI switched on and off and MPI model switched by the default option for MSTP(82).

We select one jet in the central rapidity region $|\eta_{cj}| < 2$ and the other one jet as the hardest jet in the forward region $3 < \eta_{fj} < 5$ with a transversal momentum of the jet $|\mathbf{p}_{fj}| > 35 \text{ GeV}$. We have to require a second jet because the hard subprocess was calculated for two jets. One jet observable is not relevant because a virtual correction would be necessary to remove the singularity from the real $2 \rightarrow 2$ sub-graphs.

In figure 7.4.1 we have plotted the transversal momentum of jets in the rapidity region $3 < \eta_{fj} < 5$, where η_{fj} is the rapidity of the forward jet, requiring jet in the forward rapidity region and simultaneously requiring a jet in the central rapidity region $|\eta_{cj}| < 2$. From the plot in figure 7.4.1 we can see that the cross section as a function of transversal momentum of the jets calculated using CASCADE is comparable with the cross section obtained from PYTHIA with MPI switched off. One can see that the MPI increase the

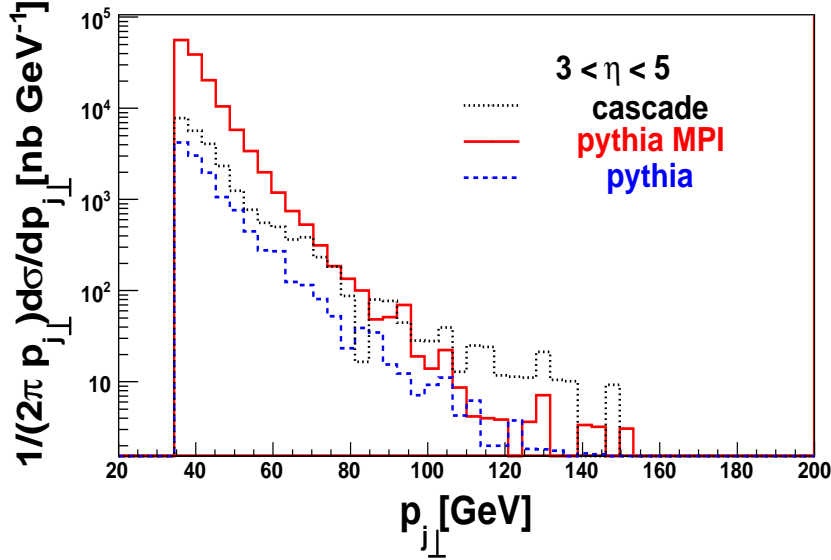


Figure 7.4.1: Transversal momentum of jets in for pseudo-rapidity of jets $3 < \eta_j < 5$.

observed cross section up more for lower transversal momentum of the jets and make the distribution steeper. The shape of the transversal momentum spectrum calculated using CASCADE is slightly harder than the one predicted by PYTHIA which can be seen from slightly different slopes of distributions.

In the plot of forward jet multiplicity, figure 7.4.2, the first number of the interval of the bin gives the information on the number of jets with transversal momentum $\mathbf{p}_{fj} > 35 \text{ GeV}$ and $\mathbf{p}_{fj} > 20 \text{ GeV}$ respectively. On the y axis is the fraction of the events with certain forward jet multiplicity.

Jet multiplicity plot in figure 7.4.2 shows that the number of forward jets selected to be in the rapidity region $3 < \eta_{fj} < 5$ is very similar for PYTHIA without MPI and CCFM based parton shower in CASCADE. CCFM based parton shower produces slightly more very high jet multiplicity, $n_{jf} \geq 3$, events. The cross section for the production of forward jets predicted by PYTHIA with MPI parton showers is higher than the one predicted by CASCADE with CCFM parton showers.

In the figure 7.4.3 is azimuthal correlation plotted in rapidity region $3 < \eta_{fj} < 5$. The figure 7.4.3 shows that the shape and also the size of the cross section for CCFM based parton shower is very similar to the one obtained from PYTHIA without MPI. PYTHIA with MPI predicts much bigger cross section than CASCADE and PYTHIA without MPI. This is consistent with previous plot in figure 7.4.1. The cross section calculated in CASCADE is flatter at $\Delta\phi_j \sim \pi$ than the one calculated in PYTHIA. This is consistent with the transversal momentum spectrum (figure 7.4.1) which is harder for CASCADE than for PYTHIA.

Last we discuss (figure 7.4.4) the average azimuthal deviation from a back-to-back con-

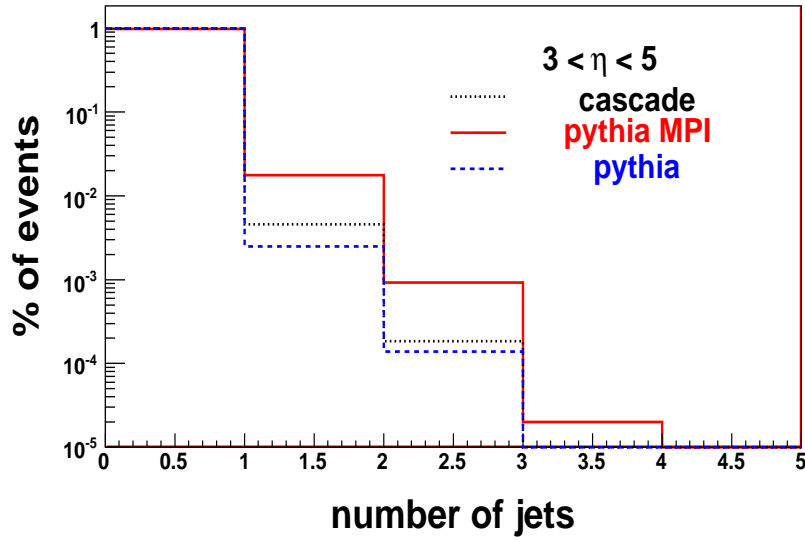


Figure 7.4.2: Multiplicity of jets in a single event for pseudo-rapidity of jets $3 < \eta_j < 5$.

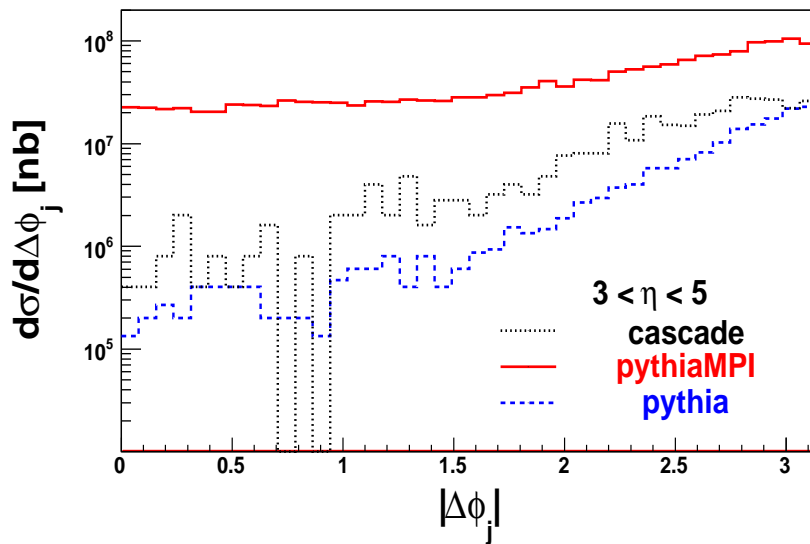


Figure 7.4.3: Azimuthal correlation of jets in for pseudo-rapidity of the forward jet $3 < \eta_j < 5$.

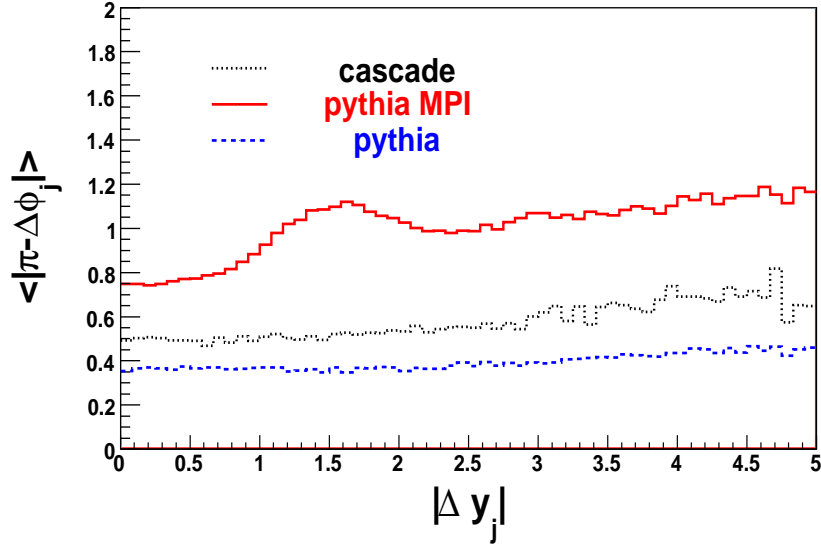


Figure 7.4.4: Average azimuthal correlation as a function of the rapidity distance of the jet pair.

figuration $|\pi - |\Delta\phi||$ of two hardest jets with $\mathbf{p}_j > 20 \text{ GeV}$ depending on the relative rapidity distance of the jets $|\Delta y|$. No restriction on the jet rapidity was imposed. In this case PYTHIA with MPI predicts roughly 40% bigger average $|\pi - |\Delta\phi||$ than the unintegrated parton shower Monte Carlo. The $|\pi - |\Delta\phi||$ distribution calculated in CASCADE has the same shape as the distribution calculated in PYTHIA without MPI which predicts slightly smaller $|\pi - |\Delta\phi||$ than the CCFM based parton shower Monte Carlo. The large value of $|\pi - |\Delta\phi||$ in PYTHIA is caused by the presence of MPI which slightly increases this quantity.

Chapter 8

Summary and Conclusions

To describe the transversal momentum spectrum of an electro-weak gauge boson it is necessary to go beyond fixed order perturbation theory. It is needed to resum whole classes of enhanced logarithmic terms. Depending on the phase space region different classes of logarithmic terms can be important. There are different approaches to sum such logarithmic terms including evolution equations of parton density functions. The evolution equation DGLAP which is valid for integrated parton density functions can be used to effectively produce unintegrated parton density functions using parton shower algorithm, but this approach involves kinematical approximations. With opening of phase space region $\Lambda_{QCD}^2 \ll \mu^2 \ll s$ at the LHC approaches based on the BFKL and the CCFM equations are becoming more relevant. The BFKL and the CCFM equations define genuine unintegrated parton density functions which can be convoluted with matrix elements with off-shell initial state gluons.

Off-shell matrix elements for $Z/W + Q\bar{Q}$ production were calculated and Monte Carlo CASCADE based on the CCFM evolution equation was used to study phenomenology. Special attention was given to observables connected with the electro-weak gauge boson for the LHC kinematics. The widening of the turn-over of the transversal momentum spectrum of the electroweak boson is observed and discussed. It was pointed out in [40] that the turn-over of the transversal momentum spectrum of the electro-weak gauge boson becomes wider by taking the small- x dynamics into account. The results were compared with results obtained in collinear factorisation in LO and NLO calculated using Monte Carlo generator MCFM. We conclude that some of the effects of NLO and even higher order collinear calculation are already included in the LO k_T -factorization calculation.

To improve the calculation additional channels to the process $g^*g^* \rightarrow Z/W/\gamma + q\bar{q}$ can be included. As we already mentioned this was done in [45] in the KMR approach for the quark uPDF, but one can go beyond this approach by using off-shell $g^* \rightarrow q\bar{q}$ splitting function or by using one-loop CCFM equation for the quark uPDF [41, 42] or even by defining evolution of the quark uPDF the way it was done in [50] and implementing it into Monte Carlo shower program.

The forward jet production using unintegrated parton density functions and off-shell matrix elements at the LHC was studied as a probe for small- x dynamics. We have anal-

used the high-energy factorisation that serves to sum consistently higher orders in α_s both the logarithmic corrections in the large rapidity interval and those in the hard jet transverse energy. The gauge-invariant (though not on shell) high-energy amplitudes, which are needed to evaluate the factorisation formula for forward jet hadroproduction were determined. The hard matrix elements were implemented in a fully exclusive Monte Carlo program and phenomenology of forward jets was studied. The results were compared with calculation using Monte Carlo generator PYTHIA. Differences in azimuthal decorrelation and harder forward jet transversal momentum spectrum were discussed. Due to unintegrated transversal momentum from the uPDFs and by taking it into account in the hard matrix elements the parton showers are better approximation for multijet final states than parton showers based on collinear factorisation. MPI used in PYTHIA predicts much more jet activity than the unintegrated shower and there are a differences in azimuthal decorrelation and transversal momentum distributions which could be used to estimate the amount of MPI and small- x dynamics required to describe data at the LHC.

The inclusive cross section of the forward jet production is dependent on an arbitrary cut on transversal momentum of the final state particles which have to be applied to regularise the partonic cross section. It would be possible to remove the dependence on this cut by approximating the hard subprocess matrix element by product of a splitting function and matrix element for a $2 \rightarrow 1$ process for small $t = (q - q')^2$ and $u = (q - k')^2$ (as defined in section 7), including also virtual corrections in a form of a Sudakov form factor, and define a suitable matching between the regime with full matrix element and approximation.

Chapter 9

Appendix

A Discussion of the method of orthogonal amplitudes

When we want to calculate amplitude squared of some process in quantum field theory usually we deal with expressions of the form

$$|\mathcal{M}_\Gamma|^2 = \text{Tr}\{\bar{u}_\lambda(k_1, m_1) \hat{\Gamma} u_\zeta(k_2, m_2) \bar{u}_\zeta(k_2, m_2) \hat{\Gamma}^\dagger u_\lambda(k_1, m_1)\}, \quad (\text{A.1})$$

where $u_\lambda(k_1, m_1)$ and $u_\zeta(k_2, m_2)$ are spinors of final or initial state fermions in diagram connected by a fermion line. In this chapter we will present a simple way - method of orthogonal amplitudes [70] - to calculate such expressions and avoid encounter of long resulting formulas.

In the method of orthogonal amplitudes one defines gamma matrices \hat{O}_i , $i \in \{1, \dots, 4\}$ in such a way that

$$(\hat{O}_i, \hat{O}_j) = \text{Tr}\{\bar{u}_\lambda(k_1, m_1) \hat{O}_i u_\zeta(k_2, m_2) \bar{u}_\zeta(k_2, m_2) \hat{O}_j^\dagger u_\lambda(k_1, m_1)\} = \|\hat{O}_i\|^2 \delta_{ij}, \quad (\text{A.2})$$

where $\|\hat{O}_i\|$ is a norm of the operator \hat{O}_i defined by the operator dot-product in equation (A.2).

Let us define objects $S_{\lambda\zeta}^i(k_1, m_1; k_2, m_2)$ by relation

$$S_{\lambda\zeta}^i(k_1, m_1; k_2, m_2) = \bar{u}_\lambda(k_1, m_1) \hat{O}_i u_\zeta(k_2, m_2). \quad (\text{A.3})$$

Then the relation (A.2) translates into equation

$$S_{\lambda\zeta}^i(k_1, m_1; k_2, m_2) S_{\zeta\lambda}^{j\dagger}(k_1, m_1; k_2, m_2) = \|S^i\|^2 \delta_{ij}. \quad (\text{A.4})$$

Since objects $S_{\lambda\zeta}^i$ depend on the spin indices of fermions in the process - λ , ζ and on the choice of the operator - index i , it can be interpreted as a certain projection of the fermion spin state. It carries information about the spin configuration of the fermions on the fermion line. Projection have to be done for each fermion line separately, because each fermion line in a diagram corresponds to an independent trace over spin indices.

If one adopts matrix formalism for the objects $S_{\lambda\zeta}^i$, which are indeed nothing more than 2×2 matrices, one can write instead of (A.4)

$$(\mathbf{S}^i, \mathbf{S}^j)_{u(2)} = \text{Tr}\{\mathbf{S}^i \cdot \mathbf{S}^{j\dagger}\} = \|\mathbf{S}^i\|_{u(2)}^2 \delta_{ij}. \quad (\text{A.5})$$

Let us point out that the trace in the equation (A.5) is over different indices than in equation (A.2). Matrices form a basis in the space of 2×2 matrices with complex components - $\mathbb{C}^2 \times \mathbb{C}^2$, satisfying the relation $\mathbb{S}^{i*} = \mathbb{S}^{i\text{T}} - u(2)$ which is indeed a 4-dimensional Lie algebra.

A practical choice of operators \hat{O}^i is to choose two four-vectors L and K which satisfy the relations

$$L^2 = -1, \quad K^2 = -1, \quad L.K = 0, \quad (\text{A.6})$$

$$L.k_1 = 0, \quad K.k_1 = 0, \quad L.k_2 = 0, \quad K.k_2 = 0. \quad (\text{A.7})$$

Using four-vectors K and L one can construct the operators \hat{O}^i

$$\hat{O}_S^1 = \mathbf{1}, \quad (\text{A.8})$$

$$\hat{O}_S^2 = \hat{K}, \quad (\text{A.9})$$

$$\hat{O}_S^3 = \hat{L}, \quad (\text{A.10})$$

$$\hat{O}_S^4 = \hat{K}\hat{L}. \quad (\text{A.11})$$

However, we know that there are projectors on the spin states constructed from gamma matrices. It must be possible to express these projectors, in the sense of objects one to one correspondence of matrices \mathbf{S}^i , as linear combination of operators \hat{O}_S^i . The goal is to find coefficients a_i in the expansion of the spin projectors by solving the equation

$$\bar{u}_\lambda(k_1, m_1) \left(\frac{\mathbf{1} \pm \gamma^5}{2} \right) u_\zeta(k_2, m_2) = \bar{u}_\lambda(k_1, m_1) \left(\sum_{i=1}^4 a_i^\pm \hat{O}_S^i \right) u_\zeta(k_2, m_2). \quad (\text{A.12})$$

The coefficients can be obtained using the formula (A.2)

$$a_i^\pm = \left(\frac{\mathbf{1} \pm \gamma^5}{2}, \hat{O}_S^i \right) / \|\hat{O}_S^i\|^2. \quad (\text{A.13})$$

The coefficients for this particular choice of operators \hat{O}_S^i are

$$a_1^\pm = \frac{1}{2}, \quad (\text{A.14})$$

$$a_2^\pm = 0, \quad (\text{A.15})$$

$$a_3^\pm = 0, \quad (\text{A.16})$$

$$a_4^\pm = \mp \frac{1}{2} \frac{\epsilon_{\kappa\mu\nu\sigma} k_1^\kappa k_2^\mu K^\nu L^\sigma}{m_1 m_2 + k_1 \cdot k_2}. \quad (\text{A.17})$$

These coefficients can be used to calculate the polarised matrix elements - not averaged over the spin of fermions. If we use orthogonal amplitudes in our calculation to derive the unpolarised matrix element it is straight forward, using the coefficients (A.14) to obtain matrix elements for certain polarisation states of fermions.

Coefficients in a similar expansion for a general operator $\hat{\Gamma}$ can be obtained in the same way. The coefficients can be obtained using the formula (A.2)

$$g_i = (\hat{\Gamma}, \hat{O}_S^i) / \|\hat{O}_S^i\|^2. \quad (\text{A.18})$$

The expression from equation (A.1) can be reconstructed by formula

$$|\mathcal{M}_\Gamma|^2 = \sum_{i=1}^4 g_i^2 \|\hat{O}_S^i\|^2 = \sum_{i=1}^4 (\hat{\Gamma}, \hat{O}_S^i)^2 / \|\hat{O}_S^i\|^2. \quad (\text{A.19})$$

If $\hat{\Gamma}$ consists from products of more than one gamma matrix then the number n of gamma matrices in products in traces which have to be calculated analytically (if one chooses to do it that way) is reduced from $2n + 2$ to roughly $n + 3$. In practice it means that the complexity of the analytical expressions can be significantly reduced.

B Z and W^\pm production associated with quark-antiquark pair in k_T -factorization at the LHC

DESY-08-
CPHT-RR025.0408

**Z and W^\pm production associated with quark-antiquark pair
in k_T -factorization at the LHC**

Michal Deák¹, Florian Schwennsen²

¹*DESY, Hamburg, Notkestrasse 85, D-22607 Hamburg, Germany*

²*Centre de Physique Théorique, École Polytechnique, F-91128 Palaiseau, France*

Abstract

We calculate and analyze Z and W^\pm production in association with quark-antiquark pair in k_T -factorization. Numerical calculations are performed using the Monte Carlo generator CASCADE for proton proton collisions at LHC energy. We compare total and differential cross sections calculated in k_T -factorization approach with total differential cross sections obtained in LO and NLO calculations in collinear factorization approach. We provide strong evidence that some of the effects of the NLO and even higher order collinear calculation are already included in the LO k_T -factorization calculation.

B.1 Introduction

In the following years new discoveries are expected at the LHC concerning physics within the Standard Model and beyond it. The discovery of the Higgs boson and exclusion or affirmation of possible extensions or alternatives to the Standard Model will be of special interest. To be able to measure the proposed signals of processes which open the access to new physics a very good understanding of the detectors and their responses to produced particles will be needed. An accurate calibration of particle detectors could be achieved by using processes with well known cross sections in which particles with well known properties are produced. A calibration of LHC detectors using W or Z signals is proposed in several publications [71]. Moreover, the W or Z production is important because it plays a significant role in background processes connected to Higgs production. Another experimental motivation is provided by the possibility to measure the luminosity via Z boson production [72].

At the Tevatron collider W/Z production takes place at a typical $x = \sqrt{M_W^2/s} \approx 0.04$ and hence is dominated by scattering of quarks. Because of the much higher energy, proton scattering at LHC will allow smaller proton energy fractions and will be dominated by gluon scattering.

The W mass provides a hard scale and allows a perturbative calculation of the hard matrix element. The resummation of large logarithms of the form $[\alpha_s \ln(\mu^2/\Lambda_{\text{QCD}}^2)]^n$ (where $\mu^2 \sim M_W^2$, $\mu^2 \gg \Lambda_{\text{QCD}}^2$) can be performed in the framework of the Dokshitzer-Gribov-Lipatov-Altarelli-Parisi (DGLAP) equation [7], leading to the collinear factorization into conventional parton densities and a hard scattering matrix element. While in the conventional collinear approach the longitudinal momentum fraction is considered to be dominant, such that the transverse momenta of the partons can be neglected as well as their virtualities, at small x the transverse momenta entering the hard matrix element should become relevant.

At the LHC the larger center of mass energy allows W/Z production at even smaller x such that the production of particles will be dominated by gluon-gluon fusion. Moreover, in this situation we have to deal with two different large scales ($s \gg \mu^2 \gg \Lambda_{\text{QCD}}^2$) and logarithms of the form $[\alpha_s \ln(1/x)]^n$ arise which have to be resummed. This is realized by the leading logarithmic (LL) Balitsky-Fadin-Kuraev-Lipatov (BFKL) equation [17] or the Ciafaloni-Catani-Fiorani-Marchesini (CCFM) evolution equation [25] which additionally resums terms of the form $[\alpha_s \ln(\mu^2/\Lambda_{\text{QCD}}^2)]^n$ and $[\alpha_s \ln(\mu^2/\Lambda_{\text{QCD}}^2) \ln(1/x)]^n$. Just as for DGLAP, it is possible to factorize the cross section into a convolution of process-dependent hard matrix elements with universal parton distributions. But as the virtualities and transverse momenta are no longer ordered (as it is the case in DGLAP evolution), the matrix elements have to be taken off-shell, and the convolution has to be made also over transverse momenta with the so-called *unintegrated parton densities*. This factorization scheme is called k_T -factorization [73, 74] or *semi-hard approach* [75] and will be used in this work.

There is also the notion of *transverse momentum dependent* (TMD) parton distributions [76]. But although in these approaches the transverse momentum of the parton is taken into

account as well, this is only the case on the side of the parton density. The matrix element is calculated with incoming on-shell partons, and transversal momenta of the incoming partons are neglected. It has been shown [6] that factorization within this approach is violated beyond NLO. In case of the k_T -factorization approach used in this work this is also expected. Indeed, it is well known that in the BFKL approach beyond NLO multiple gluon exchange in the t -channel has to be taken into account.

In this paper we calculate and analyze Z and W production associated with two quark jets provided by gluon-gluon fusion in k_T -factorization. We assume quasi-multi-Regge-kinematics (QMRK) where the cluster of W/Z and the two quarks is well separated in rapidity from the proton remnants while the kinematics within that cluster is considered without any further assumption. In particular, we take into account the mass of the quarks. In this kinematic regime a gauge independent off-shell matrix element can be extracted due to high energy factorization. A similar calculation has been done in [77], where the authors calculated photon (instead of Z/W) production in the same framework. We calculated the matrix element independently and extended it to massive gauge bosons. In our work on massive gauge bosons production we especially focus on the predictions for LHC and compare with a collinear factorization based calculation.

The paper is organized in the following way: In section 2 we describe notation, kinematics of the process and the calculation of the matrix element. In section 3 we present numerical results obtained from a calculation using the Monte Carlo generator CASCADE [26], where the matrix element squared was implemented. In section 4 we summarize the results and offer conclusions.

B.2 Kinematics of Z/W production and calculation of the hard matrix element

We label the 4-momenta of incoming hadrons with masses m_A and m_B by p'_A and p'_B , respectively. In the center of mass system they can be expressed in terms of invariant light like vectors p_A and p_B

$$p'_A = p_A + \frac{m_A^2}{s} p_B, \quad p'_B = p_B + \frac{m_B^2}{s} p_A. \quad (\text{B.1})$$

In the case of protons at the LHC we have $m_A^2 = m_B^2 = m_p^2$ which satisfies the relation $\frac{m_p^2}{s} \ll 1$. Therefore, we can neglect the masses in Eqs. (B.1) and use $p_{A,B}$ instead of $p'_{A,B}$.

It is convenient to use Sudakov decomposition for all momenta present in the calculation (see also Fig. B.1¹) by decomposing them into components proportional to p_A and p_B , and a remainder perpendicular to both of them

$$k_i = \alpha_i p_A + \beta_i p_B + k_{i\perp}, \quad (\text{B.2})$$

where $i \in \{1, 2, W(Z)\}$ for outgoing particles, and

$$q_1 = \alpha q_1 p_A + \beta q_1 p_B + q_{1\perp}, \quad q_2 = \alpha q_2 p_A + \beta q_2 p_B + q_{2\perp} \quad (\text{B.3})$$

¹These and the following diagrams were drawn in JaxoDraw [78].

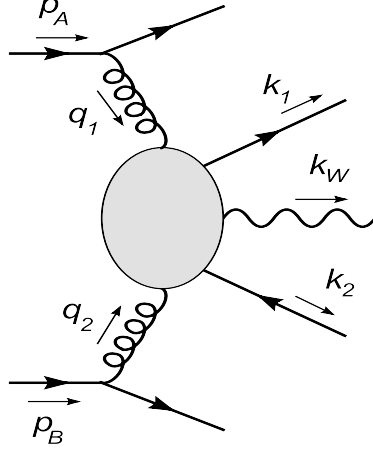


Figure B.1: Labeling and flow of momenta of the process $pp \rightarrow q(W/Z)\bar{q}X$.

for the gluons entering the hard matrix element. It is also convenient to introduce Euclidean two dimensional vectors \vec{k}_i and \vec{q}_j which satisfy the relations $\vec{k}_i^2 = -k_{i\perp}^2 \geq 0$ and $\vec{q}_j^2 = -q_{j\perp}^2 \geq 0$.

In QMRK we have

$$\alpha \gg \beta_{q_1}, \quad q_1^2 = -\vec{q}_1^2 = t_1, \quad (\text{B.4})$$

$$\beta \gg \alpha_{q_2}, \quad q_2^2 = -\vec{q}_2^2 = t_2, \quad (\text{B.5})$$

$$\alpha_i \beta_i = \frac{m_i^2 + \vec{k}_i^2}{s}, \quad (\text{B.6})$$

where $i \in \{1, 2, W(Z)\}$, and m_i are the corresponding masses of outgoing particles. The invariants t_1 and t_2 describe the momentum transfer between the cluster formed by the quarks and the W (Z) boson on one hand and the incoming protons on the other hand. Due to the strong ordering in α and β one can neglect terms proportional to β_{q_1} and α_{q_2} in the calculation.

It is useful to introduce a set of Mandelstam variables describing the system

$$\hat{s} = (q_1 + q_2)^2 = \alpha\beta s - (\vec{q}_1 + \vec{q}_2)^2, \quad (\text{B.7a})$$

$$\hat{s}_1 = (k_1 + k_W)^2, \quad \hat{s}_2 = (k_2 + k_W)^2, \quad (\text{B.7b})$$

$$\hat{t}_1 = (q_1 - k_1)^2, \quad \hat{t}_2 = (q_2 - k_2)^2, \quad (\text{B.7c})$$

$$\hat{u}_1 = (q_1 - k_2)^2, \quad \hat{u}_2 = (q_2 - k_1)^2, \quad (\text{B.7d})$$

related by

$$\hat{u}_1 + \hat{t}_2 + \hat{s} = t_1 + t_2 + m_2^2 + \hat{s}_1, \quad \hat{u}_2 + \hat{t}_1 + \hat{s} = t_1 + t_2 + m_1^2 + \hat{s}_2. \quad (\text{B.8})$$

It is convenient to introduce transverse masses defined by

$$m_{i\perp} = \sqrt{m_i^2 + \vec{k}_i^2}, \quad m_{q\perp} = \sqrt{\hat{s} + (\vec{q}_1 + \vec{q}_2)^2}, \quad (\text{B.9})$$

and longitudinal momentum fractions of the produced particles $x_i = \frac{\alpha_i}{\alpha}$. Combining these relations with Eqs. (B.6, B.7) one finds that – in the end – the matrix element of W or Z production associated with a quark-antiquark pair can be expressed in terms of independent Mandelstam variables defined in Eqs. (B.7), transverse masses and variables $x_{1,2,W(Z)}$.

In the k_T -factorization formalism the hadronic and partonic cross section are related as follows:

$$d\sigma(pp \rightarrow q(W/Z)\bar{q}X) = \int \frac{d\alpha}{\alpha} \int d\vec{q}_1^2 \int \frac{d\phi_1}{2\pi} \mathcal{A}(\alpha, \vec{q}_1^2, \mu^2) \times \int \frac{d\beta}{\beta} \int d\vec{q}_2^2 \int \frac{d\phi_2}{2\pi} \mathcal{A}(\beta, \vec{q}_2^2, \mu^2) d\hat{\sigma}(g^*g^* \rightarrow q(W/Z)\bar{q}), \quad (\text{B.10})$$

where \mathcal{A} is the unintegrated gluon density in a proton and $\phi_{1,2}$ is the angle of $\vec{q}_{1,2}$ with respect to some fixed axis in the azimuthal plane. Argument μ^2 of unintegrated gluon densities is factorization scale. The partonic cross section is denoted by $d\hat{\sigma}$.

Since the incoming gluons of the matrix element entering this partonic cross section are off-shell, the calculation differs from that of a hard matrix element in the collinear approach significantly. To guarantee gauge invariance, the process with off-shell incoming particles has to be embedded into the scattering of on-shell particles. The extracted off-shell matrix element is of course independent of the specific choice of the particles in which the scattering process is embedded. Therefore, we replace the protons by quarks for the calculation of the hard matrix element. All diagrams for the discussed process are shown in Fig. B.2.

The first two rows of Fig. B.2 include also non-factorizing (‘non-resonant’) diagrams which factorize only in the sum. To make this factorization apparent already at this level, one can sum up the different diagrams of one gluon production in quark-quark scattering leading to one effective diagram with an effective vertex (see Fig. B.3). By working in Feynman gauge one obtains the well known Lipatov vertex [79]:

$$\Gamma_{\sigma\tau}^\nu(q_1, q_2) = \frac{2p_{A\tau}p_{B\sigma}}{s} \left(\frac{2t_1 + m_{q\perp}^2}{\beta s} p_A^\nu - \frac{2t_2 + m_{q\perp}^2}{\alpha s} p_B^\nu - (q_{1\perp} - q_{2\perp})^\nu \right). \quad (\text{B.11})$$

It can be shown that this vertex obeys the Ward identity. By this procedure, the first two rows of Fig. B.2 are each replaced by just one diagram.

Strong ordering of Mandelstam variables s and $t_{1,2}$ allows us to make a simplification of the coupling of gluons to incoming quarks. By neglecting the exchanged momentum in the vertex, we get an eikonal vertex which does not depend on the spin of the particle coupled to gluon and preserves its spin. In detail, it reads

$$-i\bar{u}(\lambda'_1, p_A - q_1)\gamma^\mu u(\lambda_1, p_A) \longrightarrow -2ip_A^\mu \delta_{\lambda'_1, \lambda_1}. \quad (\text{B.12})$$

With the help of Eq. (B.12) it is possible to remove the external quark lines and attach so-called ‘non-sense’ polarizations to the incoming gluons:

$$\epsilon_{q_1}^\mu = \frac{\sqrt{2}p_A^\mu}{\sqrt{s}}, \quad \epsilon_{q_2}^\nu = \frac{\sqrt{2}p_B^\nu}{\sqrt{s}}. \quad (\text{B.13})$$

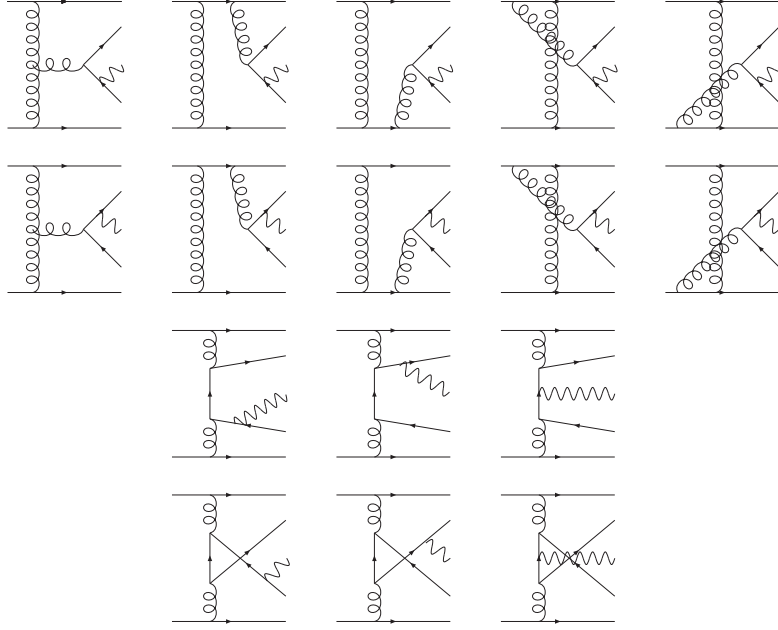


Figure B.2: Full set of diagrams contributing to W/Z production via off-shell gluon-gluon fusion.

Instead of Feynman gauge, one can choose an appropriate axial gauge [73] $n \cdot A = 0$ with the gauge vector

$$n^\mu = ap_A^\mu + bp_B^\mu \quad \text{with } a, b \in \mathbb{C}. \quad (\text{B.14})$$

The contraction of the eikonal coupling (B.12) with the gluon polarization tensor in this gauge

$$d_{\mu\nu}^{(n)}(q) = -g_{\mu\nu} + \frac{n_\mu q_\nu + q_\mu n_\nu}{nq} - n^2 \frac{q_\mu q_\nu}{(nq)^2} \quad (\text{B.15})$$

then reads

$$p_A^\mu d_{\mu\nu}^{(n)}(q_1) = \frac{q_{1\perp\nu}}{\alpha}, \quad p_B^\mu d_{\mu\nu}^{(n)}(q_2) = \frac{q_{2\perp\nu}}{\beta}. \quad (\text{B.16})$$

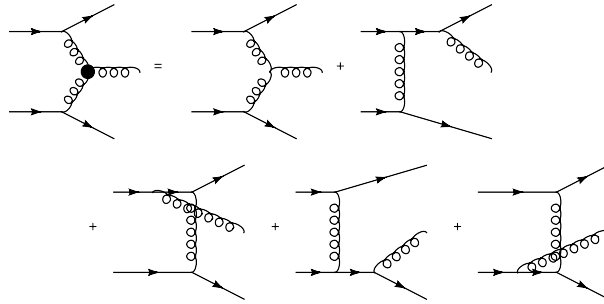


Figure B.3: Diagrams contributing to the Lipatov vertex.

In such a physical gauge the ‘non-resonant’ diagrams vanish since the direct connection of two eikonal couplings gives $p_A^\mu d_{\mu\nu}^{(n)} p_B^\nu = 0$ (in other words: the Lipatov vertex is to be replaced by the usual three gluon vertex).

In the case of heavy quark production the polarization sum for the s -channel gluon reduces to its Feynman gauge analogue $-g_{\mu\nu}$ due to the heavy flavor current conservation. The same simplification takes place in our calculation. Nevertheless, we have to stress that in general the polarization sum stays in its complex form. Of course, both ways to calculate the matrix element are equivalent due to gauge invariance.

The sum over the physical polarizations η of the W boson reads

$$\sum_{\eta} \epsilon^\mu(\eta, k_W) \epsilon^{*\nu}(\eta, k_W) = -g^{\mu\nu} + \frac{k_W^\mu k_W^\nu}{m_W^2}. \quad (\text{B.17})$$

It is equivalent to replace the polarization sum by

$$\sum_{\eta} \epsilon^\mu(\eta, k_W) \epsilon^{*\nu}(\eta, k_W) \rightarrow -g^{\mu\nu}, \quad (\text{B.18})$$

and to add also the contribution of the Goldstone boson emission diagrams, where the W boson is replaced by a Goldstone boson with mass m_W . This is in analogy of using the Feynman-t’Hooft gauge instead of the unitary gauge. We have calculated the squared matrix element in both ways as a crosscheck.

Expressions for the single diagrams in Fig. B.2 – where the first diagrams are already combined using the Lipatov vertex of Eq. (B.11) – are listed here (the hat marks contraction with Dirac-matrices):

$$\begin{aligned} \mathcal{M}_{1\mu\nu}^{ab} &= -ig_w g_s^2 K_{W/Z} \bar{u}[t^b, t^a] \frac{\hat{\Gamma}_{\mu\nu}(q_1, q_2)}{\hat{s}} \frac{-\hat{k}_2 - \hat{k}_W + m_1}{\hat{s}_2 - m_1^2} \hat{\epsilon}(v_q - a_q \gamma^5) v, \\ \mathcal{M}_{2\mu\nu}^{ab} &= -ig_w g_s^2 K_{W/Z} \bar{u} \hat{\epsilon}(v_q - a_q \gamma^5) \frac{\hat{k}_1 + \hat{k}_W + m_2}{\hat{s}_1 - m_2^2} [t^b, t^a] \frac{\hat{\Gamma}_{\mu\nu}(q_1, q_2)}{\hat{s}} v, \\ \mathcal{M}_{3\mu\nu}^{ab} &= -ig_w g_s^2 K_{W/Z} \bar{u} t^a \gamma_\mu \frac{\hat{k}_1 - \hat{q}_1 + m_1}{\hat{t}_1 - m_1^2} t^b \gamma_\nu \frac{-\hat{k}_2 - \hat{k}_W + m_1}{\hat{s}_2 - m_1^2} \hat{\epsilon}(v_q - a_q \gamma^5) v, \\ \mathcal{M}_{4\mu\nu}^{ab} &= -ig_w g_s^2 K_{W/Z} \bar{u} \hat{\epsilon}(v_q - a_q \gamma^5) \frac{\hat{k}_1 + \hat{k}_W + m_2}{\hat{s}_1 - m_2^2} t^a \gamma_\mu \frac{\hat{q}_2 - \hat{k}_2 + m_2}{\hat{t}_2 - m_2^2} t^b \gamma_\nu v, \\ \mathcal{M}_{5\mu\nu}^{ab} &= -ig_w g_s^2 K_{W/Z} \bar{u} t^a \gamma_\mu \frac{\hat{k}_1 - \hat{q}_1 + m_1}{\hat{t}_1 - m_1^2} \hat{\epsilon}(v_q - a_q \gamma^5) \frac{\hat{q}_2 - \hat{k}_2 + m_2}{\hat{t}_2 - m_2^2} t^b \gamma_\nu v, \\ \mathcal{M}_{6\mu\nu}^{ab} &= -ig_w g_s^2 K_{W/Z} \bar{u} \hat{\epsilon}(v_q - a_q \gamma^5) \frac{\hat{k}_1 + \hat{k}_W + m_2}{\hat{s}_1 - m_2^2} t^b \gamma_\nu \frac{\hat{q}_1 - \hat{k}_2 + m_2}{\hat{u}_1 - m_2^2} t^a \gamma_\mu v, \\ \mathcal{M}_{7\mu\nu}^{ab} &= -ig_w g_s^2 K_{W/Z} \bar{u} t^b \gamma_\nu \frac{\hat{k}_1 - \hat{q}_2 + m_1}{\hat{u}_2 - m_1^2} t^a \gamma_\mu \frac{-\hat{k}_2 - \hat{k}_W + m_1}{\hat{s}_2 - m_1^2} \hat{\epsilon}(v_q - a_q \gamma^5) v, \\ \mathcal{M}_{8\mu\nu}^{ab} &= -ig_w g_s^2 K_{W/Z} \bar{u} t^b \gamma_\nu \frac{\hat{k}_1 - \hat{q}_2 + m_1}{\hat{u}_2 - m_1^2} \hat{\epsilon}(v_q - a_q \gamma^5) \frac{\hat{q}_1 - \hat{k}_2 + m_2}{\hat{u}_1 - m_2^2} t^a \gamma_\mu v, \end{aligned} \quad (\text{B.19})$$

with the short hand notations $\bar{u} \equiv \bar{u}(\lambda, k_1)$, $v \equiv v(\lambda', k_2)$, $\hat{\epsilon} \equiv \hat{\epsilon}(\eta, k_W)$, and where η , λ and λ' label the helicity/ spins of the corresponding particles. Color factors are represented by Gell-Mann matrices t^a , t^b . The factors v_q , a_q and $K_{W/Z}$ encode the W and Z coupling. For W boson we have $v_q = a_q = 1$ and $K_W = V_{ud} \frac{1}{2\sqrt{2}}$, where V_{ud} is the corresponding element of Cabibbo-Kobayashi-Maskawa matrix. For Z we have $a_u = \frac{1}{2}$, $v_u = \frac{1}{2} - \frac{4}{3} \sin^2 \theta_W$ and $a_d = -\frac{1}{2}$, $v_d = -\frac{1}{2} + \frac{2}{3} \sin^2 \theta_W$ and $K_Z = \frac{1}{2 \cos \theta_W}$, where θ_W is the Weinberg angle. In the latter case m_1 equals m_2 , and m_W is replaced by m_Z .

If we make use of the Eq. (B.18) to replace the polarization sum, one has to add diagrams and corresponding amplitudes with Goldstone bosons with couplings

$$-ig_w K_{W/Z} \left(\frac{m_2 - m_1}{m_{W/Z}} v_q - \frac{m_1 + m_2}{m_{W/Z}} a_q \gamma^5 \right). \quad (\text{B.20})$$

Finally, the square of the amplitude averaged over initial helicities and colors of gluons and summed over spins/ helicities and colors of final particles can be written as

$$\frac{1}{4} \frac{1}{(N_c^2 - 1)^2} |\mathcal{M}|^2 = \frac{1}{4} \frac{1}{(N_c^2 - 1)^2} \sum_{\lambda, \lambda', \eta, a, b} \text{Tr}_{\text{color}} \left\{ \left| \sum_{i=1}^8 \epsilon_{q_1}^\mu \epsilon_{q_2}^\nu \mathcal{M}_{i\mu\nu}^{ab} \right|^2 \right\}. \quad (\text{B.21})$$

By evaluating the traces over the products of Gell-Mann color matrices, one encounters two possible cases of color factors

$$\text{Tr}\{t^a t^b t^a t^b\} = -\frac{1}{4} \frac{N_c^2 - 1}{N_c}, \quad \text{Tr}\{t^a t^b t^b t^a\} = \frac{1}{4} \frac{(N_c^2 - 1)^2}{N_c}, \quad (\text{B.22})$$

where $N_c = 3$ is the number of colors.

Finally, the expression for the partonic off-shell cross section appearing in Eq. (B.10) to calculate the hadronic cross section is

$$d\hat{\sigma}(g^* g^* \rightarrow q(W/Z) \bar{q}) = (2\pi)^4 \delta^{(4)}(q_1 + q_2 - k_1 - k_2 - k_{W/Z}) \times \\ \times \frac{1}{2\alpha\beta s} \frac{\alpha^2 \beta^2 s^2}{t_1 t_2} \frac{1}{4} \frac{1}{(N_c^2 - 1)^2} |\mathcal{M}|^2 \prod_{i \in \{1, 2, W\}} \frac{d^3 k_i}{(2\pi)^3 2E(k_i)}. \quad (\text{B.23})$$

The origin of the specific form of the flux factor and prefactor $\frac{\alpha^2 \beta^2 s^2}{t_1 t_2}$ is formulated in [73, 74]. We summarize the most relevant aspects here. An important feature of the whole calculation is that it is possible to recover the result obtained in collinear factorization by neglecting the transverse momenta of the gluons when they enter the hard matrix element and instead integrate over them only in the gluon densities. Due to factorization it is possible to keep this connection not only for the full cross section, but also for gluon densities and hard matrix element separately as well, provided that the explicit manifestations of the factorization formulae are phrased.

The key point is the observation that

$$\left\langle 2 \frac{q_{1\perp\mu} q_{1\perp\nu}}{q_{1\perp}^2} \right\rangle_{\phi_1} = -g_{\mu\nu}^\perp = \left\langle 2 \frac{q_{2\perp\mu} q_{2\perp\nu}}{q_{2\perp}^2} \right\rangle_{\phi_2}. \quad (\text{B.24})$$

As shown in Eqs. (B.14-B.16), in an appropriate gauge the polarization sum $\frac{2p_{A\mu}p_{B\nu}}{s}$ can be replaced by $\frac{2q_{1\perp\mu}q_{2\perp\nu}}{\alpha\beta s}$. Since in this gauge one has to deal with exactly the same diagrams as in the on-shell calculation, by dressing the off-shell matrix element squared with the prefactor $\frac{\alpha^2\beta^2s^2}{t_1t_2}$ and performing the averaging over azimuthal angles of the ‘incoming’ gluons, followed by taking the limit $t_1, t_2 \rightarrow 0$, one gets the collinear limit of the matrix element squared. The flux factor for off-shell gluons is defined as for on-shell gluons with $\frac{1}{2\alpha\beta s}$. As the matrix element is gauge invariant, this connection remains valid when one performs the current calculation in a different gauge.

Due to the off-shellness of the incoming gluons and the three particle final state the final result of the matrix element squared is rather lengthy. For that reason, we calculated it independently and in different ways. One calculation followed directly the derivation above using Feynman gauge for the gluons, and has been performed using MATHEMATICA. A second calculation written in FORM [80, 81] used an axial gauge as described above such that the Lipatov vertices in (B.19) are to be replaced by standard three-gluon-vertices. Moreover this second method used the method of orthogonal amplitudes, described in [70], which affects the fermionic part of the matrix element and with which one is able to treat the matrix element squared in a more compact way.

For this second method a few technical details are elaborated in the remainder of this section. The method of orthogonal amplitudes is based on expressing an generic amplitude $\widetilde{\mathcal{M}}$ (with one quark line) in terms of a set of four independent operators \hat{O}_i , $i \in \{1, \dots, 4\}$, which satisfy orthogonality relations $\text{Tr}\{\hat{O}_i(\hat{k}_2 - m_2)\overline{\hat{O}_j(\hat{k}_1 + m_1)}\} = \|\hat{O}_i\|^2\delta_{ij}$ for any possible i and j , where $\|\hat{O}_i\|$ is the ‘norm’ of the operator \hat{O}_i . The projection of $\widetilde{\mathcal{M}}$ by an operator \hat{O}_i is performed in the following way

$$\widetilde{\mathcal{M}}^i = \frac{1}{\|\hat{O}_i\|} \sum_{\lambda, \lambda'} \widetilde{\mathcal{M}} \bar{v}(\lambda', k_2) \overline{\hat{O}_i} u(\lambda, k_1). \quad (\text{B.25})$$

The matrix element squared then has the following form

$$\sum_{\lambda, \lambda'} |\widetilde{\mathcal{M}}|^2 = \sum_i |\widetilde{\mathcal{M}}^i|^2. \quad (\text{B.26})$$

In our case the matrix element consists of up to five Dirac-matrices (neglecting γ^5), after squaring one has to evaluate traces of up to twelve of them. In contrast the method of orthogonal amplitudes leads only to traces of up to eight Dirac-matrices.

If one wants to consider also the Z or W^\pm coupling in the Feynman diagram, one encounters a technical problem connected with the appearance of the Dirac-matrix γ^5 in the expression for the amplitude, leading to terms which include Levi-Civita tensors which later cancel. To avoid this complication, one can split the expression for the amplitude into two parts, one which does not include γ^5 and the other one which does (to separate the vector and axial part of the Z or W boson coupling). For the part with γ^5 one uses a base of operators $\hat{O}_i\gamma^5$. It is easy to check that they satisfy the same orthogonality relation like the operators \hat{O}_i . One also easily see that projections of amplitudes in which γ^5 occurs

do not contain terms with Levi-Civita tensors. In doing so, we extend the method of orthogonal amplitudes in a natural way.

Another complication comes from the presence of color factors in the expressions which are not numbers but matrices. To treat the projections as numbers, it is necessary to separate the Feynman diagrams into three groups according to different color factors, namely

$$\begin{aligned} C_1^{ab} &= t^a t^b - t^b t^a, \\ C_2^{ab} &= t^a t^b, \\ C_3^{ab} &= t^b t^a, \end{aligned} \tag{B.27}$$

which form a vector $C^{ab} = (C_1^{ab}, C_2^{ab}, C_3^{ab})$ (components of C^{ab} are color factors of $\mathcal{M}_{(1,2)\mu\nu}^{ab}$, $\mathcal{M}_{(3-5)\mu\nu}^{ab}$ and $\mathcal{M}_{(6-8)\mu\nu}^{ab}$ correspondingly). One can then build an corresponding vector containing the sums of Feynman diagrams without the color factors $\mathcal{F} = (\mathcal{F}_1, \mathcal{F}_2, \mathcal{F}_3)$ such that

$$\mathcal{M}^{ab} = (C^{ab})^T \mathcal{F}. \tag{B.28}$$

The Lorentz indices have been dropped for simplicity. Using the matrix

$$\mathcal{C}_{ij} = \text{Tr}\{C_i^{ab} C_j^{ba}\}, \tag{B.29}$$

the expression for the square of the matrix element takes the form

$$|\mathcal{M}|^2 = \mathcal{F}^\dagger \mathcal{C} \mathcal{F}, \tag{B.30}$$

where combinations of \mathcal{F}_i and \mathcal{F}_j^* are calculated using the projection method introduced in Eqs. (B.25, B.26). For the final simplification we have diagonalized the matrix \mathcal{C} . After diagonalization of the matrix \mathcal{C} only two diagonal elements remain nonzero. This is expected because the quarks in the final state, in this process, can occur only in two possible color states.

B.3 Numerical studies

The last missing pieces needed to calculate the hadronic cross section using Eq. (B.10), are the unintegrated gluon densities. As mentioned in the introduction, there are two equations suited to describe the evolution of an unintegrated gluon density, namely BFKL [17] and CCFM [25], respectively. Both have been shown to agree on the leading logarithms in small x [82], but the CCFM evolution is valid in the domain of larger x as well and, moreover, matches in this region with DGLAP. Therefore, we base our numerical studies on an unintegrated gluon density obeying the CCFM equation, which has been implemented in the Monte Carlo generator CASCADE [26]. We also investigate how the results change when using uPDFs generated by a different procedure known as KMR [46].

For this purpose, we implemented the matrix element squared as described above into CASCADE. This implementation will be available in the next version of CASCADE.

We have used the unintegrated parton distribution function (uPDF) CCFM 2003 set 3 for the numerical calculation.

To investigate the calculated matrix element as accurately as possible, we neglect in this first study the effect of hadronization of the final state. We study in detail rapidity and transverse momentum distributions of the produced gauge boson, quark and antiquark which (if one assumes that quarks approximately determine jets) are the most important observables in the experiment.

Furthermore, we compare the k_T -factorization approach to the collinear one. For this purpose, we compare the distributions obtained by our transverse momenta dependent matrix element with distributions obtained from the Monte Carlo generator MCFM [54] which provides a calculation of the same process in the collinear limit. In that case the transverse momenta coming from the evolution are neglected. We also investigate in Sec. B.3.3 how the variation of unintegrated parton densities affect the azimuthal angle and transverse momenta distributions.

As an artefact of the perturbative calculation, the results depend on the renormalization scale μ_R and the factorization scale μ_f . In the CCFM formalism the hardest scale is set by the emission angle of the hardest subcollision. It can be expressed in terms of the energy of the subcollision $\mu_f = \sqrt{\hat{s} + (\vec{q}_1 + \vec{q}_2)^2}$. For the comparison with collinear factorization calculations we have used as renormalization scale $\mu_R = m_Z$ in k_T -factorization calculation and in collinear calculation as well. We have also investigated other possible choices (see subsection B.3.3).

B.3.1 Comparison with LO collinear calculation

Our calculation of the hard matrix elements includes W^\pm and Z production in association with all possible quark-antiquark channels in gluon gluon fusion. Since the basic structure of all these matrix elements is very similar, we present results only for the typical case of $Zb\bar{b}$ production at LHC energies of $\sqrt{s} = 14\text{TeV}$. The mass of the b -quark used is $m_b = 4.62\text{ GeV}$. For the collinear factorization calculations we use the parton densities CTEQ6L1 [83].

The total cross sections are comparable in magnitude, though they differ considerably: 0.406 nb in k_T -factorization and 0.748 nb in collinear factorization. The difference of total cross sections stems from the different behavior at low transversal momenta of final state particles (discussed later in this section) where contributions from transversal momenta of the initial state gluons play a significant role. It can be seen that that applying a cut on the transversal momentum of the Z boson $p_{Z\perp} > 50\text{ GeV}$ the difference of the total cross sections becomes smaller. With this additional cut one obtains cross sections of 0.118 nb in k_T -factorization and 0.141 nb in LO collinear calculation.

The total cross sections for other final states of interest are given in Tab. B.1.

The transverse momentum and rapidity distributions of the vector boson are shown in Fig. B.4 and B.5, respectively. The comparison of the k_T -factorization approach to the collinear shows that they agree in transversal momentum distributions of Z at high values of this quantity. This is no surprise, since at high $p_{Z\perp}$ the contribution from initial state gluon transverse momenta is expected to become small.

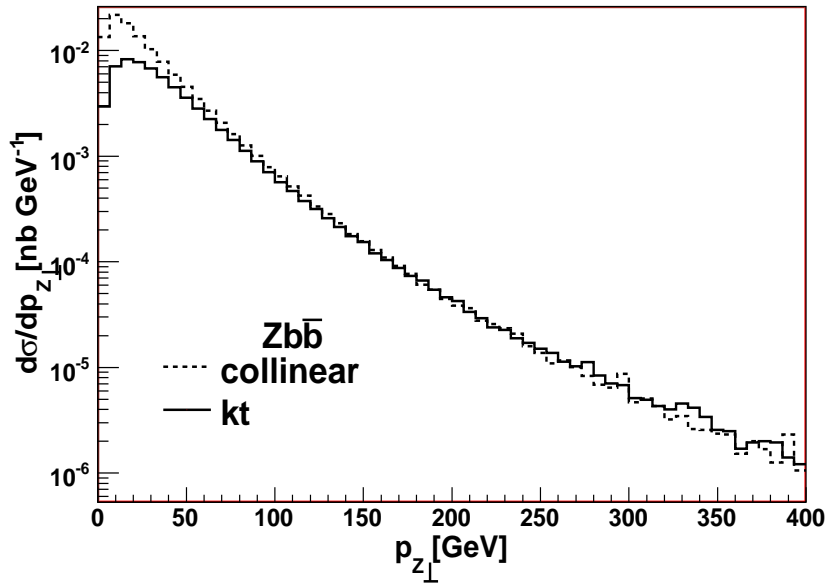


Figure B.4: Transverse momentum distributions of the produced Z gauge bosons. Calculation with massive b -quarks. Both calculations are in LO of perturbation series.

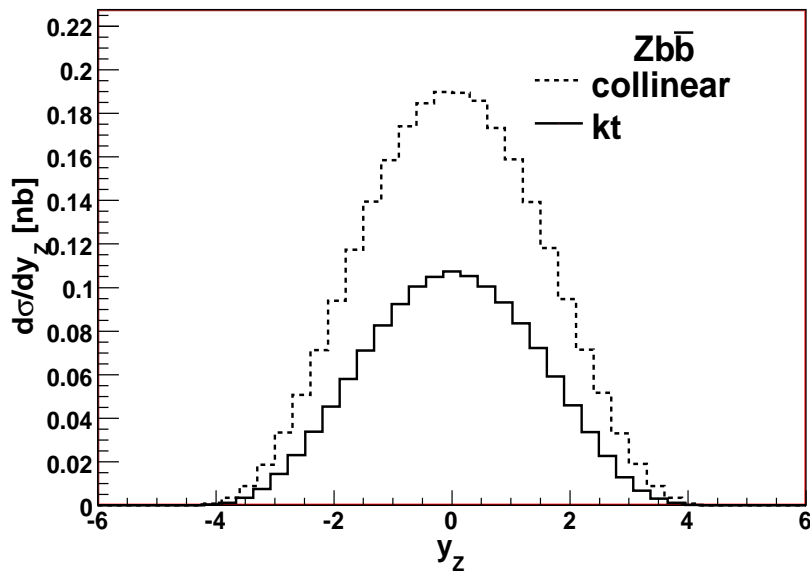


Figure B.5: Rapidity distribution of the produced Z gauge bosons. Calculation with massive b -quarks. Both calculations are in LO of perturbation series.

final state	$Zc\bar{c}$	$Zb\bar{b}$	$Zt\bar{t}$	$W^+s\bar{c}, W^-c\bar{s}$
σ_{tot} [nb]	0.430	0.406	$0.525 \cdot 10^{-3}$	1.92

Table B.1: Total cross sections for different final states, calculated in k_T -factorization using CASCADE.

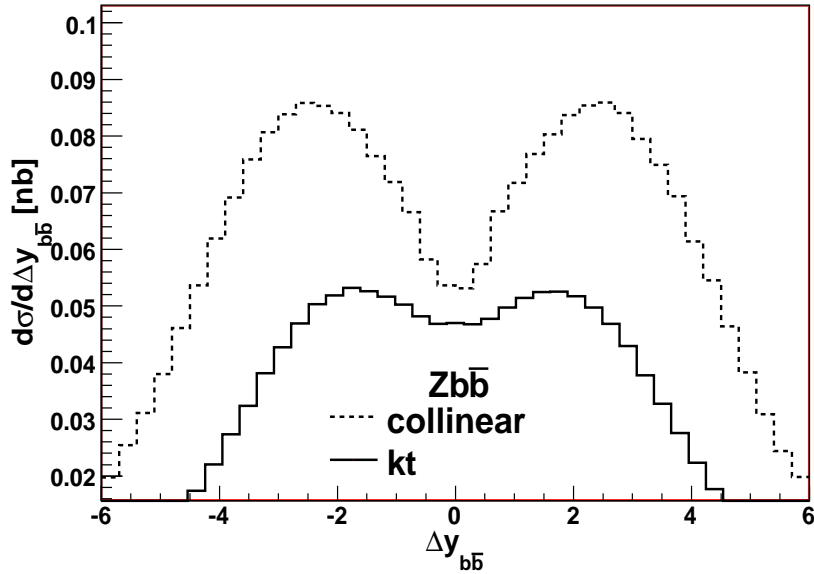


Figure B.6: Distributions of the rapidity distance between quark and antiquark. Calculation with massive b -quarks. Both calculations are in LO of perturbation series.

The rapidity distributions of the Z show a similar behavior, except for the overall normalization (Fig. B.5).

To elaborate the difference between k_T - and collinear factorization, we investigate more exclusive observables, like the cross section differential in rapidity distance between quark and antiquark (Fig. B.6). Both calculations show a two peak structure with a minimum at zero rapidity, but the k_T -factorization result has a considerably shallower minimum. The minimum in the case of NLO collinear calculation gets shallower – bringing together both calculations – when one again applies a cut on $p_{Z\perp} > 50$ GeV as one can see in Fig. B.7.

In the distribution of the azimuthal angular distance of Z and $\max(p_{b,\perp}, p_{\bar{b},\perp})$ (Fig. B.8) we observe that the region from 0 to $\pi/2$ is forbidden within the collinear calculation due to momentum conservation, which is not the case for k_T -factorization. This is caused by the contribution from initial state gluon transversal momentum which allows the transversal momenta of Z , b and \bar{b} to be unbalanced. A larger spread of possible configurations causes that the distribution in the k_T -factorization calculation flattens.

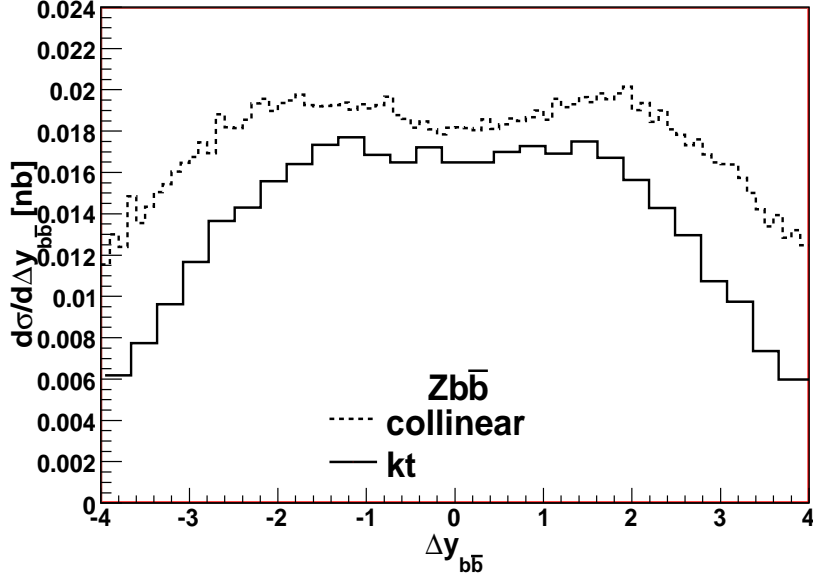


Figure B.7: Distributions of the rapidity distance between quark and antiquark. Calculation with massive b -quarks. A cut on $p_{Z\perp} > 50$ GeV has been applied.

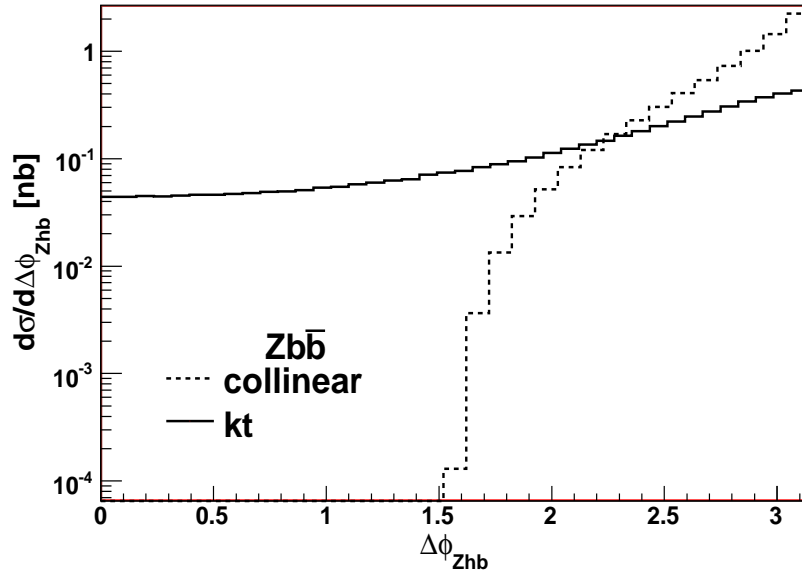


Figure B.8: Distributions of the distance in azimuthal angle of Z and highest p_{\perp} quark or antiquark. Calculation with massive b -quarks. Both calculations are in LO of perturbation series.

B.3.2 Comparison with NLO collinear calculation

In collinear factorization the physical effect of the intrinsic transverse momenta of the initial gluons can not be described until higher order corrections are taken into account. Then additional real emissions lead to off-shell gluons and their transverse momenta. Therefore, the significant differences between a calculation in the collinear factorization framework and k_T -factorization framework shown in the previous section encourage us to compare our LO calculation in k_T -factorization with a NLO collinear calculation, since CCFM evolution includes the high-energy part of the NLO collinear corrections. Since there are two off-shell initial gluons in a k_T -factorized pp -collision, one could even call for a higher order collinear calculation to compare².

To compare with a collinear NLO calculation, we use again the Monte Carlo generator MCFM. This Monte Carlo generator provides the process $gg \rightarrow Zb\bar{b}$ at NLO only in the massless quark limit. To avoid divergences, additional cuts are applied on transversal momenta of quarks, on the invariant mass of the $b\bar{b}$ pair, and on transversal momenta of a gluon which is produced in diagrams of real NLO corrections. Transversal momenta of produced quark, antiquark and gluon have to satisfy the condition $p_\perp > 4.62\text{GeV}$ (corresponding to the mass of the b -quark). These cuts on quark (antiquark) momenta are automatically applied in MCFM when one is performing a calculation involving massless quarks (antiquarks). We choose the parton density functions set CTEQ6M [83]. The same cuts on transversal momenta of quark and antiquark are then applied in CASCADE as well.

For the total cross sections, we obtain in the NLO collinear factorization calculation 1.04 nb, and in the k_T -factorization calculation 0.429 nb. The difference of the total cross sections in k_T -factorization calculation and the NLO calculation in collinear factorization is of the same origin as the difference between the total cross sections in section B.3.1 where comparison of k_T -factorization calculation and NLO calculation in collinear factorization is discussed. This is again illustrated by a cut on $p_{Z\perp} > 50\text{ GeV}$ diminishing the difference between the cross sections (0.125 nb for the k_T -factorization calculation and 0.165 nb for the NLO calculation in collinear factorization).

The result for the cross sections differential in the transversal momentum of Z can be seen in Fig. B.9. The cross section changes especially at small $p_{Z\perp}$ (see Fig. B.10) from LO to NLO calculation, and the difference between collinear calculation and k_T -factorization calculation becomes more pronounced. We observe that the maximum of the distribution in the NLO calculation (MCFM) stays approximately at same value of transversal momenta and the shape of the peak is very different from the one we obtain in k_T -factorization. Nevertheless, the $p_{Z\perp}$ distributions match at very high $p_{Z\perp}$ ($\mathcal{O}(10^2\text{GeV})$).

The rapidity distribution of the Z (Fig. B.11) shows no major difference in shape in k_T -factorization approach, LO and NLO collinear factorization approach.

²Although we argue that already the LO k_T -factorization calculation includes in some sense higher order corrections, one might ask for an extension to NLO. So far k_T -factorization based on CCFM evolution has been formulated only at LO. On the other hand, since the BFKL equation has been calculated at NLO accuracy [84], in the small x regime k_T -factorization can be formulated at NLO accuracy as well [24]. Nevertheless, an implementation into a Monte Carlo generator is still outstanding. Moreover, the calculation of an off-shell $2 \rightarrow 3$ process at one loop order is far beyond the scope of this work.

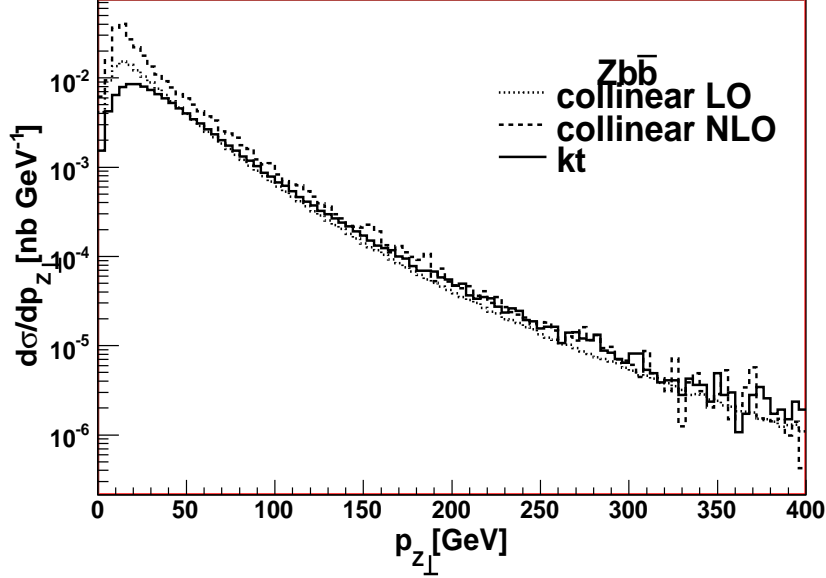


Figure B.9: Comparison of cross sections differential in transverse momentum of the produced Z gauge boson. Calculation with massless b -quarks. The applied cuts are described in the text.

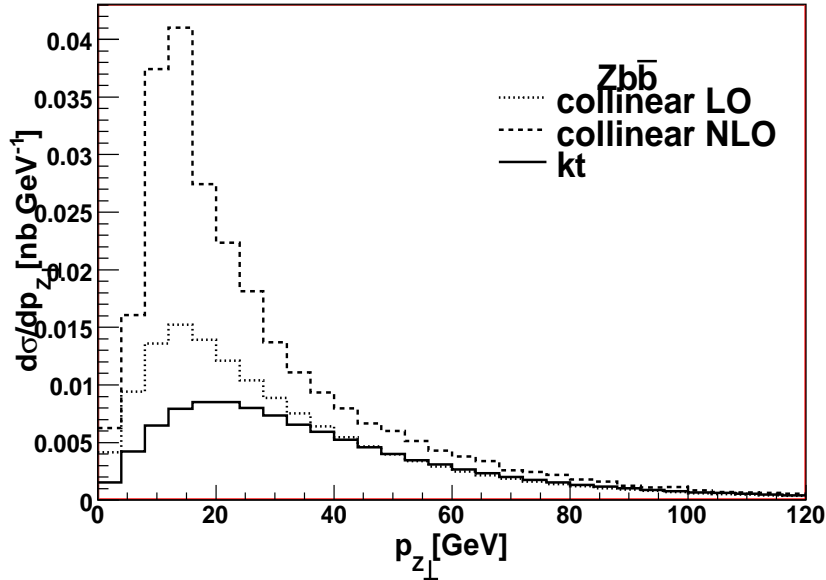


Figure B.10: Comparison of cross sections differential in transverse momentum of the produced Z gauge boson (linear scale). Calculation with massless b -quarks. The applied cuts are described in the text.

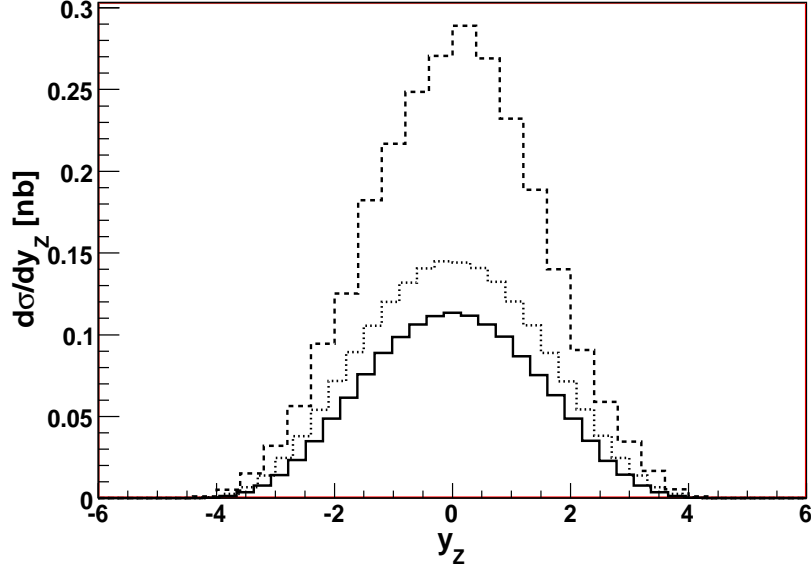


Figure B.11: Comparison of cross sections differential in rapidity of the produced Z gauge boson (logarithmic scale). Calculation with massless b -quarks. The applied cuts are described in the text.

We consider the cross section differential in the total transversal momentum of the $Zb\bar{b}$ system $p_{Zb\bar{b}\perp}$ in Fig. B.12. In the NLO collinear calculation a non-zero $p_{Zb\bar{b}\perp}$ is generated by the emission an additional gluon, while at LO it is always balanced to zero. At low $p_{Zb\bar{b}\perp}$ we see the consequence of the cut on the transverse momenta of the outgoing particles in MCFM (a small gap between 0 GeV and 4.62 GeV in $p_{Zb\bar{b}\perp}$ histogram). Since there are no parton showers or soft gluon re-summation [85] included in the MCFM NLO calculation, one observes a steep rise of the cross section towards zero transverse momentum because the matrix element diverges when approaching $p_{Zb\bar{b}\perp} \rightarrow 0$ GeV. On the other hand, uPDFs include corrections similar to parton shower effects, treated consistently, which causes the turnover in the cross section of the k_T -factorization calculation. Here, the entire transversal momentum of the $Zb\bar{b}$ system stems from the transversal momenta of initial state gluons. Interestingly, there is a difference not only at low values of $p_{Zb\bar{b}\perp}$, but also at high values of $p_{Zb\bar{b}\perp}$. Differential cross sections at high $p_{Zb\bar{b}\perp}$ have a similar slope, but differ by a factor of ~ 3 . This behavior contrasts with the behavior of distributions of $p_{Z\perp}$ in figures B.9 and B.4 where at large values of $p_{Z\perp}$ the differential cross sections overlap. However the behavior at small values of $p_{Zb\bar{b}\perp}$ in case of collinear calculation, as mentioned in the beginning of paragraph, is much different from the $p_{Z\perp}$. Because of the divergence we observe more events with low $p_{Zb\bar{b}\perp}$. Since the normalization for both distributions is the same, compensation of low $p_{Zb\bar{b}\perp}$ behavior in collinear factorization case causes difference at high $p_{Zb\bar{b}\perp}$ with kt -factorization, but doesn't change much the slope of the distribution. We

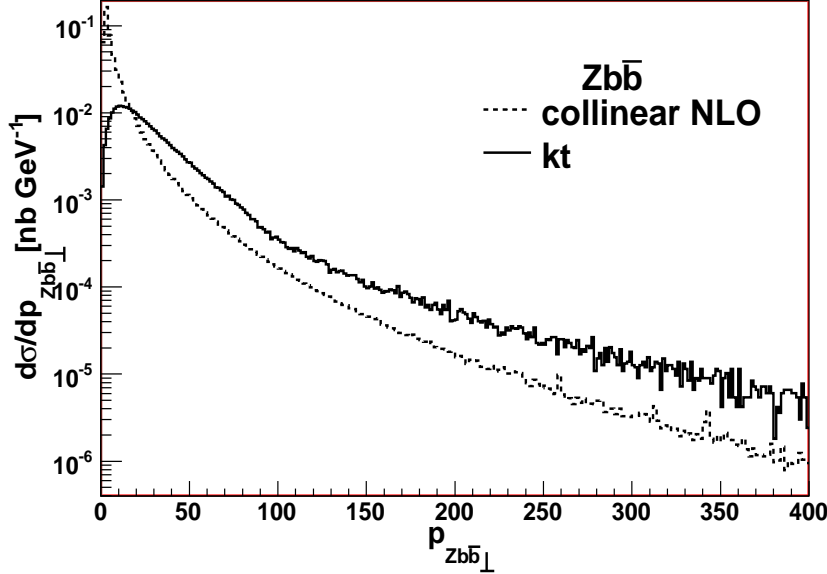


Figure B.12: Comparison of cross sections differential in the p_{\perp} of the system $Zb\bar{b}$. Calculation with massless b -quarks. The applied cuts are described in the text.

expect that resummation effects at low values of $p_{Zb\bar{b}\perp}$ would tame the growth of the cross section in collinear factorization and would decrease the difference with kt -factorization.

The cross sections differential in the difference of azimuthal angles of Z and b or \bar{b} quark with higher transversal momentum – $\Delta\phi_{Zhb}$ – is shown in Fig. B.13. Going from LO to NLO, the collinear calculation reveals a broader distribution like in the k_T -factorization case. Nevertheless, the k_T -factorization result shows a more homogeneous spread of the azimuthal angle distance. This difference originates partly in the difference of the transversal momentum distributions at low values (see Fig. B.10). A cut on low values ($p_{Z\perp} > 50$ GeV) of the transversal momentum of the Z boson results in steeper $\Delta\phi_{Zhb}$ distributions as shown in Fig. B.14. Still, the k_T -factorization result is flatter than the NLO collinear factorization calculation giving an indication that there is a contribution from the total transversal momentum of the $Zb\bar{b}$ system generated by both uPDFs.

B.3.3 Variation of the CASCADE results on uPDF and renormalization scale

To estimate the uncertainty coming from the different choices of uPDF sets, we calculate the cross sections differential in either the transverse momentum of the Z boson or $\Delta\phi_{Zhb}$ (distance in polar angle between Z and $\max(p_{b\perp}, p_{\bar{b}\perp})$) using different sets of uPDFs, namely CCFM J2003 set 1, 2, 3 [86] and CCFM set A0 [87], which are all obtained from fits to HERA F_2 data [88]. In addition we use the unintegrated parton density by [46], referred to as KMR. The resulting plots are shown in Figs. B.15 and B.16. We do not show the

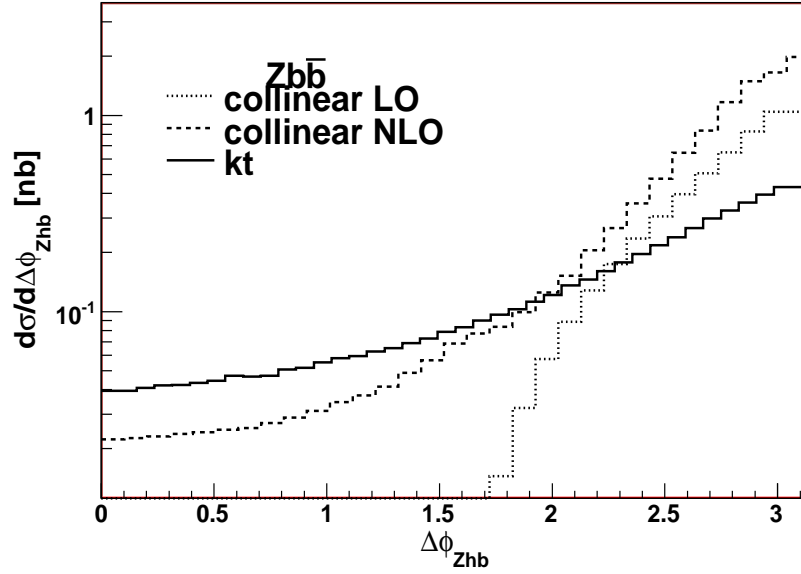


Figure B.13: Comparison of cross sections differential in distance in azimuthal angle of Z and higher $p_\perp b/\bar{b}$. Calculation with massless b -quarks. The applied cuts are described in the text.

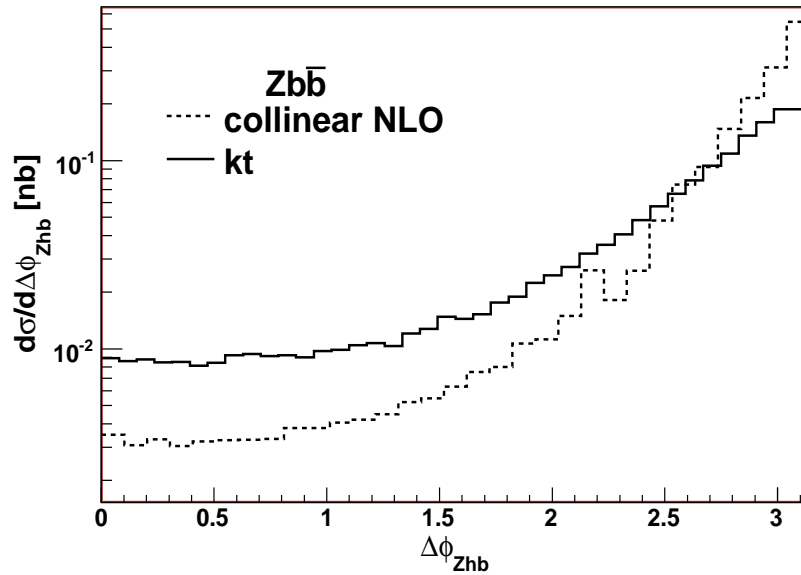


Figure B.14: Comparison of cross sections differential in distance in azimuthal angle of Z and higher $p_\perp b/\bar{b}$. Calculation with massless b -quarks. An additional cut on $p_{Z\perp} > 50$ GeV has been applied.

uPDF	Total cross section [nb]
CCFM J2003 set 1	0.369
CCFM J2003 set 2	0.147
CCFM J2003 set 3	0.406
CCFM set B0	0.277
CCFM set A0	0.378
KMR	0.190

Table B.2: Total cross sections of the process $pp \rightarrow Zb\bar{b} + X$ for different sets of unintegrated parton distribution functions.

μ_R	Total cross section [nb]
m_Z	0.406
$2m_Z$	0.392
$\frac{1}{2}m_Z$	0.607
$\sqrt{m_Z^2 + p_{Z\perp}^2}$	0.467
$2\sqrt{m_Z^2 + p_{Z\perp}^2}$	0.381
$\frac{1}{2}\sqrt{m_Z^2 + p_{Z\perp}^2}$	0.585

Table B.3: Total cross sections for different renormalization scale μ .

distributions for set 1, because they are very close to distribution for the set 3, to keep the plot clear.

The total cross sections obtained for different uPDFs can be seen in Tab. B.2. The total cross section varies for these different uPDFs about 45%, while the shape of the distributions is hardly effected except of the KMR. KMR set uses completely different evolution equations and a deviation is not surprising.

As a last point to discuss, we turn to the scale dependence. As already mentioned in the beginning of section B.3 the factorization scale is fixed by the emission angle of the hard subprocess. However, there is still freedom in choice of the renormalization scale which should be of order of the typical scale of the hard subprocess.

We consider two possible choices: the constant renormalization scale $\mu_1 = m_Z$ and the scale $\mu_2 = \sqrt{m_Z^2 + p_{Z\perp}^2}$, which are varied by factor of 2, so μ has values $2\mu_1$, $\frac{1}{2}\mu_1$ and $2\mu_2$, $\frac{1}{2}\mu_2$. The results for the $p_{Z\perp}$ and the $\Delta\phi_{Zhb}$ distribution can be seen in Figs. B.17 and B.18, respectively. The values of the cross section for individual choices of the scale are summarized in Tab. B.3. One can see that a running α_S does not affect the shape of the distributions, but only the total cross section.

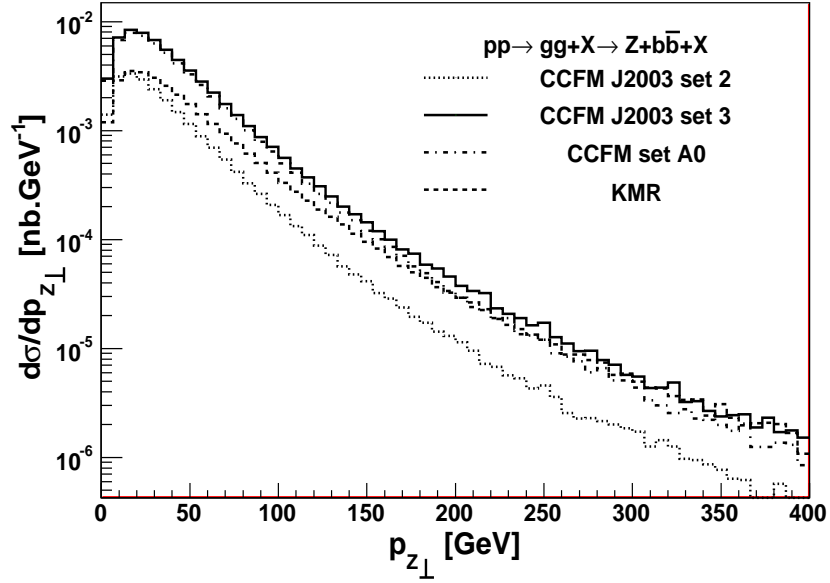


Figure B.15: Transverse momentum distributions of produced Z gauge boson calculated in CASCADE using massive quarks. Cases with different uPDFs compared.

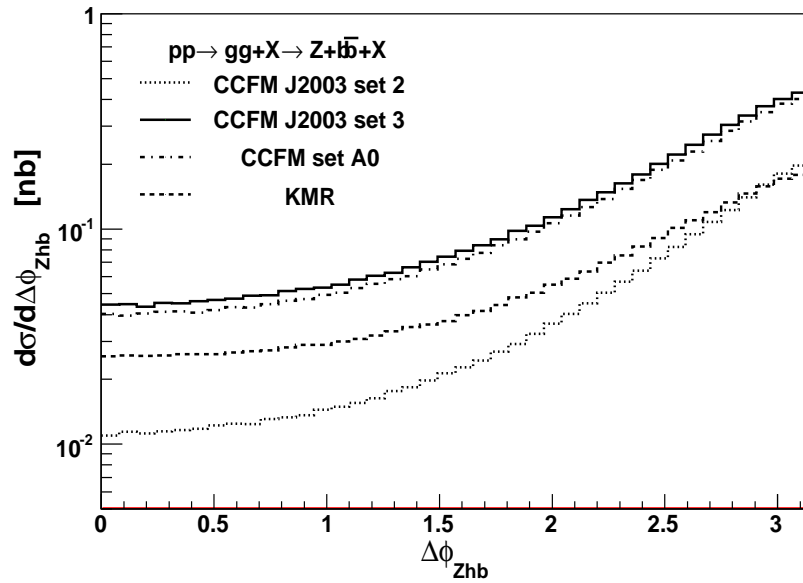


Figure B.16: Comparison of cross sections differential in distance in azimuthal angle of Z and higher $p_\perp b/\bar{b}$, using massive quarks. Cases with different uPDFs compared.

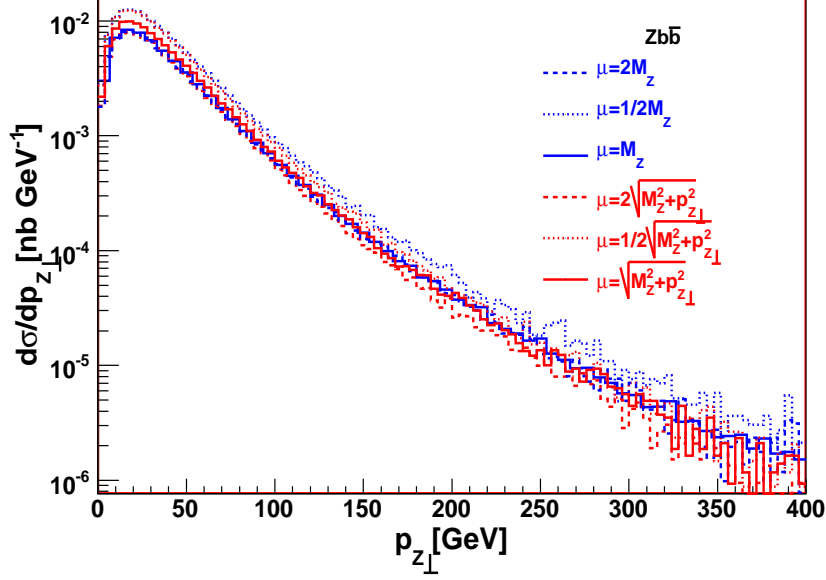


Figure B.17: Transverse momentum distributions of produced Z gauge boson calculated in CASCADE using massive quarks. Cases with different renormalization scales μ_R compared.

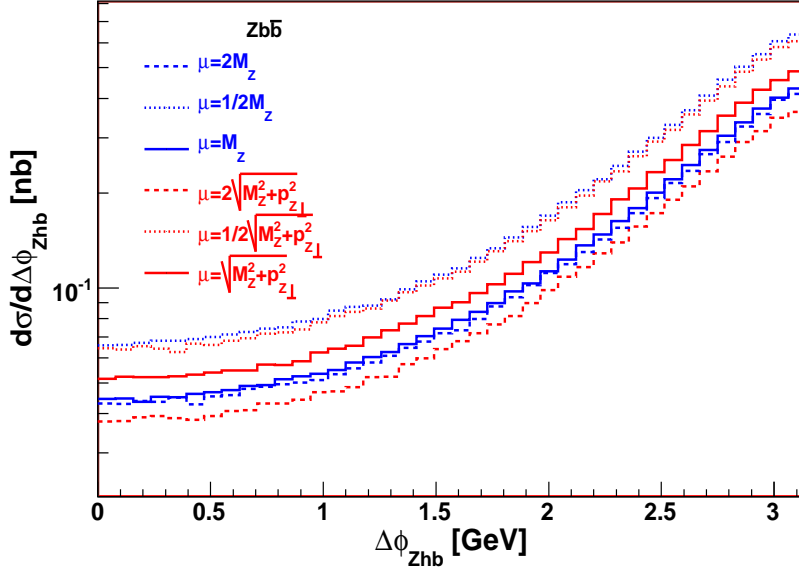


Figure B.18: Transverse momentum distributions of produced Z gauge boson calculated in CASCADE using massive quarks. Cases with different renormalization scales μ_R compared.

B.4 Summary and Conclusions

In this paper we have calculated the matrix element for the process $g^*g^* \rightarrow W/Zq_i\bar{q}_j$, taking into account the virtuality and transversal momenta of the initial gluons in the k_T -factorization formalism. We have implemented the matrix element squared in the Monte Carlo generator CASCADE and have calculated the total and differential cross sections of this process in proton proton collisions for the LHC at energy of $\sqrt{s} = 14\text{TeV}$. We have compared our results with results obtained in collinear factorization (using MCFM). The total cross sections differ by a factor of ~ 2 . There are differences in distributions which are sensitive to compensation of transversal momenta of particles in the final state coming from rather fundamental differences between the two approaches.

We found the most significant differences in the cross section differential in the azimuthal angle between the Z boson and higher p_T quark or antiquark – $\Delta\phi_{Zhb}$. While for a LO calculation in collinear factorization a region of values of $\Delta\phi_{Zhb}$ is kinematically forbidden, in k_T -factorization the whole range of $\Delta\phi_{Zhb}$ is allowed. This is because of neglecting the contribution of transversal momenta of initial state gluons in calculation of matrix element in collinear factorization. The NLO collinear calculation (where transversal momentum is generated by real corrections) shows already the same qualitative behavior as the k_T -factorization calculation. However, there remains a difference in the shape of the distribution of $\Delta\phi_{Zhb}$ compared to the k_T -factorization calculation. We also compared cross sections differential in the transversal momentum of the $Zb\bar{b}$ system – $p_{Zb\bar{b}\perp}$. In collinear factorization and lowest order perturbation theory (α_S^2), the observable $p_{Zb\bar{b}\perp}$ is exactly zero. For a non-zero contribution in collinear factorization higher order corrections are needed. The k_T -factorization gives non-zero contribution already at α_S^2 order. We have compared cross sections differential in $p_{Zb\bar{b}\perp}$ calculated in NLO in collinear calculation and LO in k_T -factorization. The distributions have different shape at low values of $p_{Zb\bar{b}\perp}$. At high values of $p_{Zb\bar{b}\perp}$ there is a difference in magnitude, but the slopes don't differ much. We expect that collinear factorization result with included resummation effects for low $p_{Zb\bar{b}\perp}$ would approach the one of k_T -factorization.

We have calculated the cross sections differential in the transversal momentum of the produced boson. The maximum of the distribution in the k_T -factorization calculation is at higher transversal momenta compared to the collinear one. This shows the sensitivity of this distribution on parton evolution model and treatment of kinematics.

We conclude that in some of the effects of NLO and even higher order collinear calculation are already included in the LO k_T -factorization calculation.

Acknowledgments

First of all, we would like to thank H. Jung and J. Bartels for their help, advice, and support during all stages of this work. We would like to express special thanks to S. P. Baranov for useful advice and introduction to method of orthogonal amplitudes, which was crucial to obtain numerically stable results. We are thankful to J. Campbell for help with filling of histograms in Monte Carlo generator MCFM. We also benefited from interesting discussions with A. Bacchetta. F.S. has been supported in part by the

Deutsche Forschungsgemeinschaft, DFG Grant No. GRK 602, and the Agence Nationale de la Recherche (France), contract No ANR-06-JCJC-0084-02. This work is associated with the DFG Collaborative Research Centre SFB 676.

C Forward Jet Production at the Large Hadron Collider

DESY-09-119
OUTP-09-15-P

Forward Jet Production at the Large Hadron Collider

M. Deak¹, F. Hautmann², H. Jung¹, K. Kutak¹

¹*Deutsches Elektronen Synchrotron, D-22603 Hamburg,*

²*Theoretical Physics, University of Oxford, Oxford OX1 3NP*

Abstract

At the Large Hadron Collider (LHC) it will become possible for the first time to investigate experimentally the forward region in hadron-hadron collisions via high- p_T processes. In the LHC forward kinematics QCD logarithmic corrections in the hard transverse momentum and in the large rapidity interval may both be quantitatively significant. We analyze the hadroproduction of forward jets in the framework of QCD high-energy factorization, which allows one to resum consistently both kinds of corrections to higher orders in QCD perturbation theory. We compute the short-distance matrix elements needed to evaluate the factorization formula at fully exclusive level. We discuss numerically dynamical features of multi-gluon emission at large angle encoded in the factorizing high-energy amplitudes.

C.1 Introduction

Experiments at the Large Hadron Collider (LHC) will explore the region of large rapidities both with general-purpose detectors and with dedicated instrumentation, including forward calorimeters and proton taggers [61–64, 89–91]. The forward-physics program involves a wide range of topics, from new particle discovery processes [89, 92, 93] to new aspects of strong interaction physics [91, 94, 95] to heavy-ion collisions [96, 97]. Owing to the large center-of-mass energy and the unprecedented experimental coverage at large rapidities, it becomes possible for the first time to investigate the forward region with high- p_T probes.

The hadroproduction of a forward jet associated with a hard final state X is pictured in Fig. C.1. The kinematics of the process is characterized by the large ratio of sub-energies $s_1/s \gg 1$ and highly asymmetric longitudinal momenta in the partonic initial state, $k_1 \cdot p_2 \gg k_2 \cdot p_1$. At the LHC the use of forward calorimeters allows one to measure events where jet transverse momenta $p_T > 20$ GeV are produced several units of rapidity apart, $\Delta y \gtrsim 4 \div 6$ [61, 64, 91]. Working at polar angles that are small but sufficiently far from the beam axis not to be affected by beam remnants, one measures azimuthal plane correlations between high- p_T events widely separated in rapidity (Fig. C.2).

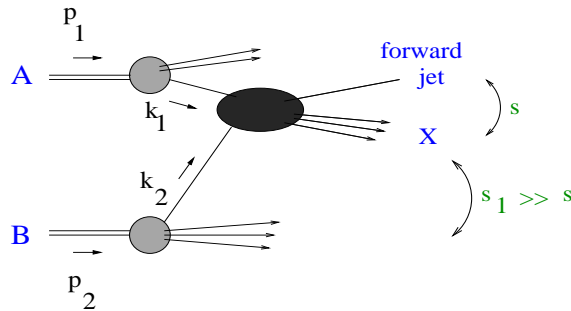


Figure C.1: Jet production in the forward rapidity region in hadron-hadron collisions.

The presence of multiple large-momentum scales implies that, as was recognized in [67–69], reliable theoretical predictions for forward jets can only be obtained after summing logarithmic QCD corrections at high energy to all orders in α_s . This has motivated efforts [22, 98–100] to construct new algorithms for Monte Carlo event generators capable of describing jet production beyond the central rapidity region. Note that an analogous observation applies to forward jets associated to deeply inelastic scattering [101, 102]. Indeed, measurements of forward jet cross subsections at HERA [56] indicate that neither fixed-order next-to-leading calculations nor standard shower Monte Carlo generators [56, 98, 103], e.g. PYTHIA or HERWIG, are able to describe forward jet ep data. Improved methods to evaluate QCD predictions are needed to treat the multi-scale region implied by the forward kinematics.

In this work we move on from the observation that realistic phenomenology in the LHC forward region will require taking into account at higher order both logarithmic corrections in the large rapidity interval (of high-energy type) and logarithmic corrections in the hard transverse momentum (of collinear type). The theoretical framework to resum consistently

both kinds of logarithmic corrections in QCD perturbation theory is based on high-energy factorization at fixed transverse momentum [104].



Figure C.2: (Left) High- p_T events in the forward and central detectors; (right) azimuthal plane segmentation.

This formulation depends on unintegrated distributions for parton splitting, obeying appropriate evolution equations, and short-distance, process-dependent matrix elements. The unintegrated-level evolution is given by evolution equations in rapidity, or angle, parameters. Different forms of the evolution, valid in different kinematic regions, are available. See [105–108], and references therein, for recent work in this area and reviews. The short-distance matrix elements, needed in the evaluation of the factorization formula, are the subject of this paper. We obtain their explicit expressions in a fully exclusive form, including all partonic channels, and present results of numerically integrating them over final states. Such matrix elements, though not on shell, are gauge invariant and perturbatively calculable. They factorize in the high energy limit in front of (unintegrated) distributions for parton splitting not only in the collinear emission region but also at finite angle. In particular, they can serve to take into account effects of coherence from multi-gluon emission, away from small angles, which become important for correlations among jets across long separations in rapidity. We give a numerical illustration of the high- k_T behavior resulting from such finite-angle radiation.

On one hand, once convoluted with the small- x gluon Green’s function according to the method [104, 109], these matrix elements control the summation of high-energy logarithmic corrections, contributing both to the next-to-leading-order BFKL kernel [84] and to the jet impact factors [110, 111]. On the other hand, they can be used in a shower Monte Carlo implementing parton-branching kernels at unintegrated level (see e.g. [11, 112] for recent works) to generate fully exclusive events. We leave these applications to a separate paper.

The paper is organized as follows. After recalling the factorized form of the cross subsections in Sec. C.2, we present the high-energy amplitudes in Sec. C.3, and discuss basic properties and numerical results in Sec. C.4. We summarize in Sec. C.5.

C.2 High-energy factorized cross subsections

High-energy factorization [104] allows one to decompose the cross subsection for the process of Fig. C.1 into partonic distributions (in general, unintegrated) and hard-scattering kernels, obtained via the high-energy projectors [104, 109] from the amplitudes for the process $p_1 + p_2 \rightarrow p_3 + p_4 + 2$ massless partons. The basic structure is depicted in Fig. C.3.

With reference to the notation of Fig. C.3, let us work in the center of mass frame of the incoming momenta

$$p_1 = \sqrt{S/2}(1, 0, 0_T) \quad , \quad p_2 = \sqrt{S/2}(0, 1, 0_T) \quad , \quad 2p_1 \cdot p_2 = S \quad , \quad (\text{C.1})$$

where, for any four-vector, $p^\mu = (p^+, p^-, p_T)$, with $p^\pm = (p^0 \pm p^3)/\sqrt{2}$ and p_T two-dimensional euclidean vector. Let us parameterize the exchanged momenta in terms of purely transverse four-vectors k_\perp and $k_{\perp 1}$ and longitudinal momentum fractions ξ_i and $\bar{\xi}_i$ as

$$p_1 - p_5 = k_1 = \xi_1 p_1 + k_{\perp 1} + \bar{\xi}_1 p_2 \quad , \quad p_2 - p_6 = k_2 = \xi_2 p_2 + k_\perp + \bar{\xi}_2 p_1 \quad . \quad (\text{C.2})$$

For high energies we can introduce strong ordering in the longitudinal momenta, $\xi_1 \gg |\bar{\xi}_2|$, $\xi_2 \gg |\bar{\xi}_1|$. Further, we make the forward region approximations $(p_4 + p_6)^2 \gg (p_3 + p_5)^2$, $k_1 \simeq \xi_1 p_1$, $k_2 \simeq \xi_2 p_2 + k_\perp$, so that

$$p_5 \simeq (1 - \xi_1)p_1 \quad , \quad p_6 \simeq (1 - \xi_2)p_2 - k_\perp \quad , \quad \xi_1 \gg \xi_2 \quad . \quad (\text{C.3})$$

It is convenient to define the rapidity-weighted average of dijet transverse momenta,

$$Q_T = (1 - \nu)p_{T4} - \nu p_{T3} \quad , \quad \text{where } \nu = (p_2 p_4)/[(p_2 p_1) - (p_2 p_5)] \quad , \quad (\text{C.4})$$

and the azimuthal angle

$$\cos \varphi = Q_T \cdot k_T / |Q_T| |k_T| \quad . \quad (\text{C.5})$$

We consider the differential jet cross subsection in Q_T and φ .



Figure C.3: (a) Factorized structure of the cross subsection; (b) a graph contributing to the qg channel matrix element.

According to the factorization [104, 110], the jet cross subsection can be computed as (Fig. C.3a)

$$\frac{d\sigma}{dQ_T^2 d\varphi} = \sum_a \int d\xi_1 d\xi_2 d^2 k_T \phi_{a/A}(\xi_1) \frac{d\hat{\sigma}}{dQ_T^2 d\varphi}(\xi_1 \xi_2 S, k_T, Q_T, \varphi) \phi_{g^*/B}(\xi_2, k_T) \quad , \quad (\text{C.6})$$

where the sum goes over parton species, ϕ are the parton distributions defined from the unintegrated Green's functions introduced in [109] for both gluon and quark cases, and $\hat{\sigma}$ is

the hard cross subsection, calculable from the high-energy limit of perturbative amplitudes (Fig. C.3b).

The physical picture underlying Eq. (C.6) is based on the fact that initial-state parton configurations contributing to forward production are asymmetric, with the parton in the top subgraph being probed near the mass shell and large x , while the parton in the bottom subgraph is off-shell and small- x . Eq. (C.6) embodies this picture through the longitudinal and transverse momentum dependences of both ϕ and $\hat{\sigma}$.

For phenomenological studies we will be interested in coupling Eq. (C.6) to parton showers to achieve a full description of the associated final states. To this end we need the matrix elements defining the hard-scattering kernels in a fully exclusive form. We give the results in the next subsection.

C.3 Matrix elements for fully exclusive events

The matrix elements determining the hard-scattering kernels $\hat{\sigma}$ can be viewed as a suitably defined off-shell continuation of scattering amplitudes at lower order [104]. They can be obtained by applying to scattering amplitudes \mathcal{M} the high-energy eikonal projectors [104, 109],

$$\mathcal{M}^H = P_{(eik)}^H{}^{\mu_1\mu_2\dots} \mathcal{M}_{\mu_1\mu_2\dots}(k_1, k_2, \{p_i\}) \quad , \quad P_{(eik)}^H{}^{\mu_1\mu_2\dots} \propto \frac{2k_{\perp 1}^{\mu_1} k_{\perp 2}^{\mu_2}}{\sqrt{k_{\perp 1}^2 k_{\perp 2}^2}} \quad . \quad (\text{C.7})$$

Although they are not evaluated on shell, they are gauge invariant and their expressions are simple. The utility of these matrix elements is that in the high-energy limit they factorize not only in the collinear emission region but also in the large-angle emission region. As long as the factorization is carried out in terms of distributions for parton splitting at fixed transverse momentum, as in Eq. (C.6), they can be useful to include coherence effects [110] from multi-gluon emission across large rapidity intervals, not associated with small angles.

The results for the matrix elements in exclusive form are given by

$$\mathcal{M}_{qg \rightarrow qg} = C_1 \mathcal{A}_1^{(ab)} + \bar{C}_1 \mathcal{A}_1^{(nab)} \quad , \quad \mathcal{M}_{gg \rightarrow q\bar{q}} = C_2 \mathcal{A}_2^{(ab)} + \bar{C}_2 \mathcal{A}_2^{(nab)} \quad , \quad \mathcal{M}_{gg \rightarrow gg} = C_3 \mathcal{A}_3 \quad (\text{C.8})$$

where

$$\mathcal{A}_1^{(ab)} = \left(\frac{k_1 k_2}{k_1 p_2} \right)^2 \frac{(k_1 p_2)^2 + (p_2 p_3)^2}{(k_1 p_4) (p_3 p_4)} \quad , \quad (\text{C.9})$$

$$\mathcal{A}_1^{(nab)} = \left(\frac{k_1 k_2}{k_1 p_2} \right)^2 \frac{(k_1 p_2)^2 + (p_2 p_3)^2}{(k_1 p_4) (p_3 p_4)} \left(\frac{(p_3 p_4) (k_1 p_2)}{(k_1 p_3) (p_2 p_4)} + \frac{(k_1 p_4) (p_2 p_3)}{(k_1 p_3) (p_2 p_4)} - 1 \right) \quad , \quad (\text{C.10})$$

$$\mathcal{A}_2^{(ab)} = \left(\frac{k_1 k_2}{k_1 p_2} \right)^2 \frac{(p_2 p_3)^2 + (p_2 p_4)^2}{(k_1 p_4) (k_1 p_3)} \quad , \quad (\text{C.11})$$

$$\mathcal{A}_2^{(nab)} = \left(\frac{k_1 k_2}{k_1 p_2} \right)^2 \frac{(p_2 p_3)^2 + (p_2 p_4)^2}{(k_1 p_4) (k_1 p_3)} \left(\frac{(k_1 p_4) (p_2 p_3)}{(p_3 p_4) (k_1 p_2)} + \frac{(k_1 p_3) (p_2 p_4)}{(p_3 p_4) (k_1 p_2)} - 1 \right) \quad , \quad (\text{C.12})$$

$$\mathcal{A}_3 = \left(\frac{k_1 k_2}{k_1 p_2} \right)^2 \frac{(p_3 p_4)(k_1 p_2) + (k_1 p_4)(p_2 p_3) + (p_2 p_4)(k_1 p_3)}{(p_2 p_4)(k_1 p_4)(p_3 p_4)(k_1 p_2)(p_2 p_3)(k_1 p_3)} [(p_2 p_4)^4 + (k_1 p_2)^4 + (p_2 p_3)^4] \quad , \quad (\text{C.13})$$

and $C_1 = g^4(N_c^2 - 1)/(4N_c^2)$, $\overline{C}_1 = C_1 C_A/(2C_F)$, $C_2 = g^4/(2N_c)$, $\overline{C}_2 = C_2 C_A/(2C_F)$, $C_3 = g^4 N_c^2/(N_c^2 - 1)$.

The results above contain the dependence on the transverse momentum k_\perp along the parton lines that connect the hard scatter to the parton distributions. Nevertheless, they are short-distance in the sense that they can be safely integrated down to $k_\perp = 0$. That is, the high-energy projection is designed so that all infrared contributions are factored out in the nonperturbative Green's functions ϕ in Eq. (C.6). An explicit numerical illustration is given in the next subsection.³

The role of Eqs. (C.9)-(C.13) is twofold. On one hand, they give the high-energy limit of multi-parton matrix elements in the forward region, which may be of direct phenomenological significance. On the other hand, because of the factorization theorem [104], logarithmically enhanced corrections for large rapidity can be systematically obtained to all orders in α_s from those in the (unintegrated) distributions for parton splitting once the hard scattering functions are known at finite k_\perp . To this end the detailed form of the fall-off at large $|k_\perp|^2$ is relevant.

In the next subsection we discuss the behavior at high transverse momentum numerically. This behavior reflects properties of gluon emission at large angle encoded in the high-energy amplitudes. These are relevant, along with large-angle effects in the Sudakov region (see e.g. [114]), to achieve a full treatment of gluon coherence effects [115] capable of describing jet final states across the whole rapidity phase space. A uniform treatment of the high-energy and Sudakov regions is still an open issue [27] of interest for parton-shower implementations.

C.4 Numerical results

We now partially integrate the amplitudes over final states. We work at the level of hard scattering matrix elements, leaving the treatment of parton evolution by showering to a separate study [116]. We concentrate on the region of hard emissions, where jets are well separated. Regions near the boundary of the angular phase space are sensitive to infrared radiation and can be addressed within a full parton-shower description of the process.

We consider the differential distribution in the transverse variable Q_T and azimuthal angle φ . The variable Q_T describes the imbalance in transverse momentum between the hardest jets, weighted by ν , according to Eq. (C.4). In Figs. C.4 and C.5 we show numerical results versus transverse momentum and versus energy (qg channel).

The curves in Fig. C.4 measure the k_T distribution of the jet system recoiling against the leading di-jets. The result at $k_T/Q_T \rightarrow 0$ in these plots returns the lowest-order result,

³Although the hard-scattering functions constructed from the amplitudes in Eqs. (C.9)-(C.13) are not coefficient functions in the conventional sense of the operator product expansion, they can be related to such objects, for inclusive variables, along the lines e.g. of [109]. They could be interpreted in terms of coefficient functions in the sense of the high-energy OPE of [113].

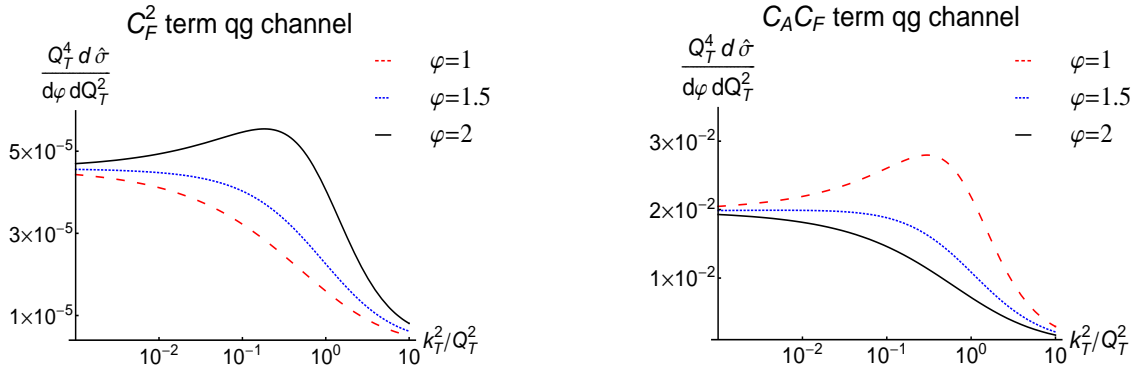


Figure C.4: The k_T/Q_T dependence of the factorizing qg hard cross subsection at high energy: (left) C_F^2 term; (right) $C_F C_A$ term ($\xi_1 \xi_2 S/Q_T^2 = 10^2$, $\alpha_s = 0.2$).

i.e., the leading-order process with two back-to-back jets,

$$\frac{d\hat{\sigma}}{dQ_T^2 d\varphi} \rightarrow \alpha_s^2 f^{(0)}(p_T^2/s) , \quad Q_T \rightarrow p_T = |p_{T3}| = |p_{T4}| , \quad (\text{C.14})$$

where $s = (p_3 + p_4)^2$, and $f^{(0)}$ is given by

$$f^{(0)}(z) = \frac{1}{16\sqrt{1-4z}} [C_F^2 z(1+z) + 2C_F C_A(1-3z+z^2)] . \quad (\text{C.15})$$

The dependence on k_T and φ plotted in Fig. C.4 is the result of higher-order gluon radiation, treated according to the high-energy asymptotics. The different behaviors in φ for the C_F^2 and $C_A C_F$ terms reflect the fact that the former comes from the insertion of gluons on fermion-exchange amplitude while the latter comes from the insertion of gluons on vector-exchange amplitude.

Fig. C.5 shows the energy dependence for fixed k_T/Q_T . The constant asymptotic behavior at large s due to color-octet spin-1 exchange distinguishes the $C_F C_A$ term from the C_F^2 term. The dependence on the azimuthal angle in Figs. C.4 and C.5 is relevant, especially because forward jet measurements will rely on azimuthal plane correlations between jets far apart in rapidity (Fig.C.2).

While Eq. (C.15) gives the collinear emission limit, we see from Fig. C.4 that multi-gluon radiation at finite angles sets a dynamical cut-off at values of k_T of order Q_T ,

$$k_T \lesssim \mu = c Q_T . \quad (\text{C.16})$$

The physical meaning of this result is that the summation of the higher-order logarithmic corrections for large $y \sim \ln s/p_T^2$ is precisely determined [104, 110] by convoluting the unintegrated splitting functions over the k_T -dependence in Fig. C.4, via the distributional relation

$$\int d^2 k_T \left(\frac{1}{k_T^2} \right)_+ \hat{\sigma}(k_T) = \int d^2 k_T \frac{1}{k_T^2} [\hat{\sigma}(k_T) - \Theta(\mu - k_T) \hat{\sigma}(0_T)] . \quad (\text{C.17})$$

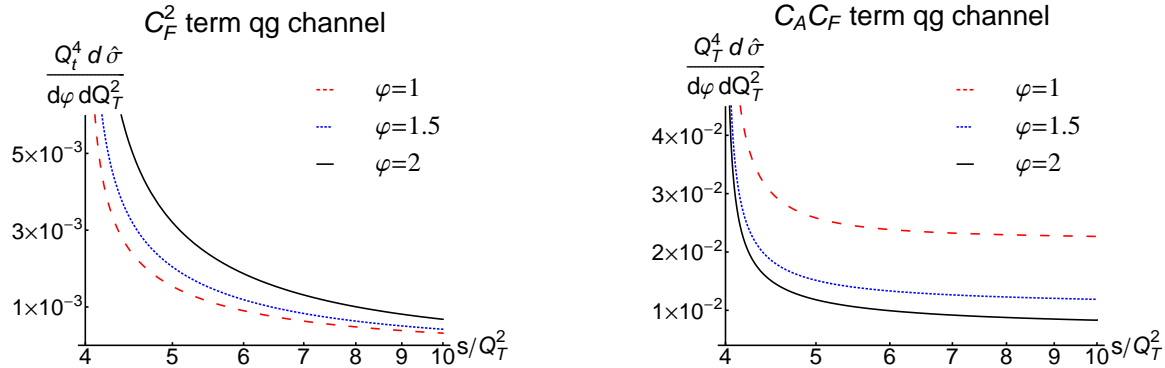


Figure C.5: The energy dependence of the qq hard cross subsection ($k_T/Q_T = 1$).

So the results in Fig. C.4 illustrate quantitatively the significance of contributions with $k_T \simeq Q_T$ in the large- y region. Non-negligible effects arise at high energy from the finite- k_T tail. These effects are not included in collinear-branching generators (and only partially in fixed-order perturbative calculations), and become more and more important as the jets are observed at large rapidity separations.

Observe that calculations based on the unintegrated formalism will in general depend on two scales, μ and the rapidity, or angle, cut-off [27, 105, 117]. See e.g. the one-loop calculation [108] for an explicit example. It will be of interest to investigate the effect of Eq. (C.16) on the behavior in rapidity distributions [116].

Results for gluon-gluon channels are reported in Fig. C.6. Note the large effect of the purely gluonic component. The behavior versus k_T is qualitatively similar to that in Fig. C.4. Calculations in progress [116], including parton showering, indicate that quark and gluon channels give contributions of comparable size in the LHC forward kinematics. The inclusion of both is relevant for realistic studies of phenomenology [65, 94]. Since the forward kinematics selects asymmetric parton momentum fractions, effects due to the $x \rightarrow 1$ endpoint behavior [108, 118] at fixed transverse momentum may become phenomenologically significant as well.

We conclude this subsection by recalling that dynamical effects of high parton densities have been studied [95, 119] as potential contributions to forward jet events. We note that if such effects show up at the LHC, the unintegrated formulation discussed above would likely be the natural framework to implement this dynamics at parton-shower level.

C.5 Conclusions

Forward + central detectors at the LHC allow jet correlations to be measured across rapidity intervals of several units, $\Delta y \gtrsim 4 \div 6$. Such multi-jet states can be relevant to new particle discovery processes as well as new aspects of standard model physics.

Existing sets of forward-jet data in ep collisions, much more limited than the poten-

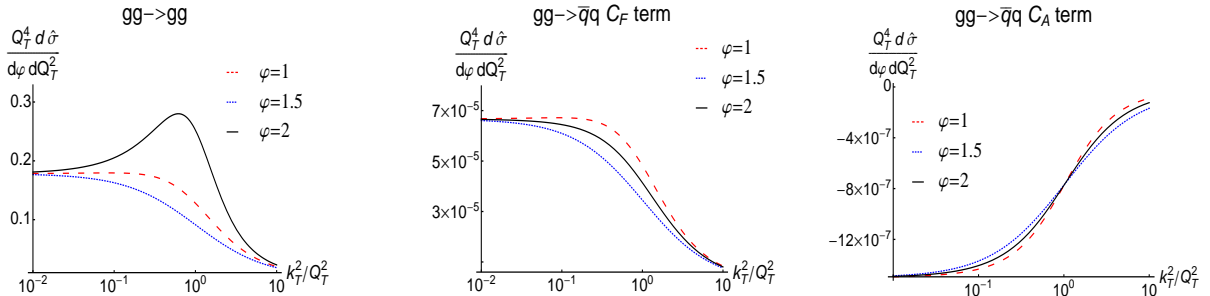


Figure C.6: The k_T/Q_T dependence of the factorizing gg matrix elements: (a) $gg \rightarrow gg$; (b) $gg \rightarrow q\bar{q}$ C_F term; (c) $gg \rightarrow q\bar{q}$ C_A term ($\xi_1\xi_2 S/Q_T^2 = 10^2$, $\alpha_s = 0.2$).

tial LHC yield, indicate that neither conventional parton-showering Monte Carlo generators nor next-to-leading-order QCD calculations are capable of describing forward jet phenomenology. These observations motivate studies of improved methods to compute QCD predictions in the multiple-scale kinematics implied by the forward region.

We have analyzed the high-energy factorization that serves to sum consistently to higher orders in α_s both the logarithmic corrections in the large rapidity interval and those in the hard jet transverse energy. We have determined the gauge-invariant (though not on shell) high-energy amplitudes, which are needed to evaluate the factorization formula for forward jet hadroproduction.

Our results can be used along with k_\perp -dependent kernels for parton branching. They can serve to construct predictions for exclusive observables associated to forward jets, including jet correlations, that take into account gluon coherence not only in the collinear emission region but also in the large-angle emission region.

Acknowledgments. One of us (F.H.) visited DESY at various stages while this work was being done and wishes to thank the DESY directorate for hospitality and support. Part of this work was carried out during the 2009 DESY Institute on Parton Showers and Resummations. We thank the organizers and participants in the workshop for the stimulating atmosphere. We gratefully acknowledge useful discussions with S. Baranov, J. Collins, A. Knutsson, A. Lipatov, Z. Nagy, T. Rogers and N. Zotov.

Bibliography

- [1] Particle Data Group Collaboration, C. Amsler *et al.*, Phys. Lett. **B667**, 1 (2008).
- [2] T. H1 and Z. Collaborations (2009). 0911.0884.
- [3] G. Dissertori *et al.*, JHEP **08**, 036 (2009). 0906.3436;
T. Gehrmann, G. Luisoni, and H. Stenzel, Phys. Lett. **B664**, 265 (2008). 0803.0695.
- [4] F. Halzen and A. D. Martin. New York, Usa: Wiley (1984) 396p.
- [5] J. C. Collins, D. E. Soper, and G. Sterman, Phys. Lett. **B134**, 263 (1984).
- [6] J. C. Collins and J.-W. Qui, Phys. Rev. **D75**, 114014 (2007). hep-ph/0705.2141v2.
- [7] V. N. Gribov and L. N. Lipatov, Sov. J. Nucl. Phys. **15**, 438 (1972);
L. N. Lipatov, Sov. J. Nucl. Phys. **20**, 94 (1975);
G. Altarelli and G. Parisi, Nucl. Phys. **B126**, 298 (1977).
- [8] T. Sjostrand, S. Mrenna, and P. Skands, JHEP **05**, 026 (2006). hep-ph/0603175.
- [9] M. Bahr *et al.*, Eur. Phys. J. **C58**, 639 (2008). 0803.0883.
- [10] T. Gleisberg *et al.*, JHEP **02**, 007 (2009). 0811.4622.
- [11] S. Jadach and M. Skrzypek, Acta Phys. Polon. **B40**, 2071 (2009). 0905.1399.
- [12] V. V. Sudakov, Sov. Phys. JETP **3**, 65 (1956).
- [13] M. Botje, Eur. Phys. J. **C14**, 285 (2000). hep-ph/9912439.
- [14] M. Gluck, E. Reya, and A. Vogt, Z. Phys. **C48**, 471 (1990).
- [15] T. Sjostrand, Phys. Lett. **B157**, 321 (1985).
- [16] G. Marchesini and B. R. Webber, Nucl. Phys. **B310**, 461 (1988).
- [17] V. S. Fadin, E. A. Kuraev, and L. N. Lipatov, Phys. Lett. **B60**, 50 (1975);
E. A. Kuraev, L. N. Lipatov, and V. S. Fadin, Sov. Phys. JETP **44**, 443 (1976);
E. A. Kuraev, L. N. Lipatov, and V. S. Fadin, Sov. Phys. JETP **45**, 199 (1977);
I. I. Balitsky and L. N. Lipatov, Sov. J. Nucl. Phys. **28**, 822 (1978).

-
- [18] C. R. Schmidt (2001). [hep-ph/0106181](#).
- [19] J. R. Forshaw and D. A. Ross, Cambridge Lect. Notes Phys. **9**, 1 (1997).
- [20] V. Barone and E. Predazzi, Springer Verlag **1**, 1 (2002).
- [21] J. Kwiecinski, J. Phys. **G22**, 685 (1996). [hep-ph/9602286](#).
- [22] L. H. Orr and W. J. Stirling, Phys. Lett. **B436**, 372 (1998). [hep-ph/9806371](#);
L. H. Orr and W. J. Stirling, Phys. Rev. **D56**, 5875 (1997). [hep-ph/9706529](#).
- [23] C. R. Schmidt, Phys. Rev. Lett. **78**, 4531 (1997). [hep-ph/9612454](#).
- [24] J. Bartels, A. Sabio Vera, and F. Schwennsen, JHEP **0611**, 051 (2006).
[hep-ph/0608154](#).
- [25] M. Ciafaloni, Nucl. Phys. **B296**, 49 (1988);
S. Catani, F. Fiorani, and G. Marchesini, Phys. Lett. **B234**, 339 (1990);
S. Catani, F. Fiorani, and G. Marchesini, Nucl. Phys. **B336**, 18 (1990);
G. Marchesini, Nucl. Phys. **B445**, 49 (1995).
- [26] H. Jung, Comput. Phys. Commun. **143**, 100 (2002). [hep-ph/0109102](#);
H. Jung and G. P. Salam, Eur. Phys. J. **C19**, 351 (2001). [hep-ph/0012143](#).
- [27] Small x Collaboration, J. R. Andersen *et al.*, Eur. Phys. J. **C48**, 53 (2006).
[hep-ph/0604189](#).
- [28] Small x Collaboration, J. R. Andersen *et al.*, Eur. Phys. J. **C35**, 67 (2004).
[hep-ph/0312333](#).
- [29] Small x Collaboration, B. Andersson *et al.*, Eur. Phys. J. **C25**, 77 (2002).
[hep-ph/0204115](#).
- [30] A. Knutsson, A. Bacchetta, H. Jung, and K. Kutak (2008). 0808.0847;
Y. L. Dokshitzer, Sov. Phys. JETP **46**, 641 (1977).
- [31] B. Andersson, G. Gustafson, G. Ingelman, and T. Sjostrand, Phys. Rept. **97**, 31 (1983).
- [32] CDF Collaboration, R. D. Field (2002). [hep-ph/0201192](#);
CDF Collaboration, R. Field and R. C. Group (2005). [hep-ph/0510198](#).
- [33] T. Sjostrand and M. van Zijl, Phys. Rev. **D36**, 2019 (1987).
- [34] T. Sjostrand and P. Z. Skands, JHEP **03**, 053 (2004). [hep-ph/0402078](#);
T. Sjostrand and P. Z. Skands, Eur. Phys. J. **C39**, 129 (2005). [hep-ph/0408302](#).
- [35] M. Bahr, S. Gieseke, and M. H. Seymour, JHEP **07**, 076 (2008). 0803.3633.

- [36] Y. L. Dokshitzer, D. Diakonov, and S. I. Troian, Phys. Rept. **58**, 269 (1980);
Y. L. Dokshitzer, D. Diakonov, and S. I. Troian, Phys. Lett. **B79**, 269 (1978).
- [37] J. C. Collins, D. E. Soper, and G. Sterman, Nucl. Phys. **B250**, 199 (1985).
- [38] R. K. Ellis, D. A. Ross, and S. Veseli, Nucl. Phys. **B503**, 309 (1997).
hep-ph/9704239;
R. K. Ellis and S. Veseli, Nucl. Phys. **B511**, 649 (1998). hep-ph/9706526.
- [39] A. Kulesza and W. J. Stirling, Nucl. Phys. **B555**, 279 (1999). hep-ph/9902234.
- [40] S. Berge, P. M. Nadolsky, F. Olness, and C. P. Yuan (2004). hep-ph/0401128;
S. Berge, P. M. Nadolsky, F. Olness, and C. P. Yuan, Phys. Rev. **D72**, 033015 (2005).
hep-ph/0410375.
- [41] J. Kwiecinski and A. Szczurek, Nucl. Phys. **B680**, 164 (2004). hep-ph/0311290.
- [42] A. Gawron, J. Kwiecinski, and W. Broniowski, Phys. Rev. **D68**, 054001 (2003).
hep-ph/0305219.
- [43] E. Levin and J. Miller (2008). 0801.3593.
- [44] A. Gawron and J. Kwiecinski, Acta Phys. Polon. **B34**, 133 (2003). hep-ph/0207299.
- [45] S. P. Baranov, A. V. Lipatov, and N. P. Zotov, Phys. Rev. **D77**, 074024 (2008).
0708.3560;
S. P. Baranov, A. V. Lipatov, and N. P. Zotov, Phys. Rev. **D78**, 014025 (2008).
0805.4821.
- [46] M. A. Kimber, A. D. Martin, and M. G. Ryskin, Phys. Rev. **D63**, 114027 (2001).
hep-ph/0101348;
G. Watt, A. D. Martin, and M. G. Ryskin, Eur. Phys. J. **C31**, 73 (2003).
hep-ph/0306169.
- [47] S. P. Baranov, A. V. Lipatov, and N. P. Zotov (2008). 0811.2575.
- [48] M. Deak and F. Schwennsen, JHEP **09**, 035 (2008). 0805.3763.
- [49] S. P. Martin (1997). hep-ph/9709356.
- [50] B. A. Kniehl, A. V. Shipilova, and V. A. Saleev, Phys. Rev. **D79**, 034007 (2009).
0812.3376.
- [51] M. Buza, Y. Matiounine, J. Smith, and W. L. van Neerven, Phys. Lett.
B411, 211 (1997). hep-ph/9707263;
A. D. Martin, R. G. Roberts, M. G. Ryskin, and W. J. Stirling, Eur. Phys. J.
C2, 287 (1998). hep-ph/9612449.

- [52] R. S. Thorne, Nucl. Phys. Proc. Suppl. **191**, 54 (2009);
R. S. Thorne, J. Phys. **G25**, 1307 (1999). [hep-ph/9902299](#).
- [53] Y. L. Dokshitzer, V. A. Khoze, and S. I. Troian, J. Phys. **G17**, 1602 (1991).
- [54] J. Campbell and K. Ellis. <http://mcfm.fnal.gov/>.
- [55] M. Deak, F. Hautmann, H. Jung, and K. Kutak, JHEP **09**, 121 (2009). [0908.0538](#).
- [56] H1 Collaboration, A. Aktas *et al.*, Eur. Phys. J. **C46**, 27 (2006). [hep-ex/0508055](#);
ZEUS Collaboration, S. Chekanov *et al.*, Phys. Lett. **B632**, 13 (2006).
[hep-ex/0502029](#).
- [57] D0 Collaboration, C. Royon. Prepared for 8th International Workshop on Deep Inelastic Scattering and QCD (DIS 2000), Liverpool, England, 25-30 Apr 2000;
CDF Collaboration, L. R. Babukhadia (1999). [hep-ex/0001062](#).
- [58] A. Sabio Vera and F. Schwennsen, Phys. Rev. **D77**, 014001 (2008). [0708.0549](#).
- [59] M. Klein (2009). [0908.2877](#).
- [60] O. Kepka, C. Royon, C. Marquet, and R. B. Peschanski, Phys. Lett. **B655**, 236 (2007). [hep-ph/0609299](#);
O. Kepka, C. Royon, C. Marquet, and R. B. Peschanski, Eur. Phys. J. **C55**, 259 (2008). [hep-ph/0612261](#).
- [61] CMS Coll., CERN-LHCC-2006-001 (2006); CMS PAS FWD-08-001 (2008).
- [62] ATLAS Coll., CERN-LHCC-2008-004 (2008); CERN-LHCC-2007-001 (2007).
- [63] CMS Coll., TOTEM Coll., CERN-LHCC-2006-039/G -124 (2006).
- [64] X. Aslanoglou *et al.*, Eur. Phys. J. **C52**, 495 (2007). [0706.2641](#).
- [65] A. Sabio Vera and F. Schwennsen, Nucl. Phys. **B776**, 170 (2007). [hep-ph/0702158](#);
C. Marquet and C. Royon, Phys. Rev. **D79**, 034028 (2009). [0704.3409](#);
P. Aurenche, R. Basu, and M. Fontannaz, Eur. Phys. J. **C57**, 681 (2008). [0807.2133](#);
J. Kwiecinski, A. D. Martin, L. Motyka, and J. Outhwaite, Phys. Lett. **B514**, 355 (2001). [hep-ph/0105039](#).
- [66] A. Sabio Vera, Nucl. Phys. **B746**, 1 (2006). [hep-ph/0602250](#).
- [67] A. H. Mueller and H. Navelet, Nucl. Phys. **B282**, 727 (1987).
- [68] V. Del Duca, M. E. Peskin, and W.-K. Tang, Phys. Lett. **B306**, 151 (1993).
[hep-ph/9303237](#).
- [69] W. J. Stirling, Nucl. Phys. **B423**, 56 (1994). [hep-ph/9401266](#).

- [70] S. P. Baranov and V. L. Slad, *Phys.Atom.Nucl.* **67**, 808 (2004). [hep-ph/0603090](#).
- [71] L. Agostino, L. Malgeri, G. Daskalakis, P. Govoni, and M. Paganoni, *J. Phys.* **G33**, N67 (2007);
J. D'Hondt, S. Lowette, J. Heyninck, and S. Kasselmann, *CMS NOTE* **025** (2006).
- [72] M. Dittmar, F. Pauss, and D. Zurcher, *Phys. Rev.* **D56**, 7284 (1997). [hep-ex/9705004](#).
- [73] S. Catani, M. Ciafaloni, and F. Hautmann, *Nucl. Phys.* **B366**, 135 (1991).
- [74] J. C. Collins and R. K. Ellis, *Nucl. Phys.* **B360**, 3 (1991).
- [75] L. V. Gribov, E. M. Levin, and M. G. Ryskin, *Phys. Rept.* **100**, 1 (1983);
E. M. Levin, M. G. Ryskin, Y. M. Shabelski, and A. G. Shuvaev, *Sov. J. Nucl. Phys.* **53**, 657 (1991).
- [76] J. C. Collins and D. E. Soper, *Nucl. Phys.* **B193**, 381 (1981);
X. Ji, J.-p. Ma, and F. Yuan, *Phys. Rev.* **D71**, 034005 (2005). [hep-ph/0404183](#);
X. Ji, J.-P. Ma, and F. Yuan, *Phys. Lett.* **B597**, 299 (2004). [hep-ph/0405085](#);
J. C. Collins and A. Metz, *Phys. Rev. Lett.* **93**, 252001 (2004). [hep-ph/0408249](#);
A. Bacchetta, C. Bomhof, P. Mulders, and F. Pijlman, *Phys.Rev.* **D72**, 034030 (2005). [hep-ph/0505268](#).
- [77] S. P. Baranov, A. V. Lipatov, and N. P. Zotov (2007). [arXiv:0708.3560 \[hep-ph\]](#).
- [78] D. Binosi and L. Theussl, *Comput. Phys. Commun.* **161**, 76 (2004). [hep-ph/0309015](#).
- [79] L. N. Lipatov, *Sov. J. Nucl. Phys.* **23**, 338 (1976).
- [80] J. A. M. Vermaseren (2000). [math-ph/0010025](#).
- [81] J. A. M. Vermaseren, *Nucl. Phys. Proc. Suppl.* **116**, 343 (2003). [hep-ph/0211297](#).
- [82] J. R. Forshaw and A. Sabio Vera, *Phys. Lett.* **B440**, 141 (1998). [hep-ph/9806394](#);
B. R. Webber, *Phys. Lett.* **B444**, 81 (1998). [hep-ph/9810286](#);
G. P. Salam, *JHEP* **03**, 009 (1999). [hep-ph/9902324](#);
J. Campbell and K. Ellis, *Phys. Rev. D* **65**, 113007 (2002). [hep-ph/0202176](#);
J. Campbell, K. Ellis, and D. Rainwatter, *Phys. Rev. D* **68**, 094021 (2003). [hep-ph/0308195](#).
- [83] J. Pumplin, D. Stump, J. Huston, H. Lai, P. Nadolsky, and W. Tung, *JHEP* **0207**, 012 (2002).
- [84] V. S. Fadin and L. N. Lipatov, *Phys. Lett.* **B429**, 127 (1998). [hep-ph/9802290](#);
M. Ciafaloni and G. Camici, *Phys. Lett.* **B430**, 349 (1998). [hep-ph/9803389](#).
- [85] C. Balazs and C. P. Yuan, *Phys. Rev.* **D56**, 5558 (1997). [hep-ph/9704258](#).

- [86] M. Hansson and H. Jung (2003). [hep-ph/0309009](#).
- [87] H. Jung (2004). [hep-ph/0411287](#).
- [88] H1 Collaboration, S. Aid *et al.*, Nucl. Phys. **B470**, 3 (1996). [hep-ex/9603004](#);
H1 Collaboration, C. Adloff *et al.*, Eur. Phys. J. **C21**, 33 (2001). [hep-ex/0012053](#);
ZEUS Collaboration, M. Derrick *et al.*, Z. Phys. **C72**, 399 (1996). [hep-ex/9607002](#);
ZEUS Collaboration, S. Chekanov *et al.*, Eur. Phys. J. **C21**, 443 (2001).
[hep-ex/0105090](#).
- [89] FP420 R and D Collaboration, M. G. Albrow *et al.* (2008). [0806.0302](#).
- [90] M. Grothe (2009). [0901.0998](#).
- [91] L. Adamczyk *et al.* (2009). [0903.3861](#).
- [92] A. De Roeck, V. A. Khoze, A. D. Martin, R. Orava, and M. G. Ryskin, Eur. Phys. J. **C25**, 391 (2002). [hep-ph/0207042](#).
- [93] S. Heinemeyer *et al.*, Eur. Phys. J. **C53**, 231 (2008). [0708.3052](#).
- [94] CMS Collaboration, S. Cerci and D. d’Enterria, AIP Conf. Proc. **1105**, 28 (2009).
[0812.2665](#).
- [95] D. d’Enterria, AIP Conf. Proc. **1038**, 95 (2008). [0806.0883](#);
D. G. d’Enterria, Eur. Phys. J. **A31**, 816 (2007). [hep-ex/0610061](#).
- [96] A. Accardi *et al.* (2004). [hep-ph/0308248](#).
- [97] CMS Coll., CERN-LHCC-2007-009 (2007).
- [98] C. Ewerz, L. H. Orr, W. J. Stirling, and B. R. Webber, J. Phys. **G26**, 696 (2000).
[hep-ph/9912469](#);
J. R. Forshaw, A. Sabio Vera, and B. R. Webber, J. Phys. **G25**, 1511 (1999).
[hep-ph/9812318](#).
- [99] J. R. Andersen *et al.* (2001). [hep-ph/0109019](#);
J. R. Andersen, V. Del Duca, S. Frixione, C. R. Schmidt, and W. J. Stirling, JHEP
02, 007 (2001). [hep-ph/0101180](#).
- [100] J. R. Andersen and A. Sabio Vera, Phys. Lett. **B567**, 116 (2003). [hep-ph/0305236](#);
J. R. Andersen (2009). [0906.1965](#);
J. R. Andersen and C. D. White, Phys. Rev. **D78**, 051501 (2008). [0802.2858](#).
- [101] A. H. Mueller, Nucl. Phys. Proc. Suppl. **18C**, 125 (1991).

- [102] W.-K. Tang, Phys. Lett. **B278**, 363 (1992);
J. Bartels, A. de Roeck, and M. Loewe, Z. Phys. **C54**, 635 (1992);
J. Kwiecinski, A. D. Martin, and P. J. Sutton, Phys. Rev. **D46**, 921 (1992);
S. Catani, M. Ciafaloni, and F. Hautmann, Nucl. Phys. Proc. Suppl. **29A**, 182 (1992).
- [103] B. R. Webber (1995). [hep-ph/9510283](#).
- [104] S. Catani, M. Ciafaloni, and F. Hautmann, Phys. Lett. **B307**, 147 (1993);
S. Catani, M. Ciafaloni, and F. Hautmann, Nucl. Phys. **B366**, 135 (1991);
S. Catani, M. Ciafaloni, and F. Hautmann, Phys. Lett. **B242**, 97 (1990).
- [105] J. Collins, PoS **LC2008**, 028 (2008). [0808.2665](#).
- [106] F. Hautmann, Acta Phys. Polon. **B40**, 2139 (2009).
- [107] T. C. Rogers, Phys. Rev. **D78**, 074018 (2008). [0807.2430](#).
- [108] F. Hautmann, Phys. Lett. **B655**, 26 (2007). [hep-ph/0702196](#).
- [109] S. Catani and F. Hautmann, Nucl. Phys. **B427**, 475 (1994). [hep-ph/9405388](#);
S. Catani and F. Hautmann, Phys. Lett. **B315**, 157 (1993).
- [110] M. Ciafaloni, Phys. Lett. **B429**, 363 (1998). [hep-ph/9801322](#).
- [111] F. Schwennsen (2007). [hep-ph/0703198](#);
J. Bartels, A. Sabio Vera, and F. Schwennsen (2007). [0709.3249](#);
J. Bartels, D. Colferai, and G. P. Vacca, Eur. Phys. J. **C29**, 235 (2003).
[hep-ph/0206290](#);
J. Bartels, D. Colferai, and G. P. Vacca, Eur. Phys. J. **C24**, 83 (2002).
[hep-ph/0112283](#).
- [112] F. Hautmann and H. Jung, JHEP **10**, 113 (2008). [0805.1049](#);
F. Hautmann and H. Jung (2008). [0804.1746](#).
- [113] I. Balitsky, Phys. Rev. **D72**, 074027 (2005). [hep-ph/0507237](#).
- [114] Y. L. Dokshitzer and G. Marchesini, JHEP **01**, 007 (2006). [hep-ph/0509078](#).
- [115] Y. L. Dokshitzer, V. A. Khoze, S. I. Troian, and A. H. Mueller, Rev. Mod. Phys. **60**, 373 (1988).
- [116] M. Deák, F. Hautmann, H. Jung, and K. Kutak, in preparation.
- [117] J. C. Collins (2001). [hep-ph/0106126](#).
- [118] J. C. Collins and F. Hautmann, JHEP **03**, 016 (2001). [hep-ph/0009286](#);
J. C. Collins and F. Hautmann, Phys. Lett. **B472**, 129 (2000). [hep-ph/9908467](#).

- [119] E. Iancu, M. S. Kugeratski, and D. N. Triantafyllopoulos, Nucl. Phys. **A808**, 95 (2008). 0802.0343;
E. Iancu, C. Marquet, and G. Soyez, Nucl. Phys. **A780**, 52 (2006). hep-ph/0605174;
C. Marquet and R. B. Peschanski, Phys. Lett. **B587**, 201 (2004). hep-ph/0312261;
Y. Hatta, E. Iancu, and A. H. Mueller, JHEP **01**, 026 (2008). 0710.2148.

Acknowledgements

First of all I would like to thank my supervisor Dr. Hannes Jung for many interesting discussions, supervising me during my PhD studies, giving me the opportunity to discuss with other physicists by organising interesting meetings and reading the manuscript several times and giving useful comments and corrections.

I would like to thank Dr. Carsten Niebuhr for letting me be a part of H1 collaboration which was financing me during my studies and gave me opportunity to learn a lot about experimental physics.

For financing my 4-months long stay at CERN I am thankful to MCNet.

I am very thankful to Jochen Bartels, Francesco Hautmann, Hannes Jung, Krzysztof Kutak and Florian Schwennsen for fruitful collaboration. I want to acknowledge stimulating and interesting discussions with Alessandro Bacchetta, Sergey Baranov, Jochen Bartels, Gosta Gustafsson, Francesco Hautmann, Krzysztof Kutak, Artem Lipatov, Simone Marzani, Leszek Motyka, Florian Schwennsen, Mike Seymour, Tobias Toll and Nikolaj Zotov.

For reading a part of the manuscript and giving useful comments I would like to thank also Voica Radescu.

I have to thank my family for supporting me and leading me to science since my childhood.

I am very pleased that people who were surrounding me during my PhD. studies created a very friendly atmosphere not only at the working place, but also in my spare time. For this I am thankful to Sebastian Aderhold, Alessandro Bacchetta, Axel Cholewa, Matt Forest, Anastasia Grebenyuk, Julia Grebenyuk, Hannes Jung, Albert Knutsson, Krzysztof Kutak, Angela Lucaci-Timoce, Lluís Martí, Tim Namsoo, Voica Radescu, Julia Ruiz Tabasco, Carlos Sandoval, Niladri Sen, Felix Schlander, Zlatka Staykova, Tobias Toll, Martin von den Driesch and Eberhard Wuensch.

